

Compton Scattering Polarimetry for the Determination of the Proton's Weak
Charge Through Measurements of the Parity-Violating Asymmetry of $^1\text{H}(\text{e},\text{e}')\text{p}$

Juan Carlos Cornejo
Bell, California

Masters of Science, College of William & Mary, 2010
Bachelors of Science, California State University, Los Angeles, 2005

A Dissertation presented to the Graduate Faculty
of the College of William and Mary in Candidacy for the Degree of
Doctor of Philosophy


Department of Physics

The College of William and Mary
August 2016

© 2016
Juan Carlos Cornejo
All Rights Reserved

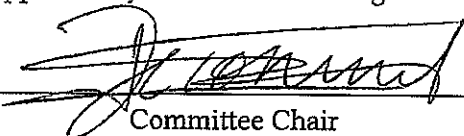
APPROVAL PAGE

This Dissertation is submitted in partial fulfillment of
the requirements for the degree of
Doctor of Philosophy



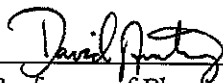
Juan Carlos Cornejo

Approved by the Committee August 2015

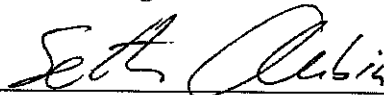


Committee Chair

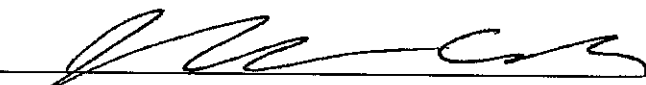
Assistant Professor Wouter Deconinck, Physics
The College of William & Mary



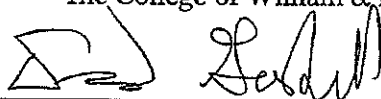
Chancellor Professor of Physics David Armstrong, Physics
The College of William & Mary



Associate Professor Seth Aubin, Physics
The College of William & Mary



Class of 2017 Associate Professor of Physics Joshua Erlich, Physics
The College of William & Mary



Dr. David Gaskell,
Jefferson Lab

ABSTRACT

The Standard Model has been a theory with the greatest success in describing the fundamental interactions of particles. As of the writing of this dissertation, the Standard Model has not been shown to make a false prediction. However, the limitations of the Standard Model have long been suspected by its lack of a description of gravity, nor dark matter. Its largest challenge to date, has been the observation of neutrino oscillations, and the implication that they may not be massless, as required by the Standard Model. The growing consensus is that the Standard Model is simply a lower energy effective field theory, and that new physics lies at much higher energies.

The Q_{weak} Experiment is testing the Electroweak theory of the Standard Model by making a precise determination of the weak charge of the proton (Q_W^p). Any signs of “new physics” will appear as a deviation to the Standard Model prediction. The weak charge is determined via a precise measurement of the parity-violating asymmetry of the electron-proton interaction via elastic scattering of a longitudinally polarized electron beam of an un-polarized proton target.

The experiment required that the electron beam polarization be measured to an absolute uncertainty of 1 %. At this level the electron beam polarization was projected to contribute the single largest experimental uncertainty to the parity-violating asymmetry measurement.

This dissertation will detail the use of Compton scattering to determine the electron beam polarization via the detection of the scattered photon. I will conclude the remainder of the dissertation with an independent analysis of the blinded Q_{weak} .

TABLE OF CONTENTS

Acknowledgements.....	iv
Dedication.....	vi
List of Tables.....	vii
List of Figures.....	ix
1 Introduction.....	1
2 Basic Standard Model Theory.....	3
2.1 Standard Model Mathematical Formulation.....	4
2.2 Unification of Electromagnetic and Weak Interactions.....	7
2.3 Parity and Left-Handed Fermions.....	10
2.4 Tests and Limits of the Standard Model.....	12
2.4.1 Weak Charges.....	15
3 The Q_{weak} Experiment.....	20
3.1 Elastic Electron Scattering.....	21
3.2 Electron-Proton Scattering Form Factors.....	26
3.3 Parity Violating Electron Scattering.....	30
3.4 The Weak Charge of the Proton.....	32
3.4.1 Extracting Q_w^p Through the Parity-Violating Asymmetry.....	34
3.5 Polarization Effects on the Asymmetry.....	35
3.5.1 Transverse Asymmetries.....	36
4 The Q_{weak} Experimental Apparatus.....	38
4.1 Polarized Beam Source and High Luminosity.....	41
4.1.1 Producing Polarized Electrons.....	41
4.1.2 Helicity Control and Reversal.....	43
4.1.3 Primary Target.....	44
4.2 Main Detectors.....	45
4.3 Spectrometer Magnet.....	46
4.4 Collimation and Shielding System.....	47
4.5 Tracking Detectors.....	50
4.5.1 Horizontal Drift Chambers.....	51
4.5.2 Vertical Drift Chambers.....	53
4.5.3 Triggering Scintillator.....	54
4.5.4 Focal Plane Scanner.....	55
4.6 Background Detectors.....	55
4.7 Beam Monitors.....	57
4.7.1 Polarimeters.....	57
4.7.2 Current Monitors.....	60
4.7.3 Position Monitors.....	61
4.7.4 Luminosity Monitors.....	63

4.7.5	Beam Modulation System	64
4.8	Auxiliary Targets.....	65
5	Compton Scattering and Polarimetry	67
5.1	Polarimetry Through Compton Scattering	67
5.1.1	Kinematics of Compton Scattering.....	68
5.1.2	Compton Cross Section	71
5.2	The Hall C Compton Polarimeter	75
5.2.1	Laser System	77
5.2.2	Electron Detector	82
5.2.3	Photon Detector	84
5.3	Compton Data Acquisition	88
5.3.1	Timing and Helicity Trigger	89
5.3.2	Scalers	91
5.3.3	Photon Detector Signal	93
5.3.4	Linearity Electronics.....	98
5.3.5	Slow Data (EPICS).....	98
5.3.6	Data Processing.....	99
6	Photon Detector Analysis	104
6.1	Measuring the Experimental Asymmetry	105
6.1.1	Calibrating the Charge Monitors	106
6.1.2	Calibrating the Position Monitors	109
6.1.3	Background Sources and Corrections.....	112
6.1.4	Determining and Correcting for Pedestal	123
6.1.5	Measured Asymmetries.....	127
6.1.6	Corrections to the Asymmetry and Errors	130
6.1.7	Sensitivity to Beam Properties	131
6.2	Determining the Analyzing Power	133
6.2.1	Monte Carlo Simulation	134
6.2.2	Determined Analyzing Powers.....	144
6.3	Beam Polarizations from the Photon Detector.....	146
6.4	Additional Corrections and Errors	146
6.4.1	Spin Precession and Depolarization Effects	147
6.4.2	Building the Table of Errors	150
7	A Blinded Q_{weak} Asymmetry	151
7.1	Determining the Measured Asymmetry.....	152
7.1.1	Blinding the Asymmetry	153
7.1.2	Blinded Detector Asymmetries	155
7.1.3	Corrections Due to Beam Properties	157
7.1.4	Transverse Polarization and Signal Non-Linearity.....	162

7.2	Determining the PVES Asymmetry	163
7.2.1	Background Corrections	165
7.2.2	Experimental Bias Corrections	175
7.2.3	The Blinded Run II Parity-Violating Asymmetry	177
8	Results and Discussions	180
8.1	The World PVES Data	180
8.2	Determination of the Blinded Q_w^p	181
8.3	Extracting the Weak Coupling Constants	182
8.4	Closing Remarks	183
A	Appendix Compton Tables	186
B	Appendix Compton Analysis Figures	192
C	Appendix appendix]sec:QweakTablesQweak Tables	197
D	Appendix Miscellaneous Figures for Q_{weak}	200
E	Appendix Derivation of Background Corrected A_{ep}^{PV}	202

ACKNOWLEDGEMENTS

As I write these last few lines of my dissertation, I am reminded of all the people in my life whom have made this possible. This dissertation is the culmination of support from many people helping and supporting me both directly as well as behind the scenes. I would like to share my appreciation for all of their hard work:

First, I would like to thank my advisor, Wouter Deconinck, for all his advice, help, and patience throughout my years as his student. I am grateful for him always being available to answer questions, even, to my surprise, at odd hours of the night. Thank you also Dave Gaskell and David Armstrong for your support and helpful advise. Thanks to the other two members of my dissertation committee, Joshua Erlich and Seth Aubin for your comments and suggestions in the weeks leading to the defense.

Next, I would like to thank my family and friends whom offered support and encouragement throughout this entire journey. Thanks to my parents María Dolores Cornejo and Francisco Javier Cornejo for dedicating your lives to ensure your children reached whatever goals they wanted. Thanks to my older brother Francisco Javier Cornejo for being the whole reason I decided to pursue science. Thanks to my brother José Oswaldo Cornejo, and my two sisters Marisol Cornejo and Azucena Cornejo for their attention and patience while I rambled on about science, even if they were too young to understand much at the time. Thanks to my closest friend Samn Dammet for the many years of friendship, and for being there to support me even though I am on the other side of the country. And thanks to a recent friend Eunice Mercado Lara, whose visit during the last few months of my degree ensured that I would eventually reach the goal line. I would like to extend my gratitude to the Hall C Compton Polarimeter group for all of their support and hard work. Special thanks to Amrendra Narayan, Donald Jones, Mark Dalton, Kent Paschke, Vladas Tvaskis, and Jeffrey Martin. Thanks also to the many collaborators who worked hard and long hours to ensure the success of the Q_{weak} experiment.

Writing and finishing a dissertation is both difficult and stressful, but it was made less stressful with the help Melissa Cummings and Leonidas Aliaga Soplín whom together we sat long hours on Sundays to ensure we each stayed focused. I would also like to thank my undergraduate professors, Konrad Aniol, Marty Epstein, and Dimitry Margaziotis, whom encouraged me to pursue a graduate degree in the field of Experimental Nuclear Physics.

I also want to acknowledge and share my gratitude to the many friends I made at William & Mary whose friendship gave me the strength to finish. These are, without order, Martín Rodríguez-Vega, Valerie Gray, Ellie Radue, Raymundo

Ramos, and Kurtis Bartlett and Gleb Romanov.

Lastly, I would like to thank all the small creatures which have been with me throughout my life. They may be small and incapable of speaking our language, but they have provided often needed company and love, despite their short lifespans. Thank you Templeton, Juno, Nicholay, Sephi, Ra, Tito, and the smallest of them all, Latte, Mocha and Tiny.

This dissertation is dedicated to my family.

LIST OF TABLES

2.1	A table listing the electromagnetic charge Q , the third component of the $SU_c(3)$ isospin T_3 and the weak vector and axial-vector “charges.”	18
3.1	The net weak charges of the quarks, neutron, and proton, respectively. Calculated in terms of the C_{1u} and C_{1d} coupling constants.	34
6.1	Analyzing powers determined from Monte Carlo for the three shielding configurations. Statistical errors only. Not corrected for detector non-linearity.	145
6.2	Error contributions on the determination of the electron beam polarization using the photon detector. The notation ($\ll 1\%$) means the error is significantly small, and essentially zero. H-C stands for Helicity Correlated.	150
A.1	Table map of the scaler channels located on ROC 31, Bank 0x1f02.	187
A.2	Tables of the calibration factors and pedestals for the Unser and BCMs 1, 2 and 6 for runs taken from December 2011 to May 2012.	188
A.3	Listing of each respective pedestal on each antenna. The global calibration is set to 1 and instead relies on the relative gain α between the two antennas. The angle corresponds to the rotation around the beamline. Lastly, the absolute distance from the start of the Hall C beamline is listed.	189
A.4	Table of photon detector compared to electron detector for the 1 thin lead and no thin lead configuration. Only includes the statistical errors, where the photon detector includes the statistical error of the analyzing power.	190
A.5	Table of photon detector compared to electron detector for 2 thin lead configuration at the nominal beam energy (top) of 1160 MeV and the special 879 MeV running period. Only includes the statistical errors, where the photon detector includes the statistical error of the analyzing power.	191
C.1	The results of the raw blinded asymmetry due to various regression schemes. The schemes are defined in [89]. Sets 5, 6 and 13 were excluded due to incomplete coverage of the entire asymmetry data set. Set 9 is an outlier due to the inclusion of a luminosity monitor which is highly sensitive to other background processes. The remaining schemes were all fairly consistent. “DoF” stands for Degrees of Freedom.	198

C.2	Table of Wien periods and the Q_{weak} runs. The approximate Compton polarimeter runs are also shown.	199
-----	---	-----

LIST OF FIGURES

2.1	An illustration of the particles included in the Standard Model. It shows the three main groups: leptons, quarks and Gauge bosons, the first two of which have three generations. The top right particle is the Higgs boson. Reproduced from Wikipedia[1].	4
2.2	An example illustration showing the effects on a key-hole (left) if the parity operator \mathcal{P} where to mirror they key-hole (right). In this case, the key for the hole on the left would not fit the key on the hole on the right, despite their similarities.	11
2.3	The two neutral current exchange vertexes where either a virtual photon (left) or a weak neutral boson (right) is exchanged, but leaves the two fermions the same.	15
3.1	The two ElectroWeak Neutral Current interactions at tree level are due to the exchange of a photon (left) and a massive Z_0 boson (right). In elastic scattering we require that all states, intial, final and any intermediate, be the same.	21
3.2	The kinematics of a two-body interaction can be simplified into a 2D plane, as shown here in the laboratory coordinate system. This interaction is fully symmetric around the out of plane angle $\phi \in [0, 2\pi]$ defined by rotations around the $+z$ axis.	22
4.1	A cartoon overview describing the functionality of CEBAF. Graciously provided by JLab's Public Affairs office.	39
4.2	An illustration of the main components of the detector[26].	40
4.3	Left: A drawing of the electron bands of the GaAs crystal. The highest band is the conduction band and just below is the 1.52 eV band gap. Right: An illustration of possible and relative rates of excitations from the lower non-conducting bands due to an excitation of a circularly polarized photon. The solid lines represent circularly right (σ^+) and the dashed lines circularly left (σ^-) photons. The circles represent the relative rates of excitation with respect to each other. Image taken from [28].	42
4.4	Noise on the Main Detectors due to rapid density fluctuations in the LH_2 target[34].	45
4.5	Figures showing the relative rates around the Main Detectors (left) and the relative positions of the various detectors (right).	47
4.6	Figure showing the lead lintels installed within the coils of the Q_{weak} Toroidal Magnet. CAD drawing provided by the JLab Engineering group.	49

4.7	A profile of tracks projected back to the defining collimator near the HDCs. The few projections seen outside of the enclosed region are likely improperly reconstructed tracks due to multiple scattering of the particles before detection. Image provided by David Armstrong.....	52
4.8	A drawing of the Q_{weak} Vertical Drift Chambers as seen from Octant 3. The particle's nominal trajectory intersects the VDCs at a 45° angle with respect to the VDCs plane. The sense wires are strung perpendicular to each other and 26.5° with respect to the edge of the frame.....	54
4.9	Relative rate map of the flux over the MD bar as seen by the focal plane scanner in octant 7 (see fig. 4.5b) [32]. The vertical y-axis is in the radial direction and the x-axis is tangent to the radial direction and perpendicular to the beam direction. The characteristic "mustache" shape seen in the rates on the MD bar in octant 7 as mapped out by the scanner apparatus.....	56
4.10	Drawing of the Møller Polarimeter layout showing the main components of the polarimeter. Møller scattered electrons from the target would be selected by a quadrupole-collimator-quadrupole configuration. The resulting Møller scattered electron pairs were detected in coincidence by the detectors on either side of the beamline. Figure courtesy of Howard Fenker.....	59
4.11	A schematic of the SEE BPM system employed at CEBAF showing the relative position of the four-wire stripline antenna. The antenna's are isolated by a SEE setup and 1497 MHz signal is down converted to 45 MHz to be read out by commercial data acquisition systems. Taken from [45]	62
4.12	An illustration showing the relative positions of the solid auxiliary targets. In the real setup not all available positions were used, particularly in the case when they would overlap one of the targets downstream.	65
5.1	Compton scattering on the x - z plane as show in the lab frame and the electron rest frame. The electron rest frame is the conventional Compton scattering frame, which we then boost into the laboratory frame at the end.	68
5.2	The main contributing processes of Compton scattering expressed via Mandelstam variable channels s and u respectively.	71
5.3	Graphs showing the properties of the photon scattered energies and cross sections under the Q_{weak} kinematics and a special running period during the Q_{weak} running. The two energies correspond to the nominal Q_{weak} energy of 1160 MeV and the special running period at 879 MeV. ...	72

5.4	Plots of both the longitudinally polarized component of the Compton scattering cross section and the respective asymmetry. Note that the sign of the asymmetry is dependent on the definition of the handedness of the electron and the polarization direction of the photon. The transverse component has been excluded as it goes to zero under an integral over the azimuthal angle ϕ	74
5.5	Drawing of the Compton Polarimeter. We see the four dipole chicane diverting the beam towards the laser table. The third dipole selects the Compton scattered electrons and allows the photons to pass through to the photon detector. The fourth dipole then diverts the remainder of the beam towards the LH ₂ target. Thanks to Donal Jones for providing this picture.	76
5.6	A map of the magnetic field normalized to the supplied current and plotted versus the current shows a well behaved linear relationship within the nominal settings for the two beam energies used in Q _{weak} . The right figure shows a map of magnetic field of one half of the dipole and shows the relationship to the beam direction z and the vertical axis y . We can see the relatively uniform behavior under minimal deviations from the central regions.	77
5.7	A simplified layout of the optical path of the Compton laser. Additional components not described by this thesis were not drawn.	79
5.8	The Pound-Drever-Hall technique uses an error signal of a reflected signal from a band outside the Fabry-Pérot passband to lock the cavity to a laser. A clean scope trace of the error signal is seen in fig. 5.8b. The effectiveness of the locking technique is evident in the scope traces of the transmitted and reflected power from the cavity is seen on fig. 5.8a. The left trace shows good locking with low reflection and stable transmission, while the right shows a bad lock where the reflected power is large and noisy and the transmitted power decreases and has broad noise. . . .	80
5.9	A figure showing the relationship of laser polarization to the setting on the quarter-wave plate and the half-wave plate, taken from [61]. By comparing both plots we see the inverse relationship between the degree of circular polarization to linear polarization. The third figure shows the corresponding residual reflected power measured.	82
5.10	The electron detector was housed inside an aluminum can that sits atop the beamline. In this picture, looking at it from below, we see the four mounted planes, where the inner dark gray rectangles are the actual diamond strips.	84
5.11	A two parameter fit and final Run II electron detector based polarizations.	85

5.12	A drawing of the stacked crystals attached to the PMT. The PMT is a little larger than the four stacked crystals.	86
5.13	Photographs of the photon detector crystals as they are wrapped before placed inside the enclosure (left) and after inserted inside a thermally cooled enclosure (right).	87
5.14	Timing diagram of the Compton DAQ showing the main trigger from the MPS and the output pulse from the HAPTIB that defines the integrating window.	90
5.15	Flow chart illustrating the steps used in processing the data. Starting with the initial acquisition at the top and ending with the final results at the bottom.	103
6.1	Left: The calibrated Unser current for run 22617 plotted as a function of time. The horizontal dashes are caused by the bit-level precision of the scalers. Right: The difference between the calibrated BCM1 and Unser measured currents.	107
6.2	An example of the five minute beam motion as it scans the vertical axis to identify central position of the laser, as measured by BPM 3P02A, which is upstream of the IP. The horizontal axis corresponds to the time since the start of the run (23678). A comparison between the Scaler calibrated data (left) and the EPICS values retrieved from the Hall C Archiver (center). The corresponding current normalized photon rates are also shown (right).	110
6.3	During special periods where the beam is re-centered on the photon target by scanning purely in the vertical direction, BPM 3P02A shows evidence of horizontal motion. This is seen both on the data (left) as well as the accelerator readouts (center). However, by introducing a small angle offset of just -1° the horizontal component disappears, which points to an offset as the likely culprit.	111
6.4	By following the procedure of [77] we can get the density of power incident on the photon detector as a function of the out of plane angle ψ (left). By integrating over all ψ and the entire helicity window we can get the expected density of Synchrotron photons (right).	114
6.5	Scarring of the copper beam pipe exit window after two years or running at high current. The narrow burn mark is a characteristics signs Synchrotron radiation.	115

6.6	Figures showing the rates of particles incident on the photon detector. A simulation of the electron beam interacting with the residual gas in the beam pipe is show on the left. Show on the right are the rates seen in run 24267. The simulated rates are not sufficient to explain the background rates seen in run 24267.	116
6.7	An example of the Accum0 yields in units of integrated adc values. The top image shows the yields without pedestal corrections applied. The bottom image shows the yields after pedestal corrections were applied. Both images have quality cuts applied which are evident by the gaps in the data. The horizontal axis corresponds to a unit of time.....	120
6.8	Shown here are the beam normalized slug averaged pedestal corrected yields (in units of integrated ADC channels per μA). The blue close circles correspond to the laser-on periods with no background subtraction. The red open circles are the laser off periods averaged by either side of the corresponding laser-on period. The pink closed squares correspond to the background subtracted real Compton scattered yields.....	121
6.9	The rates seen by the “background” scintillator averaged by slug. No significant differences seen between the laser-on states and the laser off states, confirming that this scintillator only sees background signal. The running period with a beam energy of 879 MeV are not shown.....	122
6.10	An illustration of two full snapshots containing 256 contiguous samples, where the main photon trigger is seen around sample 115 and the magenta box highlights the region used to determine the pedestal. The figure to the right shows a good clean single photon event useful for the pedestal determination, while the one on the right shows multiple photon events, one of which is in the pedestal region and must be discarded.	124
6.11	Pedestals vs time for run 24267. Each point corresponds to the average of the first 100 samples for all snapshots in a given laser state.	125
6.12	Run II pedestals from January 27 to May 15, 2012 and averaged by slug. The cause of drastic change in pedestal from the earlier running period (before run 24150) compared to the later periods is not known.....	127
6.13	Shown here are the Run II helicity differences and the asymmetries, averaged into groups of ~ 30 runs. Only statistical errors shown.	128
6.14	The average Accum0 yield (left) and helicity difference (right) per helicity quartet for run 24846 in units of integrated adc channels. The laser off data was removed from these histograms. No other corrections were applied for pedestal nor were the background contributions subtracted out. This run was 96 minutes long.	129

6.15	Shown here are the background helicity differences and the asymmetries, averaged into groups of ~ 30 runs. Only statistical errors shown.	130
6.16	Showing the correlation of the Accum0 yields vs helicity differences for run 24846. No corrections for pedestal or background subtraction have been applied. There is no correlation between the two and so the variations can be treated as un-correlated.	133
6.17	Optical properties of the PbWO_4 crystal showing the emission, transmission spectra [81] and the efficiency of the Hamamatsu PMT[65] (left). The integral of the emission spectrum has been normalized to 100 % and for display purposes were multiplied by 50 in this graph. The index of refraction averaged over the ordinary and extraordinary components from[82] (right).....	136
6.18	An example of the distribution of the integrated signal of individual photons in the snapshot data set. The black line corresponds to the sum of all incident photons on the detector. The blue and red histograms correspond to the laser on and off periods, respectively. The magenta histogram is the difference between the laser on and laser off histograms and should correspond to only Compton scattered photons. This includes the data from seven runs, whose average is 24835.	142
6.19	The distribution of the integrated signal due to the incident optical photons on the PMT of simulated Compton scattered photons. The full simulation (left) serves to fill in the gaps of the snapshot data which is restricted by a threshold. The discrepancy between the simulation and data at the lower voltages can be explained in part to the threshold of the discriminator. An example where the threshold is simulated (right) gives a better match. The remaining mismatch is thought to be associated with a non-linear response of the detector signal.	143
6.20	The time dependent beam polarizations as determined by the photon detector analysis. Statistical errors are shown on each point. The known systematic errors on the measured polarizations are shown as bands. The blue band corresponds to error contribution from the measured asymmetries, and the dark brown band corresponds to contributions from the analyzing power. The electron detector measured polarizations are also shown in red. The statistical errors for the electron detector are smaller than the size of the marker. The corresponding systematic error band for the electron detector is shown in red. Not shown are possible hidden errors on the photon detector results which contribute to the large discrepancy in results after run 24600.....	147

7.1	The slug averaged Run II raw asymmetries. Only No regression or linearity corrections applied. Only statistical errors shown.	157
7.2	The null asymmetries A_{NULL}^1 for all the Run II data. The average over the entire period for both the un-regressed raw asymmetries (left) and the asymmetries regressed under the Set10 scheme (right) are consistent with zero for the given errors. Only statistical errors are shown.	161
7.3	An example of the strong correlation between two background detectors[98]. The vertical axis is the asymmetry of the PMT-only detector and the horizontal is the average asymmetry in the US lumi. The units are in ppm.	166
7.4	Regressed asymmetries using set 10 regression scheme with an overlay of the the background correction. The background correction corresponds to $\Delta A_{\text{bbkg}} = C_{\text{bkgdet}}^{\text{md}} A_{\text{uslumi}}$	167
7.5	The determined fractional signal contribution of the Aluminum windows on the detector signal[104].	170
7.6	The measured asymmetries from a thick (~ 3.6 mm) pure Aluminum foil[105]. Only the statistical errors are shown. Asymmetries are regressed using regression scheme Set13 and are corrected for beamline scattering backgrounds and the beam polarization[105]. The sign of the asymmetry has been corrected for IHWP, Wien and spin precession.	171
7.7	Simulations of the total scattering rates for various processes are show on the left. The horizontal scale corresponds to the current on the spectrometer which is proportional to the scattering energy of the particle. The figure on the right shows the relative fractional yield for the inelastic scattering energy distribution[108].	172
7.8	The measured regressed asymmetries averaged into slugs. Regression scheme set 10 was used. Beamline background corrections and polarization corrections have been applied. Only statistical errors shown.	178
8.1	γZ -box diagram, in which an interaction exchanges two virtual particles, a photon and a Z -boson.	181
8.2	A projection of the five parameter fit to the world PVES data at low Q^2 into a 2D plot showing the reduced asymmetry as a function of Q^2 . ..	182

8.3	The constraints imposed the coupling constants C_{1u} and C_{1d} from the results of the world PVES and APV experiments. The vertical axis corresponds to the isoscaler ($C_{1u} + C_{1d}$) and the horizontal axis corresponds to the isovector ($C_{1u} - C_{1d}$). The green shaded area represent the constraints imposed by APV experiments with a 68 % confidence level, while the outer lines correspond to a 95 % confidence level. The purple ellipses corresponds to the constraints imposed by all the PVES experiments at 68 % and 95 % confidence levels, respectively. Finally the small red ellipse is the combination of PVES and APV data. The solid black dot is the Standard Model prediction.	185
B.1	The slug averaged pedestal corrected yields normalized to beam current of all the Photon Detector data from January to May 2012.....	192
B.2	The slug averaged determined pedestals for all the Photon Detector data from January to May 2012.	193
B.3	An illustration of the pedestal sensitivity to temperature. During a special period where the electronics's room AC malfunctioned for several hours, the pedestal slowly started to increase (pedestal is measured from the top down). The match in time with the measured room temperature (top) with the measured pedestal (bottom) track incredibly well.	194
B.4	Photon Detector Survey (November 08, 2011)	195
B.5	Photon Detector Survey (May 25, 2012)	196
D.1	The measured upstream Lumi asymmetries. Note, these are given in ppm	200
D.2	Background correction due to beamline scattering applied on a slug by slug basis.	201

Chapter 1

Introduction

This dissertation will cover an experimental technique in use by the Q_{weak} Collaboration to test the leading theory which describes particle interactions. The roughly 100 members of the collaboration range from professors, staff scientists, a dozen postdocs and 23 Ph.D. students, of which I am one. The goal of the collaboration was to measure the weak charge of the proton, which is a weak force analogue to electromagnetic charge. The concept of a weak charge will be described in Chapter 1, where I will provide a basic overview of the leading theory known as the Standard Model. An overview of how the weak charge can be used to test the Standard Model will be presented in Chapter 2.

To measure the weak charge, the collaboration designed and built custom detectors which were installed in Hall C of the Thomas Jefferson National Accelerator Facility, in Newport News, Virginia. The polarized electron beam from the on-site accelerator, the Continuous Electron Beam Accelerator Facility (CEBAF), was used to provide a GeV scale electron source. The experimental apparatus and the CEBAF accelerator will be described in Chapter 3.

My work with the collaboration focused on measuring the polarization of the electron beam via detection of a photon which undergoes Compton scattering. The theory and description of the Compton polarimeter will be detailed in Chapter 4. The results of my analysis will be detailed in Chapter 5. Given the poor statistics of this method, and an underlying systematic effect, the decision was made not to use these measurements for the final experimental result.

The remaining chapters will cover a blinded analysis and results of the weak charge of the proton. Chapter 6 will introduce the concept of blinding, and will outline my independent analysis of the Q_{weak} data set. Lastly, Chapter 7 will summarize the results of this blinded analysis, and of the analysis of Chapter 5.

Chapter 2

Basic Standard Model Theory

At present, the theory with the greatest success in describing the interactions of the very minute fundamental particles is known as the Standard Model (SM). This theory is a mix of both conceptual and mathematical models and relies on the determination of fundamental symmetries in our universe. Conceptually, it includes a classification of particles into one of three main groups: leptons, quarks and Gauge bosons as seen on fig. 2.1, where there are three generations of both leptons and quarks. In the SM the gauge bosons are the force carriers, with the gluons being the carriers of the strong force, and only couple to quarks and other gluons. The remaining are the electromagnetic (γ), and the weak Z , and W carriers, which combined make up the electro-weak interaction. Noticeably absent is a gravitational carrier, and this is perhaps our first clue as to the limited scope of the SM. The lone particle on the top right of fig. 2.1 is the Higgs boson, which plays a role in particles acquiring mass. The subtle shading of fig. 2.1 maps the allowed couplings of quarks and leptons to the four gauge bosons. To summarize, the quarks couple to all gauge bosons, while the electron (e), muon (μ) and tau τ couple with all except for gluons. Meanwhile

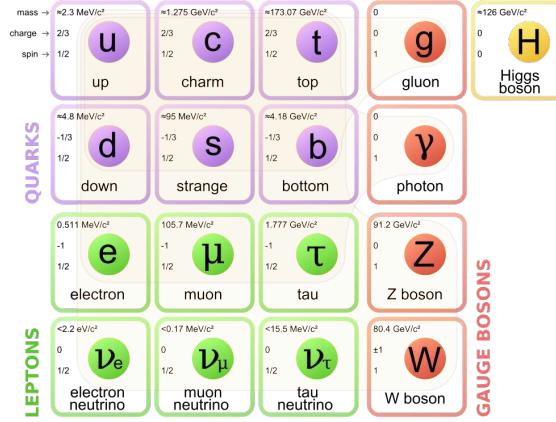


Figure 2.1: An illustration of the particles included in the Standard Model. It shows the three main groups: leptons, quarks and Gauge bosons, the first two of which have three generations. The top right particle is the Higgs boson. Reproduced from Wikipedia[1].

their corresponding neutrinos ν_e , ν_μ and ν_τ respectively, couple only via the weak gauge bosons Z and W .

2.1 Standard Model Mathematical Formulation

The interactions between quarks and leptons is mediated by an exchange of a “virtual” gauge boson, where the use of virtual here simply means that the exchanged boson can not be observed. The coupling to a boson defines the type of interaction two particles may have. For example, the quarks couple to all bosons and can interact with each other via exchanging of any virtual gluon, photon or weak boson. However quarks cannot interact with electrons via the strong force, since electrons do not couple to the gluons. Instead, quarks interact with electrons only via an exchange of a photon or a weak boson.

The mathematical description of the Standard Model is based on the ability to

write down a Lagrangian \mathcal{L} of an arbitrary system whose action is given by

$$S \equiv \int \mathcal{L}(q : q_1, \dots, q_n) d^n q,$$

for the given coordinates q_i . The minimization of the action $\delta S = 0$ gives the equations that describe the system. In a “classical” sense, the Lagrangian can be constructed from the kinetic and potential energies of the system and the equations of motion can be extracted by minimizing the action. We then require that the Lagrangian be invariant under some transformations, which may require that we rewrite the Lagrangian by adding extra terms to make it invariant. As an example, we consider the Dirac Lagrangian for fermions given by its kinetic and potential terms[2]

$$\mathcal{L}_{\text{Dirac}} = \bar{\psi}(i\gamma^\mu \partial_\mu - m)\psi, \quad (2.1)$$

where ψ represents the fermion wave function, m the fermion mass, and γ^μ are the gamma matrices with an implicit sum over $\mu = 0, 1, 2, 3$. It is evident that both Lagrangian and action are invariant under a transformation involving a constant phase offset of the form $\psi \rightarrow e^{i\phi}\psi$. However, should the offset also be position dependent as in the case $\phi \rightarrow \phi(\mathbf{x}; t)$, we find the Lagrangian no longer invariant. However, we can still make it invariant by adding an extra term A_μ to the Lagrangian and redefining the derivative ∂_μ to be covariant of the form[2, 3]

$$\partial_\mu \rightarrow D_\mu \equiv \partial_\mu - iqA_\mu,$$

where q is the coupling (strength) of this new vector field. To complete this example,

we also note that the vector A_μ must have a gauge invariant term given by[3]

$$-\frac{1}{4} (\partial^\mu A^\nu - \partial^\nu A^\mu) (\partial_\mu A_\nu - \partial_\nu A_\mu), \quad (2.2)$$

where the $-1/4$ is an overall normalization. In this example, the requirement that the Lagrangian be invariant under a constant phase shift α represents an example of a global symmetry. The requirement that it be constant under a position dependent phase shift $\alpha(\mathbf{x}; t)$ corresponds to a local symmetry.

As a consequence, the Standard Model is described by the gauged symmetries of an $SU(3) \times SU(2) \times U(1)$ vector space[4]. I will reproduce equation 2.1 of Burgess and Moore[4, page 54] in part, since it better illustrates the features of the Standard Model:

$$\begin{array}{ccc} SU_c(3) & \times & SU_L(2) & \times & U_Y(1) \\ \downarrow & & \downarrow & & \downarrow \\ 8 G_\mu^\alpha & & 3 W_\mu^\alpha & & 1 B_\mu \end{array} \quad (2.3)$$

Where the authors use the subscript “c” to denote that the generators of the group G_μ^α correspond to “color,” the number represents the eight linear combinations of color of this space, and $\alpha = 0, 1, 2$ represents the three distinct particles. These particles are the gluons that couple with the quarks, and the color is meant as the strong force analog to the electromagnetic charge.

Setting the strong interaction aside, we shift focus to the remaining groups, namely, $SU_c(3) \times U_Y(1)$ which represents the work of Glashow, Weinberg and Salam developed in the late 1960’s. In the notation adopted from[4] the “L” illustrates that only left-handed fermions are included in this theory and that the unitary group $U_Y(1)$ describes fermions with weak hypercharge quantum number.

2.2 Unification of Electromagnetic and Weak Interactions

We can write the mathematical formulation that gives rise to the four “electro-weak” bosons in fig. 2.1, by writing the corresponding electro-weak Lagrangian that contains the mass terms of the four gauge fields W_μ^α and B_μ [4]

$$\mathcal{L}_{\text{EW}}^{\text{MT}} = -\frac{1}{8}g'^2v^2|W_\mu^1 - iW_\mu^2|^2 - \frac{1}{8}v^2(g'^2B_\mu - g^2W_\mu^3)^2, \quad (2.4)$$

where g' and g are the field coupling constants and v is the vacuum expectation value (v.e.v). We find that the gauge fields W_μ^1 and W_μ^2 are mixed together and entirely separate from the other two W_μ^3 and B_μ gauge fields which are subsequently mixed together. This fact gives us the flexibility of treating them individually.

One can “read off” the mass of the gauge fields by comparing the quadratic terms to the kinetic term of an arbitrary Lagrangian of the form

$$-\frac{1}{2}M^2K^\mu K_\mu, \quad (2.5)$$

where M is the corresponding mass. For example, after expanding the first part of eq. (2.4) and comparing the quadratic term of $W_\mu^1 W^{\mu 1}$ to eq. (2.5) we get

$$-\frac{1}{2}M^2 = -\frac{1}{8}g'^2v^2 \quad \Rightarrow \quad M^2 = \frac{1}{4}g'^2v^2. \quad (2.6)$$

Similarly, we find that the mass term of $W_\mu^2 W^{\mu 2}$ is exactly the same. We are free to write these fields in a form that makes them mass eigenstates and invariant under

electromagnetic charge Q , with $Q = T_3 + Y$, where T_3 is the third component of the $SU_c(3)$ isospin and Y is the weak hypercharge[4]. We define these two fields as real charged boson vectors which are orthogonal in this field as[5]

$$W_\mu^+ \equiv \frac{1}{\sqrt{2}} (W_\mu^1 - iW_\mu^2) \quad \text{and} \quad W_\mu^- \equiv \frac{1}{\sqrt{2}} (W_\mu^1 + iW_\mu^2), \quad (2.7)$$

which are the corresponding W bosons in fig. 2.1 with opposite charge and whose mass is identical and determined from eq. (2.6) as

$$M_{W_\mu^\pm} = \frac{1}{2}g'v. \quad (2.8)$$

Similarly we follow the same procedure for the two remaining W_μ^3 and B_μ gauge fields in the second part of eq. (2.4). We define two new vectors to be the eigenmass states described by the fields as such

$$\begin{aligned} Z_\mu &= -B_\mu \sin \theta_W + W_\mu^3 \cos \theta_W \\ A_\mu &= B_\mu \cos \theta_W + W_\mu^3 \sin \theta_W, \end{aligned} \quad (2.9)$$

where θ_W is the Weinberg angle (or weak mixing angle) defined by

$$\sin \theta_W = \frac{g}{\sqrt{g^2 + g'^2}} \quad \text{and} \quad \cos \theta_W = \frac{g'}{\sqrt{g^2 + g'^2}}, \quad (2.10)$$

Since we are interested in reading off the mass terms of these two bosons, we trans-

form back to W_μ^3 and B_μ with the following relation

$$\begin{pmatrix} B_\mu \\ W_\mu^3 \end{pmatrix} = \begin{pmatrix} \cos \theta_W & -\sin \theta_W \\ \sin \theta_W & \cos \theta_W \end{pmatrix} \begin{pmatrix} A_\mu \\ Z_\mu \end{pmatrix}, \quad (2.11)$$

and apply to the second part of eq. (2.4) to get

$$-\frac{1}{8}v^2 [-Z_\mu(g' \cos \theta_W + g \sin \theta_W) + A_\mu(-g' \sin \theta_W + g \cos \theta_W)]^2. \quad (2.12)$$

Comparing the two corresponding quadratic terms with eq. (2.6) we get the mass terms of the Z_μ and A_μ as

$$M_{Z_\mu} = \frac{1}{2}v(g' \cos \theta_W + g \sin \theta_W) \quad (2.13)$$

$$M_{A_\mu} = \frac{1}{2}v(-g' \sin \theta_W + g \cos \theta_W)$$

where if we substitute $\cos \theta_W$ and $\sin \theta_W$ from eq. (2.10) we find that $g' \cos \theta_W + g \sin \theta_W = \sqrt{g^2 + g'^2}$ and more importantly, that $-g' \sin \theta_W + g \cos \theta_W = 0$. Which means that the A_μ field is massless and the Z_μ field is massive and given by

$$M_{Z_\mu} = \frac{1}{2}v\sqrt{g^2 + g'^2}. \quad (2.14)$$

We conclude by recognizing that the Z_μ field is represented by the massive and chargeless mediator of the weak interaction Z^0 boson, while the massless and also chargeless A_μ field represents the electromagnetic interaction mediated via the γ .

With this, we complete the unification of the electromagnetic and weak interactions.

2.3 Parity and Left-Handed Fermions

While one would envision that a theory that couples to both left and right handed fermions can be built, there is no direct evidence that a right handed neutrino exists[6] and, as a result, the theory was written to match that of observation.

To understand the consequence of having no right-handed neutrino, we first consider an operator of “parity” \mathcal{P} that flips the sign of coordinates in a vector. Quantities that are invariant under such a transformation are said to be parity conserving, likewise those that are not invariant under such a transformation are said to be parity violating. For example consider a three-momentum vector $\mathbf{k}(x, y, z)$ given by its spatial coordinates x , y and z and its corresponding parity-operated vector $\mathbf{k}' \equiv \mathcal{P}\mathbf{k}$. By working out the mathematics we see that the two vectors are the same up to a sign difference

$$\mathbf{k}'(x, y, z) = \mathcal{P}\mathbf{k}(x, y, z) = \mathbf{k}(-x, -y, -z) = -\mathbf{k}(x, y, z). \quad (2.15)$$

Furthermore, while their direction is no longer their same, the parity operator preserves the magnitude of the vectors as $|\mathbf{k}| = |-\mathbf{k}|$.

Now we consider a scenario in which the actions of parity do not preserve a general characteristic of the system. Take the case of mirror images, where on fig. 2.2a we have a key-hole that opens up a box and on fig. 2.2b we have its mirrored image. While the two key-holes look similar, we find that the key that fits the key-hole on the left no longer matches that of the right and as a consequence we are unable to

open up the box on the right.

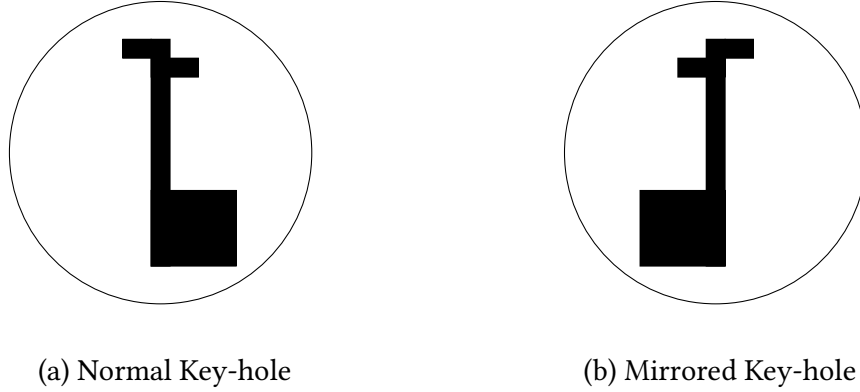


Figure 2.2: An example illustration showing the effects on a key-hole (left) if the parity operator \mathcal{P} where to mirror they key-hole (right). In this case, the key for the hole on the left would not fit the key on the hole on the right, despite their similarities.

One might believe that only parity-conserving transformations should be allowed. However, in 1956 Tsung-Dao Lee and Chen-Ning Yang questioned this notion citing no experimental evidence that either confirms nor contradicts the need for parity conservation[7]. They approached the experimentalist Chien-Shiung Wu with a proposal to test this notion. In just a few short months Wu and colleagues at the United States National Bureau of Standards, now in present day as NIST, were able to experimentally confirm that parity is not conserved in the β decay of ^{60}Co [8]. Wu and colleagues placed a polarized ^{60}Co nucleus in a magnetic field and observed the rate of decay. They then reversed the magnetic field, and hence the polarization and measured the rates again. They found a discrepancy between the two polarization states that should not be allowed in a parity conserving system[8].

We now know that ^{60}Co undergoes β decay in which a neutron decays into a proton by emitting an electron e and an electron anti-neutrino $\bar{\nu}_e$. If we were to

consider the magnetic field orientation in terms of chirality, then we would expect a left-handed electron e_L to be emitted with a right-handed anti-neutrino $\bar{\nu}_R$. In the reverse case, where the electron is right-handed e_R the corresponding anti-neutrino is then expected to be left-handed $\bar{\nu}_L$. By the decay preferring only one orientation, in this case the left-handed electron, means that the case with the left-handed anti-neutrino is not allowed. The left-handed anti-neutrinos are thought to be equivalent to the right-handed neutrino, which means if $\bar{\nu}_L$ is not allowed to exist, then the corresponding ν_R is also not allowed.

2.4 Tests and Limits of the Standard Model

Since its formulation in this final form in the early 1970's, the Standard Model has been the most successful field theory in the description of fundamental particles and their interactions. I am aware of no definitive proof of a false prediction made by the Standard Model. But with the success of a theory comes the implicit need to test and find the limits of the theory.

As a consequence, the Standard Model has been tested, in some way, with each and every experiment that relies on its predictions. Furthermore, while the introduction of some particles, such as the electron and the electron neutrino, were introduced into the Standard Model based on observation, others, like the weak W and Z boson were not. However, within only a few years of the theoretical developments of the Glashow-Weinberg-Salam electro-weak theory, evidence of possible interactions mediated by the W and Z boson were observed at the European Organization for Nuclear Research (CERN), in Geneva, Switzerland. In 1973, researchers

at CERN reported the first evidence of weak mediated interactions of both charge and neutral currents within the Gargamelle bubble chamber experiment[9, 10]. It would take another decade before advances in accelerators allowed for proton and anti-proton beams to be accelerated independently to 270 GeV and collided together to provide the first direct observations of the Z^0 [11] and W^\pm [12–14] by the UA1 and UA2 collaborations at CERN. The observed masses of the Z^0 and the W^\pm at that time of $(95.6 \pm 1.4) \text{ GeV}/c^2$ and $(80.9 \pm 1.5) \text{ GeV}/c^2$ respectively[14] were consistent with Standard Model predictions.

The last remaining piece of the electro-weak theory of the Standard Model eluded physicists for nearly three more decades. The Higgs boson is described by the Standard Model as the mediator of the Higgs field and the process by which the electro-weak gauge bosons gain mass, and in the case of the photon, the reason why it must be massless. Using the Higgs field we were able to write the mass terms of the electro-weak Lagrangian in eq. (2.4). However, without evidence of the Higgs boson one can question the validity of the Standard Model.

Fortunately, after a multi-decade wait, experimenters at the Large Hadron Collider (LHC) accelerator in CERN reported evidence of a massive spin-less boson of 125 GeV detected at both by the ATLAS experiment[15] and the Compact Muon Solenoid (CMS) experiment[16] in summer of 2012.

At this point, and with the test of time, one may believe that there is no new physics to be found beyond what is predicted by the Standard Model. However, one must be careful not to confuse the absence of evidence as evidence of absence. Since it took about three decades to reach the energies of 7 TeV to 8 TeV to find direct signs of the Higgs boson, it is equally likely that any new physics is hidden at much greater

energies. Additionally, we know for a fact that the Standard Model is limited as it has no suitable mechanism for including gravity. Even more recently, the Standard Model may not be sufficient to explain the observations of both dark energy and matter. It further cannot tell us with certainty that there cannot be a fourth generation. One may be willing to accept these phenomenon as simply outside of the scope of the Standard Model. There is, however, evidence to suggest that the Standard Model may be describing the neutrino inaccurately.

More critical to the validity of the Standard Model, however, is the fact that the Standard Model, as developed from the mid 1960's to the mid 1970's, requires that the neutrinos be exactly massless. This is due to the fact that no right-handed neutrinos (or left-handed anti-neutrinos, for that matter) have been observed[6]. Both left and right handed fermions are required for interactions with the Higgs field to bring about mass terms. The notion of a massless neutrino, however, was challenged by the measurements of the flux of electron-neutrinos from the Sun, believed to be due to the carbon to nitrogen fusion in the sun[17]. This lead to a description by Pontecorvo, whom already had a model for neutrino oscillations as early as 1958, and V. Gribov for possible extensions to the Standard Model¹ that would allow the neutrinos to have mass[18].

The remainder of this chapter will discuss the weak analog to the electromagnetic charge. This will start the motivation for the Q_{weak} experiment in the next chapters.

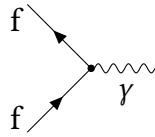
¹Which, at the time of their publication, the Standard Model was still relatively new and severely under-tested.

2.4.1 Weak Charges

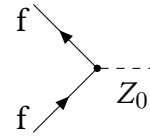
Since electromagnetism has been well known for more than a century, the concept of electric charge in this context is well defined. We want to have an equivalent analog weak charge to incorporate into the description of the relatively new² electroweak interactions. Take the part of the invariant Standard Model Lagrangian that contains only the fermion kinetic terms[4]

$$\mathcal{L}_{\text{EW}} = -\frac{1}{2}\bar{L}_m \not{D} L_m - \frac{1}{2}\bar{E}_m \not{D} E_m - \frac{1}{2}\bar{Q}_m \not{D} Q_m - \frac{1}{2}\bar{U}_m \not{D} U_m - \frac{1}{2}\bar{D}_m \not{D} D_m, \quad (2.16)$$

where the lepton terms L_m and E_m are the left and right terms respectively, Q_m the electromagnetic terms of the quarks and the corresponding up- and down-like terms are in U_m and D_m respectively and we used the Feynman slash notation $\not{D} \equiv \gamma^\mu D_\mu$. We are only interested in the terms that interact via the neutral gauge field A_μ fig. 2.3a or a neutral weak boson Z_μ fig. 2.3b.



(a) EM Interaction (γ -exchange)



(b) Weak Interaction (Z^0 -exchange)

Figure 2.3: The two neutral current exchange vertexes where either a virtual photon (left) or a weak neutral boson (right) is exchanged, but leaves the two fermions the same.

We first expand eq. (2.16) in terms of the mass eigenstates and select out only the neutral current terms of W_μ^3 and B_μ to get[4]:

²Relative in comparison to electromagnetism.

$$\mathcal{L}_{EW}^{\text{NC}} = \sum_i \left[-\bar{\psi}_i \gamma^\mu P_L (-ig' W_\mu^3 T_3 - ig B_\mu Y_L) \psi_i - \bar{\psi}_i \gamma^\mu P_R (-ig B_\mu Y_R) \psi_i \right], \quad (2.17)$$

where ψ_i is any given fermion spinor, and

$$P_L = \frac{1}{2} (1 - \gamma^5) \quad \text{and} \quad P_R = \frac{1}{2} (1 + \gamma^5), \quad (2.18)$$

are the corresponding left (right) projection operators. Now use eq. (2.11) to rewrite in terms of the Z_μ and A_μ gauge fields. We also make use of the results for the cancelled A_μ mass term from before to define a new constant

$$e \equiv g \cos \theta_W = g' \sin \theta_W \quad (2.19)$$

and write the above equation as

$$\begin{aligned} \mathcal{L}_{EW} = \sum_i & [ig' \cos \theta_W \bar{\psi}_i \gamma^\mu P_L Z_\mu T_3 \psi_i + ie \bar{\psi}_i \gamma^\mu P_L A_\mu T_3 \psi_i \\ & + ie \bar{\psi}_i \gamma^\mu P_L A_\mu Y_L \psi_i + -ig \sin \theta_W \bar{\psi}_i \gamma^\mu P_L Z_\mu T_L \psi_i \\ & ie \bar{\psi}_i \gamma^\mu P_R A_\mu Y_R \psi_i - ig \sin \theta_W \bar{\psi}_i \gamma^\mu P_R Z_\mu Y_R \psi_i]. \end{aligned} \quad (2.20)$$

At this point, we recall $Q = T_3 + Y$, but, given that there are no right-handed neutrinos, the weak hypercharge for the right-handed fermions is just the electromagnetic charge Q , and so $Q = T_3 + Y_L = Y_R$. Now collect only the terms of A_μ and rewrite $Y_{L,R}$

in terms of Q to get

$$\mathcal{L}_{\text{EM}} = \sum_i ieQ_i \bar{\psi}_i \gamma^\mu (P_L + P_R) A_\mu \psi_i = \sum_i ieQ_i \bar{\psi}_i \gamma^\mu A_\mu \psi_i, \quad (2.21)$$

where we used $P_L + P_R = 1$. At this point, we can also see that the choice of e was not accidental, as it represents the electromagnetic coupling constant, and we can also define the electromagnetic neutral current term as

$$j_\mu^Y \equiv Q_i \bar{\psi}_i \gamma^\mu \psi_i \quad (2.22)$$

The remaining neutral current electroweak terms can be written simplified as

$$\mathcal{L}_{\text{weak}} = \sum_i i(g' \cos \theta_W + g \sin \theta_W) \bar{\psi}_i \gamma^\mu P_L Z_\mu \psi_i - igQ \sin \theta_W \bar{\psi}_i \gamma^\mu Z_\mu \psi_i, \quad (2.23)$$

with a bit of manipulation, and by pulling out a $g'/(4 \cos \theta_W)$ term we can write

$$\mathcal{L}_{\text{weak}} = \frac{ig'}{4 \cos \theta_W} \sum_i \left[(\cos^2 \theta_W + \sin^2 \theta_W) T_3 \bar{\psi}_i \gamma^\mu P_L Z_\mu \psi_i - \sin^2 \theta_W Q \bar{\psi}_i \gamma^\mu Z_\mu \psi_i \right]. \quad (2.24)$$

Simplify $\cos^2 \theta_W + \sin^2 \theta_W = 1$ and now define two coupling constants g_V and g_A as such

$$g_V \equiv 2T_3 - 4Q \sin^2 \theta_W \quad \text{and} \quad g_A \equiv 2T_3, \quad (2.25)$$

and plug back into eq. (2.24) to get

$$\mathcal{L}_{\text{weak}} = \frac{ig'}{4 \cos \theta_W} \sum_i \left[\bar{\psi}_i \gamma^\mu (g_V - g_A \gamma^5) Z_\mu \psi_i \right]. \quad (2.26)$$

	Q	T_3	$g_V (2T_3 - 4Q \sin^2 \theta_W)$	$g_A (2T_3)$
e	-1	-1/2	$-1 + 4 \sin^2 \theta_W$	-1
u	+2/3	+1/2	$+1 - 8/3 \sin^2 \theta_W$	+1
d	-1/3	-1/2	$-1 + 4/3 \sin^2 \theta_W$	-1
s	-1/3	-1/2	$-1 + 4/3 \sin^2 \theta_W$	-1

Table 2.1: A table listing the electromagnetic charge Q , the third component of the $SU_c(3)$ isospin T_3 and the weak vector and axial-vector “charges.”

Like in the case for the electromagnetic case, we can also write down a charge current due to the weak boson Z^0 as

$$j_\mu^{Z^0} \equiv \bar{\psi}_i \gamma^\mu (g_V - g_A \gamma^5) \psi_i. \quad (2.27)$$

These relations represent an important feature for this thesis, as it lays out the foundations for the fermion interactions via exchange of electroweak currents. Equally important, is that we can now create a weak charge analog to the electromagnetic charge. In eq. (2.22) the electromagnetic charge of the fermion is specified by Q_i . Hence, by comparing it to eq. (2.27) we can then deduce that the two coupling constants g_V and the axial g_A represent the vector and axial-vector components of the weak “charge” of the fermion, respectively. In table 2.1, I have tabulated the electromagnetic and weak charges of the electron and the three “light” quarks, the up, down and strange quark.

In eq. (2.25) we also notice that the vector weak charge component is directly dependent on the weak mixing angle. If we rewrite the weak mixing angle into the

following form [6]

$$\sin^2 \theta_W \approx 1 - \frac{M_W^2}{M_{Z^0}^2}, \quad (2.28)$$

where M_W and M_Z are the masses of the weak charged and neutral gauge boson, respectively, we can determine the scale of the weak mixing angle by using the masses of the electroweak gauge bosons. For example, by using the current PDG 2014 values for the electroweak gauge masses, $M_W = (80.385 \pm 0.015) \text{ GeV}/c^2$ and $M_{Z^0} = (91.1876 \pm 0.0021) \text{ GeV}/c^2$ [6], we find that $\sin^2 \theta_W \approx 0.2229$. In calculating this value, I have ignored any higher order corrections, but we can use this value to set the scale. In particular, one useful rule of thumb is to note that $\sin^2 \theta_W \approx 1/4$, which when using the axial vector coupling constant of the electron from table 2.1 means the coupling constant is small. This will be useful in the discussion of the weak charge of the proton in the following chapter.

Chapter 3

The Q_{weak} Experiment

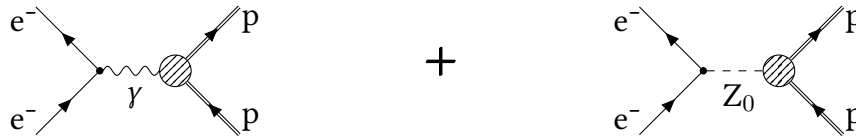
The previous chapter introduced the Standard Model and a weak analog to the electromagnetic charge. In this chapter, I will introduce the Q_{weak} Experiment and describe the physics behind the experiment. The goal of the Q_{weak} Experiment is to test the limits of the Standard Model by determining the weak charge of the proton Q_w^p . In this chapter, I will derive Q_w^p similar to the up and down quark weak charges in the previous chapter. To reach Q_w^p the Q_{weak} Experiment made precise measurements of a longitudinally polarized electron elastically scattering off a stationary un-polarized proton in the lab frame.

In this chapter, I will introduce electron scattering and the concept of elastic scattering. I will also detail the precise measurements of the elastic-proton scattering required to precisely determine Q_w^p . While $M_{Z^0} = (91.1876 \pm 0.0021) \text{ GeV}/c^2$ [6] and the strength of the interaction is proportional to the inverse of $M_{Z^0}^2$, I will show how the relatively low energy Q_{weak} Experiment ($\sim 1 \text{ GeV}$) can be competitively sensitive to interactions at the higher M_{Z^0} energy scale.

3.1 Elastic Electron Scattering

As I showed in the introductory chapter, electrons only couple to the electroweak gauge bosons. As such their interactions tend to be much simpler than those of quark-on-quark interactions which may happen on an ion to ion collision. This is because, unlike gluons, the electroweak gauge bosons do not couple to each other and requiring smaller subset of loop corrections.

We can further simplify the process by requiring that the interaction be elastic. In elastic scattering there are no distinct intermediate states and the final states of the interaction are the same as the initial states as illustrated by the Feynman diagrams infig. 3.1.



(a) Electromagnetic Neutral Interaction

(b) Weak Neutral Interaction

Figure 3.1: The two ElectroWeak Neutral Current interactions at tree level are due to the exchange of a photon (left) and a massive Z_0 boson (right). In elastic scattering we require that all states, initial, final and any intermediate, be the same.

To simplify the discussion, let me introduce a bit of nomenclature. We can write electron interactions in the following form $A(e, x_i \dots x_n)X$ which can be split up into two parts. The left part “ $A(e)$ ” indicates the initial state of the system, where the A represents the target. Conversely right side “ $x_i \dots x_n)X$ ” represents the final state of the interaction. Anything within the parenthesis is a directly measured or observed quantity. For example, $^{208}\text{Pb}(e, e'p)^{207}\text{Tl}$ is an inelastic interaction where a proton was stripped off the ^{208}Pb nucleus and one directly observes the scattered electron

and ejected proton. In Q_{weak} we only observed the scattered electron and so the interaction is written as

$$^1\text{H}(\mathbf{e}, \mathbf{e}')p, \quad (3.1)$$

where the $^1\text{H} \rightarrow p$ highlights that we were scattering off an atomic hydrogen target and we have ignored any atomic interactions in the final state¹. Also highlighted is the fact that we measure the polarization of the incident electron \mathbf{e} but the final state polarization of the scattered electron \mathbf{e}' is not observed. Since we do not directly observe the recoil proton, we need a method to determine that the interaction was truly elastic without and that there were no intermediate states in the interaction. We can do this by writing down the kinematics of an elastically scattered interaction.

The two-body electron-proton interaction of eq. (3.1) can be described by a 2D plane as in fig. 3.2, where \mathbf{p}_e is the incident electron three-momentum, \mathbf{p}'_e and \mathbf{p}_p

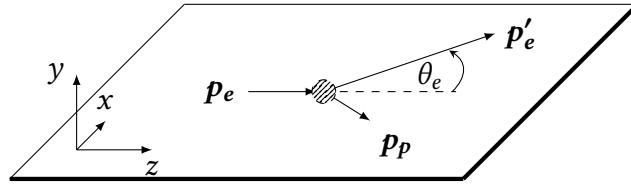


Figure 3.2: The kinematics of a two-body interaction can be simplified into a 2D plane, as shown here in the laboratory coordinate system. This interaction is fully symmetric around the out of plane angle $\phi \in [0, 2\pi]$ defined by rotations around the $+z$ axis.

are the scattered electron and proton three-momenta, respectively, and θ_e is the in-plane scattering angle of the electron. We can relate the initial and final terms by imposing energy and momentum conservation, which for elastic scattering takes

¹Atomic interactions, such as ionization, are in the low $\sim\text{eV}$ range while the incident energies in our experiment are of the $\sim\text{GeV}$ range and so can be ignored without consequence.

the following form

$$E_e + E_p = E'_e + E'_p, \quad (3.2)$$

$$\mathbf{p}_e + \mathbf{p}_{pi} = \mathbf{p}'_e + \mathbf{p}_p. \quad (3.3)$$

We can further relate energy and momentum via the relativistic relation $E^2 = (pc)^2 + (mc^2)^2$. To avoid having to write out the speed of light (c) explicitly, we redefine the units of momentum $[p]$ and mass $[m]$ in terms of units of energy, like so $[p] = \text{MeV}/c$ and $[m] = \text{MeV}/c^2$, and so we can rewrite the energy to momentum and mass relation as $E^2 = p^2 + m^2$.

If we use a stationary target the $\mathbf{p}_{pi} = 0$ and the initial energy part of the proton becomes $E_p = m_p$, in the appropriate units discussed above. An incident electron with total energy of $E_e \sim 1 \text{ GeV}$ is considered to be traveling at an ultra relativistic energies. The mass of the electron at rest is $m_e \approx 0.511 \text{ MeV}/c^2$ [6] and in comparison to an ultra relativistic electron is $m_e \ll E_e$ and can be dropped from the equations. Therefore we can write the corresponding energies of the electron as $E_e \approx |\mathbf{p}_e| = p_e$. And so the equations of ?? can be re-written in a simpler form of

$$p_e + m_p = p'_e + \sqrt{p_p^2 + m_p^2} \quad (3.4)$$

$$\mathbf{p}_e = \mathbf{p}'_e + \mathbf{p}_p.$$

We do not directly observe the recoil proton and so to remove dependence on the proton momentum from equation ?? we use the law of cosines to rewrite the proton

three-momentum in terms of the electron scattered angle θ_e like so

$$|\mathbf{p}'_p|^2 = |\mathbf{p}_e|^2 + |\mathbf{p}'_e|^2 - 2|\mathbf{p}_e||\mathbf{p}'_e|\cos\theta_e. \quad (3.5)$$

With these conservation relations we can restrict all possible electron-proton interactions to the elastic form of eq. (3.1). A special note however, is that in the treatment of a stationary proton target we have not only ignored the small kinetic terms of an atomic hydrogen target inside a cooled liquid, but we have also set aside any internal momenta distribution inside the proton due to its composite quark content. This is also true for higher nuclei, in which case we also have to worry about the momenta of the composite nucleons. While not pertinent to this thesis, one way to deal with this situation is to also detect the recoil proton. Then by applying conservation of energy and momentum, one can determine the “missing” momentum corresponding to the internal structure of the nuclei. However, in the Q_{weak} Experiment the recoil proton is not observed, and so the results sum over any internal structure, as is implied by the dashed circle in fig. 3.1.

The three-momenta and scattering angles, however, are not invariant under a Lorentz transformation. This proves particularly problematic when we want to make direct comparisons between different the various experiments that used different kinematic settings. We need to find an invariant quantity which can be used in any reference frame. If we rewrite the energies and three-momentum components into their corresponding relativistic four-momentum vectors $q^\mu = (E, q_1, q_2, q_3)$, we recall that the square of these four-momentum vectors ($q^\mu q_\mu$) correspond to the invariant mass of the particle m^2 . In fig. 3.1a the virtual photon carries some nominal energy given by $\omega = E_e - E'_e$ and three-momentum given by $\mathbf{q} = \mathbf{p}'_e - \mathbf{p}_e$. Hence, we

define the invariant quantity

$$-Q^2 \equiv q^\mu q_\mu = (E_e - E'_e)^2 - (\mathbf{p}_e - \mathbf{p}'_e)^2, \quad (3.6)$$

as the four-momentum transfer square of the interaction. By using eq. (3.5) and the relativistic limit where $E_e \approx p_e$ and $E'_e \approx p'_e$, we can expand the terms of eq. (3.6) into

$$\begin{aligned} -Q^2 &\approx (E_e - E'_e)^2 - (E_e^2 + E'^2_e - 2E_e E'_e \cos \theta_e) \\ &= -2E_e E'_e (1 - \cos \theta_e). \end{aligned} \quad (3.7)$$

The above equation has three measured quantities, the incident and scattered energies and the scattering angle. It may be favorable to express this in a form that only depends on two of these quantities, so we use the conservation of energy from eq. (3.4) to get

$$E'_e = \frac{m_p E_e}{m_p + E_e (1 - \cos \theta_e)}, \quad (3.8)$$

and apply it to eq. (3.7) to get

$$Q^2 = 2E_e^2 \frac{1 - \cos \theta_e}{1 + (E_e/m_p)(1 - \cos \theta_e)}. \quad (3.9)$$

As I will show next, we can use Q^2 in the determination of cross sections of the electron-proton interaction.

3.2 Electron-Proton Scattering Form Factors

In the derivation of the weak charges in section 2.4.1 we wrote the neutral currents associated with the exchange of a photon (j_μ) and a Z^0 weak boson (j_μ) given by eq. (2.22) and eq. (2.27), respectively. I will use the notation of j_μ^ν to denote the charge currents of an elementary particle due to the gauge boson V . Likewise, the capitalized form of J_μ^ν will represent those of composite particles, such as the proton. We can now write the scattering matrix of the electromagnetic component of the electron-proton interaction as [3, 19]

$$\mathcal{M}_{\text{EM}} = \frac{4\pi\alpha}{Q^2} j_{\gamma e}^\mu J_\mu^{\gamma p}, \quad (3.10)$$

where Q^2 is the four-momentum transfer squared, *alpha* is the fine structure constant, and $j_{\gamma e}^\mu$ and $J_\mu^{\gamma p}$ are the associated photon charge currents of the electron and proton, respectively. The proton charges are more complicated due to the composite nature of the proton, but we can express them in terms of invariant Dirac (F_1) and Pauli (F_2) form factors and takes the form [2, 3]

$$J_p^\mu = \bar{\psi}_p \left[F_1^\gamma(Q^2) \gamma^\mu + F_2^\gamma(Q^2) \frac{i\sigma^{\mu\nu} q_\nu}{2m_p} \right] \psi_p, \quad (3.11)$$

where $\sigma^{\mu\nu}$ is the Minkowski transformation metric and m_p is the mass of the proton. It is experimentally favorable to write these form factors as a linear combinations

known as Sachs form factors[2, 3] of the following form

$$G_E^N(Q^2) \equiv F_1(Q^2) - \tau F_2(Q^2) \quad (3.12)$$

$$G_M^N(Q^2) \equiv F_1(Q^2) + \tau F_2(Q^2) \quad (3.13)$$

which are the electric and magnetic form factors,, respectively, the N indicates that this is true for any nucleon and

$$\tau = \frac{Q^2}{2m_p}. \quad (3.14)$$

Written in this form we can interpret G_E^Y and G_M^Y as the Fourier transform of the electric and magnetic spatial distributions, respectively[20]. Furthermore, at the $Q^2 \rightarrow 0$ limit they become the net electric charge and magnetic moment, respectively.

We can similarly write the weak scattering matrix as

$$\mathcal{M}_{\text{weak}} = \left(\frac{g'}{4 \cos \theta_W} \right)^2 j_{Ze}^\mu J_\mu^{Zp}. \quad (3.15)$$

It is favorable to match the notation of literature in which the scattering matrix is written in terms of the Fermi coupling constant G_F which is given by

$$\frac{G_F}{\sqrt{2}} \equiv \left(\frac{g'}{4 \cos \theta_W} \right)^2, \quad (3.16)$$

so that we get[3]

$$\mathcal{M}_{\text{weak}} = \left(\frac{G_F}{\sqrt{2}} \right) j_{Ze}^\mu J_\mu^{Zp}, \quad (3.17)$$

where we introduce the Fermi coupling constant G_F . Again the weak charge current of the electron is given by eq. (2.27) and the proton current must be parametrized in

terms of the weak form factors as[2, 3]

$$J_\mu^{Zp} = \bar{\psi}_p \left[F_1^Z(Q^2) \gamma^\mu + F_2^Z(Q^2) \frac{i\sigma^{\mu\nu} q_\nu}{2m_p} + \gamma^\mu \gamma^5 G_A^Z \right] \psi_p, \quad (3.18)$$

where the new term G_A^Z is the axial form factor. The Dirac and Pauli form factors are then written using the Sachs form factors of eq. (3.13). We want to express the electromagnetic form factors of the proton in terms of its constituent quarks. However, while the proton is primarily composed of three quarks, two up quarks and one down quark, there can exist a sea of intermediate quarks momentarily appearing in the vacuum. As such, we can build the proton form factors by summing over the possible quark flavors and scale them by their corresponding electroweak charges [2]. Given the electromagnetic charge Q_q of a given quark “ q ” we get

$$G_{E,M}^{\gamma p} = \sum_q Q_q G_{E,M}^q. \quad (3.19)$$

Similarly the weak vector charge g_V is expressed as

$$G_{E,M}^{Zp} = \sum_q g_V^q G_{E,M}^q, \quad (3.20)$$

and the weak axial charge g_A is given by

$$G_A^{Zp} = \sum_q g_A^q G_A^q. \quad (3.21)$$

It is sufficient to include only the light up, down and strange quarks[2]. Summing

over the three light quarks and using the charges of table 2.1 we get

$$G_{E,M}^{\gamma p} = \frac{2}{3}G_{E,M}^u - \frac{1}{3}(G_{E,M}^d + G_{E,M}^s), \quad (3.22)$$

$$G_{E,M}^{Zp} = \left(1 - \frac{8}{3}\sin^2\theta_W\right)G_{E,M}^u - \left(1 - \frac{4}{3}\sin^2\theta_W\right)(G_{E,M}^d + G_{E,M}^s), \quad (3.23)$$

$$G_A^{Zp} = G_A^d - G_A^u - G_A^s. \quad (3.24)$$

We can assume charge symmetry between the up quarks in the proton and the down quarks in the neutron, and similarly the down quark in the proton and the up quark in the neutron[21]. It is then easy to write the neutron form factors as

$$G_{E,M}^{\gamma n} = \frac{2}{3}G_{E,M}^d - \frac{1}{3}(G_{E,M}^u + G_{E,M}^s), \quad (3.25)$$

$$G_{E,M}^{Zn} = \left(1 - \frac{8}{3}\sin^2\theta_W\right)G_{E,M}^d - \left(1 - \frac{4}{3}\sin^2\theta_W\right)(G_{E,M}^u + G_{E,M}^s), \quad (3.26)$$

$$G_A^{Zn} = G_A^d - G_A^u - G_A^s. \quad (3.27)$$

We could take this a step further and rewrite the weak form factors in terms of the electromagnetic form factors of the proton and neutron. These take the form of[2]

$$G_{E,M}^{Zp} = (1 - 4\sin^2\theta_W)G_{E,M}^{\gamma p} - G_{E,M}^{\gamma n} - G_{E,M}^s, \quad (3.28)$$

$$G_{E,M}^{Zn} = (1 - 4\sin^2\theta_W)G_{E,M}^{\gamma n} - G_{E,M}^{\gamma p} - G_{E,M}^s. \quad (3.29)$$

We could even rewrite the form factors of the quarks and express in terms of the proton and neutron form factors, which are easier to determine experimentally. However, I will not re-write them in this dissertation, but they can be found in the literature[2, 3, 21].

3.3 Parity Violating Electron Scattering

Given the scattering matrices of the electromagnetic and the weak interactions of eq. (3.10) and eq. (3.17) we can write the cross section as the amplitude squared of the sum of the scattering matrices

$$\sigma_{ep} \propto |\mathcal{M}_{\text{EM}} + \mathcal{M}_{\text{weak}}|^2 = |\mathcal{M}_{\text{EM}}|^2 + 2 \text{Re}(\mathcal{M}_{\text{EM}} \mathcal{M}_{\text{weak}}) + |\mathcal{M}_{\text{weak}}|^2. \quad (3.30)$$

However, as strength of the electromagnetic interaction is $\propto 1/Q^2$ while the strength of the weak interaction is $\propto 1/(Q^2 - M_Z^2)$, at low $Q^2 \ll M_Z^2$ the electromagnetic term dominates and the amplitude of the weak scattering matrix $|\mathcal{M}_{\text{weak}}|$ banishes. We need a mechanism to access the weak interaction at low Q^2 . Fortunately, we can take advantage of parity violation in the weak interaction to build a system in which the electromagnetic terms are canceled out.

Consider the cross section of a left-handed electron and that of a right-handed electron. Individually each is still dominated by the electromagnetic term, but the difference between the two is

$$\sigma_L - \sigma_R \sim 2 \text{Re}(\mathcal{M}_{\text{EM}} \mathcal{M}_{\text{weak}}). \quad (3.31)$$

We can get a reasonable substitute for a left-handed or right-handed electron by using the helicities. We define the helicity of a particle with mass as the projection of its spin on its momentum vector $h = \mathbf{s} \cdot \mathbf{p}$, where \mathbf{s} is the spin vector and \mathbf{p} the corresponding three-momentum vector. In the limit where the electron mass is smaller than the scattering target ($m_e \ll m_p$) we can treat helicity as being equivalent

to chirality[5] that is defined in the massless limit. So we redefine helicity to be either left-handed (+) or right-handed (-) as such

$$h \equiv \text{sign}(\mathbf{s} \cdot \mathbf{p}) = \begin{cases} + & \text{(left)} & \text{if } \mathbf{s} \cdot \mathbf{p} > 0 \\ - & \text{(right)} & \text{if } \mathbf{s} \cdot \mathbf{p} < 0. \end{cases} \quad (3.32)$$

In this limit the left-handed and right-handed cross sections are equivalent to their spin-momentum defined helicity

$$\sigma_{\text{L}}^{ep} \equiv \sigma_{+}^{ep} \quad \text{and} \quad \sigma_{\text{R}}^{ep} \equiv \sigma_{-}^{ep}. \quad (3.33)$$

We want to avoid having to make absolute cross section measurements so we normalize the difference to the sum of the cross sections to define the parity violating electron-proton asymmetry

$$A_{ep}^{\text{PV}} \equiv \frac{\sigma_{+} - \sigma_{-}}{\sigma_{+} + \sigma_{-}} \sim \frac{2 \text{Re}(\mathcal{M}_{\text{EM}} \mathcal{M}_{\text{weak}})}{|\mathcal{M}_{\text{EM}}|^2 + 2 \text{Re}(\mathcal{M}_{\text{EM}} \mathcal{M}_{\text{weak}})} \sim \frac{2 \mathcal{M}_{\text{EM}}^{*} \mathcal{M}_{\text{weak}}}{|\mathcal{M}_{\text{EM}}|^2}, \quad (3.34)$$

where we used $2 \text{Re}(\mathcal{M}_{\text{EM}} \mathcal{M}_{\text{weak}}) \ll |\mathcal{M}_{\text{EM}}|^2$ to simplify the equation. Consequentially, this also means that the asymmetry is expected to be substantially small where the scale is set by[21]

$$\frac{\mathcal{M}_{\text{weak}}}{\mathcal{M}_{\text{EM}}} \sim \frac{Q^2}{(M_Z)^2}. \quad (3.35)$$

Using $M_{Z^0} = (91.1876 \pm 0.0021) \text{ GeV}/c^2$ [6] from before and the nominal Q_{weak} four-momentum transfer squared $Q^2 \sim 0.025 \text{ GeV}^2/c^2$ the expected asymmetry is on the order of $\sim 10^{-6}$. From now on asymmetries will be denoted in the parts-per notation

of either parts per million ($\text{ppm} \equiv 10^{-6}$) or as will be required later, parts per billion ($\text{ppb} \equiv 10^{-9}$).

We can write the asymmetry in terms of the previously defined Sachs form factors as[21]

$$A_{\text{ep}}^{\text{pv}} = \left(\frac{-G_F Q^2}{4\pi\alpha\sqrt{2}} \right) \left(\frac{\varepsilon G_E^Y G_E^Z + \tau G_M^Y G_M^Z + g_V^e \varepsilon' G_M^Y G_A^e}{\varepsilon (G_E^Y)^2 + \tau (G_M^Y)^2} \right), \quad (3.36)$$

where $\tau(Q^2)$ is defined in eq. (3.14), and ε and ε' are two kinematic variables defined as

$$\varepsilon = \frac{1}{1 + 2(1 + \tau) \tan^2 \left(\frac{\theta}{2} \right)}, \quad (3.37)$$

$$\varepsilon' = \sqrt{\tau(1 + \tau)(1 - \varepsilon^2)}, \quad (3.38)$$

where θ is the polar scattering angle of the electron. We now have a fully robust means of accessing the neutral weak interaction at low energies. What is missing is a way to tie this all in to the measurement of the proton's weak charge, which I will discuss next.

3.4 The Weak Charge of the Proton

Thus far I have alluded to the fact that we can make a determination of the weak charge of the proton using the parity-violating asymmetry defined in eq. (3.36). The inclusion of the vector and axial coupling constants g_V and g_A in the Sach form factors already provides a hint of the role of the weak charges in electron-proton scattering. We also learned that we can write the form factors of a composite proton as the sums of the constituent quark form factors scaled by the charge terms. Then

it follows that we can similarly write the parity-violating Lagrangian for electron-proton scattering as of the quark components. This takes the form of

$$\mathcal{L}_{\text{weak}}^{\text{PV}} = - \left(\frac{G_F}{\sqrt{2}} \right) \left[g_A^e \bar{\psi}_e \gamma^\mu \gamma^5 \psi_e \sum_q g_V^q \bar{\psi}_q \gamma_\mu \psi_q + g_V^e \bar{\psi}_e \gamma^\mu \psi_e \sum_q g_A^q \bar{\psi}_q \gamma_\mu \gamma^5 \psi_q \right]. \quad (3.39)$$

The combinations of axial and vector coupling constants for the electron-quark interaction are commonly defined in the literature as[22]

$$C_{1q} \equiv \frac{1}{2} g_A^e g_V^q, \quad (3.40)$$

$$C_{2q} \equiv \frac{1}{2} g_V^e g_A^q. \quad (3.41)$$

We recall from table 2.1 that $g_V^e = -1 + 4 \sin^2 \theta_W$, and we found in section 2.4.1 that $\sin^2 \theta_W \approx 1/4$, which makes the C_{2q} terms small. We can make a further observation by noticing that as $\theta_e \rightarrow 0$ it makes $\varepsilon \rightarrow 1$. This has the added consequence that $\varepsilon' \rightarrow 0$ which combined with the small g_V^e further suppresses the axial part in eq. (3.36). Under these conditions we claim define the C_{1q} terms as the net-weak charges of the quarks. Furthermore, since we describe the electron-proton interaction as the sum of the constituent quark interactions, we can then determine the net weak charge of the proton by adding up the corresponding C_{1q} charges. In table 3.1 I compute the weak charges of the quarks, proton and the neutron.

First, notice that the weak charge of the neutron is exactly one at tree-level. This is in consequence to having no dependence on $\sin^2 \theta_W$. Conversely, the weak charge of the proton is given by

$$Q_w^p = 1 - 4 \sin^2 \theta_W, \quad (3.42)$$

	Q_{EM}	Q_w (tree level)			
u	$+2/3$	$-2C_{1u}$	$=$	$+1 - (8/3) \sin^2(\theta_w)$	$\approx +0.384$
d	$-1/3$	$-2C_{1d}$	$=$	$-1 + (4/3) \sin^2(\theta_w)$	≈ -0.692
n	0	$-2(C_{1u} + 2C_{1d})$	$=$	$-1 + (0/3) \sin^2(\theta_w)$	$= -1.000$
p	1	$-2(2C_{1u} + C_{1d})$	$=$	$+1 - (12/3) \sin^2(\theta_w)$	$\approx +0.075$

Table 3.1: The net weak charges of the quarks, neutron, and proton, respectively. Calculated in terms of the C_{1u} and C_{1d} coupling constants.

and has an enhanced sensitivity to $\sin^2 \theta_w$. Also since $\sin^2 \theta_w \approx 1/4$ means that Q_w^p is “accidentally” suppressed. This makes the weak charge of the proton more sensitive to deviations caused by any new physics.

3.4.1 Extracting Q_w^p Through the Parity-Violating Asymmetry

Now that we have a definition of the weak charge of the proton, we want to develop a method to extract this value from eq. (3.36). We start by modifying eq. (3.36) in terms of the electromagnetic form factors of eqs. (3.22), (3.25), (3.28) and (3.29), and using the definition of the weak charges in table 3.1, we get[2, 19]

$$A_{ep}^{\text{PV}} = \left(\frac{-G_F Q^2}{4\pi\alpha\sqrt{2}} \right) \left[Q_w^p + \frac{Q_w^n (\varepsilon G_E^{\gamma p} G_E^{\gamma n} + \tau G_M^{\gamma p} G_M^{\gamma n}) - g_V^e \varepsilon' G_M^{\gamma p} G_A^e}{\varepsilon (G_E^{\gamma p})^2 + \tau (G_M^{\gamma p})^2} \right]. \quad (3.43)$$

The first thing we notice is that by writing the asymmetry in this form, we can explicitly see the role of both the weak and neutral charges on the asymmetry. Reuse the forward angle limit of $\theta \rightarrow 0$ to make $\varepsilon \rightarrow 1$ and $\varepsilon' \rightarrow 0$. This makes the axial part vanish and the remaining terms are only dependent on the electric and magnetic form factors of both the neutron and proton. Furthermore when $Q^2 \ll m_p^2$ makes

$\tau \ll 1$ and the remaining terms can be written as[19]

$$A_{ep}^{\text{pv}} = \left(\frac{-G_F Q^2}{4\pi\alpha\sqrt{2}} \right) (Q_w^p + Q^2 B(Q^2, \theta)), \quad (3.44)$$

where $B(Q^2, \theta)$ represents all the “nuclear structure” terms. To isolate the Q_w^p we let

$$A_0 \equiv \frac{-G_F Q^2}{4\pi\alpha\sqrt{2}}, \quad (3.45)$$

and define the reduced parity-violating electron-proton asymmetry as

$$\frac{A_{ep}^{\text{pv}}}{A_0} = Q_w^p + Q^2 B(Q^2, \theta). \quad (3.46)$$

In this simplified form we can treat the Q_w^p term as the intercept of the axis when we let $Q^2 B(Q^2, \theta) \rightarrow 0$.

3.5 Polarization Effects on the Asymmetry

In deriving eq. (3.46) we described an ideal scenario in which the electrons were fully defined as either left- or right-handed. In the remainder of this chapter I will discuss the effects of on the asymmetry given real experimental conditions. I will also describe how we can reduce and correct for these effects in order to extract the parity-violating asymmetry discussed previously.

In eq. (3.34) we observe that the numerator was dominated by the weak mixing term, while the denominator was dominated by the electromagnetic term. The electromagnetic term for an un-polarized proton target is insensitive to the longitu-

dinal polarization of the electron beam. However, the numerator, by construction, is exactly dependent on the longitudinal polarization. This numerator scales with the polarization[23] and is maximal when the electron beam longitudinal polarization is maximal. The asymmetry we measure for a given longitudinally polarized electron beam is

$$A_{\text{msr}}^{\text{PV}} = P_L A_{ep}^{\text{PV}}. \quad (3.47)$$

If we know the longitudinal polarization then determining the real parity-violating asymmetry is straightforward. The determination of the longitudinal polarization of the electron beam is the focus of chapters four and five and represents my major contribution to the experiment.

3.5.1 Transverse Asymmetries

While the electromagnetic term in the denominator of eq. (3.34) is insensitive to longitudinal polarizations, it is still sensitive to transverse polarizations. A transverse polarization is defined as the projection of the electron spin in a direction perpendicular to the direction of motion. The mechanism which gives rise to this dependence is thought to be the interference of the single photon and two photon exchange amplitudes[24]. We write the asymmetry as

$$B_n = \frac{\sigma^\uparrow - \sigma^\downarrow}{\sigma^\uparrow + \sigma^\downarrow}, \quad (3.48)$$

where \uparrow and \downarrow are now normal to the electron beam motion. The use of notation B_n is to highlight that this asymmetry is due to a polarized electron beam, as opposed

to a polarized target A_n . In terms of the scattering matrices, B_n is given as[24]

$$B_n = \frac{\text{Im} \left[\sum_{\text{spins}} \mathcal{M}^{\gamma*} Abs \mathcal{M}^{\gamma\gamma} \right]}{\sum_{\text{spins}} (\mathcal{M}^{\gamma})^2}, \quad (3.49)$$

where $Abs \mathcal{M}^{\gamma\gamma}$ sums over all intermediate states of the two photon exchange. This asymmetry is called a Beam Normal Single Spin Asymmetry (BNSSA) to distinguish it from the parity-violating asymmetry from before, and the asymmetry that arises when both the target and electron are polarized.

Let P_T represent the transverse component to the electron beam polarization. We modify eq. (3.47) to include the transverse polarization as such[24]:

$$A_{\text{msr}} = A_{ep}^{\text{PV}} P_L + B_n \sin(\phi_e - \phi_s) P_T, \quad (3.50)$$

where ϕ_e is the azimuthal angle of the scattering plane and ϕ_s is the azimuthal angle of the spin vector S . Because of the azimuthal dependence, we can remove the contributions of B_n to the parity-violation asymmetry by integrating over 0 rad to 2π rad.

Chapter 4

The Q_{weak} Experimental Apparatus

The experiment was conducted in Experimental Hall C of the Thomas Jefferson National Accelerator Facility (Jefferson Lab) in Newport News, Virginia. Three experimental halls (A, B and C) sit at the end of the Continuous Electron Beam Accelerator Facility (CEBAF) which combines two linear accelerators (linacs) to simultaneously deliver a polarized electron beam to the three halls. Each linac accelerates electrons through ten superconducting Radio Frequency (RF) cryogenically cooled modules (cryomodule) operating at 1497 MHz for all three halls and with an electron bunch boost gradient up to 8.4 MV/m [25]. Bending magnets at the ends of each linac connect them together allowing for multiple passes through each linac. A total of five consecutive passes brings the total maximum beam energy delivered to one hall at 6 GeV. A separator magnet at the end of CEBAF selects out a distinct number of passes to be delivered to each Hall. Figure 4.1 provides a layout and an overview of CEBAF.

The unique requirements of the Q_{weak} experiment meant that the two existing spectrometers in Hall C had to be moved out of the way for a custom built detector to

HOW CEBAF WORKS

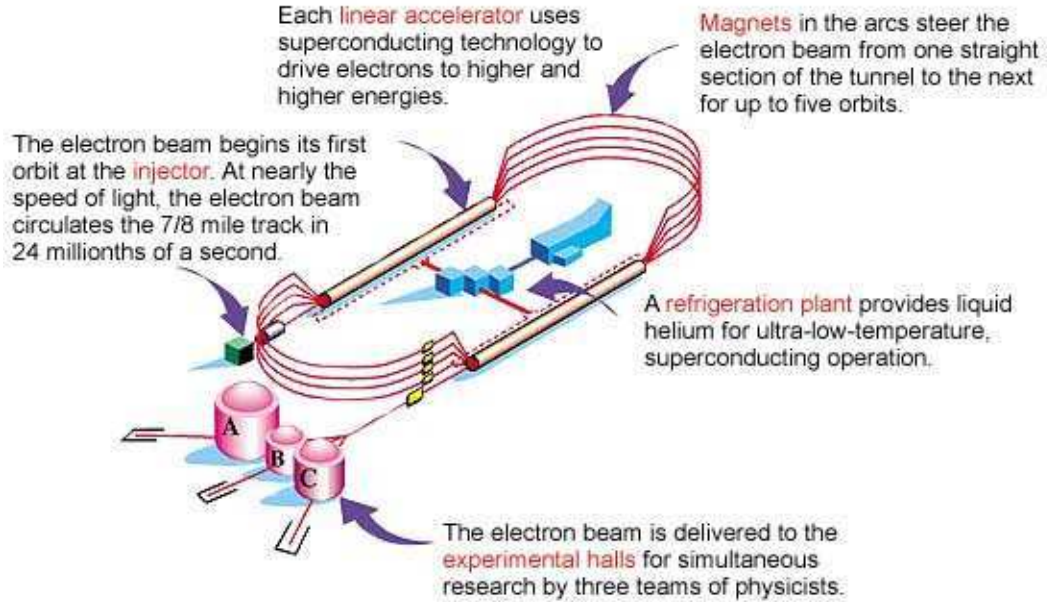


Figure 4.1: A cartoon overview describing the functionality of CEBAF. Graciously provided by JLab's Public Affairs office.

be installed in the hall. The high statistics necessary required high luminosity which we achieved through a combination of a stationary unpolarized proton target and a high current, highly polarized electron beam. Furthermore, in order to minimize any false asymmetries, the detector components were placed radially symmetric along the beam direction in an octagonal configuration as can be seen on figs. 4.2 and 4.5.

Recall the three main measurable quantities in eqs. (3.36) and (3.46): the parity-violating electron-proton asymmetry A_{ep} , the electron beam polarization P and the four momentum transfer Q^2 . We reach A_{ep} through measuring the asymmetry in the integrated signal of the scattered electrons passing through a Cherenkov¹ quartz bar (A_{msr}). The experimental Q^2 can be determined through tracking of individual

¹An alternative spelling is Čerenkov, however, I will be using the Russian spelling throughout.

scattered electrons. Figure 4.2 is a drawing of the components used in these measurements to be discussed further in this chapter. Lastly the measurement of P is achieved through two independent polarimeters as shown in figs. 4.10 and 5.5 and discussed further below.

The remainder of this chapter will provide an overview of the detector setup with sufficient detail to understand the experiment and the analysis, though, the reader is asked to read through the references for a more complete description of each component.

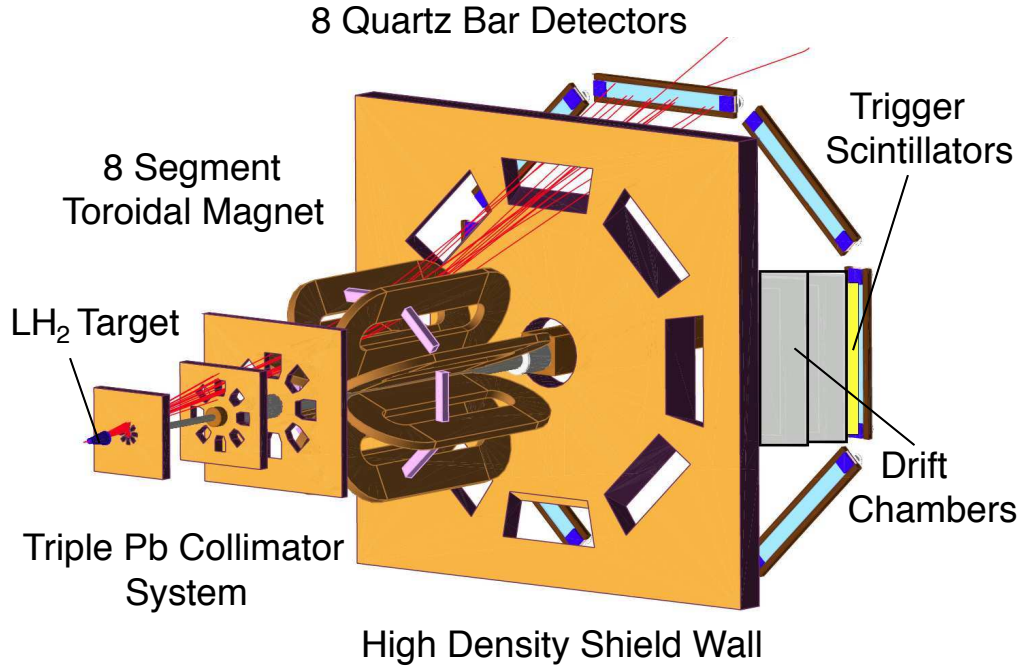


Figure 4.2: An illustration of the main components of the detector[26].

4.1 Polarized Beam Source and High Luminosity

The statistical goals of the experiment are achieved via two critical aspects: a high polarization source with well defined helicity states and a thick proton target.

4.1.1 Producing Polarized Electrons

The polarized electrons come from a crystal of so-called “superlattice” Galium Arsenide (GaAs). GaAs had already shown great promise in producing a theoretical maximum of 50 % polarized electrons as early as 1975[27]. The process of extracting a polarized electron from the crystal involves the use of a technique called optical pumping, in which a photon source (such as a laser) is used to excite an electron from a lower shell in the atom to a higher shell. In the case of GaAs the goal is to excite an electron from the valance band (four-fold degenerate $P_{1/3}$) across the 1.52 eV band gap to the conduction band (two-fold degenerate $S_{1/2}$)[28] as seen on fig. 4.3. Given a circularly polarized photon (σ^\pm), the quantum mechanical selection rules require the transition to abide by $|\Delta m_j| < \pm 1$ which produces the possible excitations on the right of fig. 4.3. Photons with right (left) circularly polarized light produce a 3 to 1 rate from $m_j = -3/2$ ($m_j = +3/2$) in the $P_{3/2}$ valance band to the $m_j = -1/2$ ($m_j = +1/2$) in the $S_{1/2}$ conducting band comparing to the $m_j = -1/2$ ($m_j = +1/2$) to $m_j = -1/2$ ($m_j = +1/2$) from bands $P_{1/3}$ to $S_{1/2}$ respectively. These transitions correspond to 50 % maximum polarization. However, one has to be careful not to use sufficiently energetic photons that can excite from the nearby split-off valance band of two-fold degenerate $P_{1/2}$ which will undo the polarization gain from before[28].

One may overcome the limiting maximum polarization of 50 % by further break-

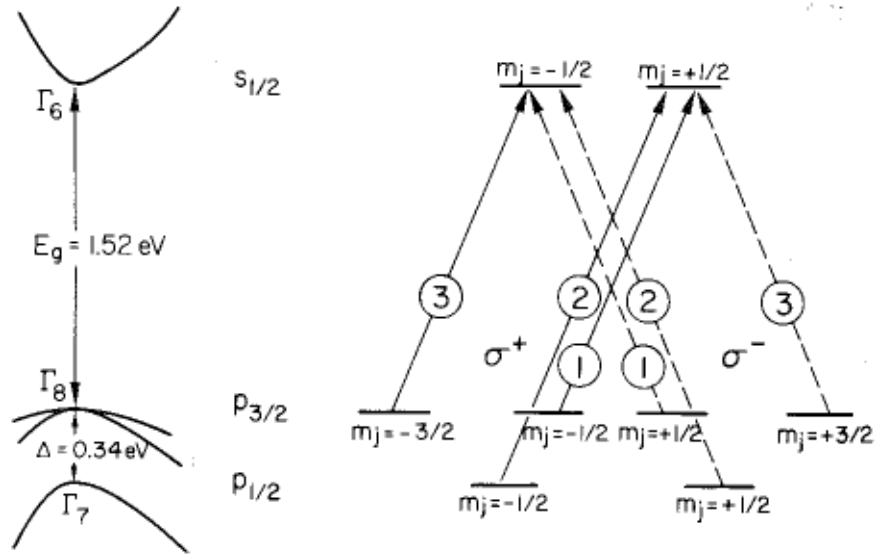


Figure 4.3: Left: A drawing of the electron bands of the GaAs crystal. The highest band is the conduction band and just below is the 1.52 eV band gap. Right: An illustration of possible and relative rates of excitations from the lower non-conducting bands due to an excitation of a circularly polarized photon. The solid lines represent circularly right (σ^+) and the dashed lines circularly left (σ^-) photons. The circles represent the relative rates of excitation with respect to each other. Image taken from [28].

ing the degeneracy of the valance band $P_{1/3}$ [29, 30]. Straining and distorting the band structure can produce such degeneracy[31]. A p-doped GaAs/GaAsP wafer[32] which exhibited maximum polarization was selected and then cut into 15 mm diameter sample photocathodes. In addition to the use of an ultra-vacuum support system, the photocathodes were anodized in the center to define the active area and to prevent re-absorption [33].

4.1.2 Helicity Control and Reversal

One of three gain-switched radio frequency pulsed diode lasers operating at 499 MHz, which is a third of the accelerator's operating frequency, provided linearly polarized photons[33]. The laser beam is then passed through a Pockels cell (an effective quarter-wave plate induced by application of a voltage) that transforms the polarization to circularly polarized[32]. Reversing the voltage on the Pockels cell reverses the helicity of the photons. These circularly polarized photons are then incident on the active region of the GaAs/GaAsP photocathode.

The reversible Pockels cell is shared among all three lasers and defines of the helicity for all three halls[33], which we will define as $H = S \cdot P_{beam}$ where S is the spin of the emitted electron and P_{beam} is the three-momentum of the electron beam. To minimize any sensitivity to relatively slow changes in any element along the beamline, the helicity is continuously reversed throughout the entire experimental data taking. The rate of reversibility was chosen to be 960 reversals per second, but to minimize sensitivities to drifts a quartet pattern was built with either a (+ - - +) or (- + + -) configuration[24].

A slower method of reversing the linearly polarized light prior to entering the Pockels cell employed a using a non-electronic optical element. An insertable half-waveplate (IHP) was moved in and out of the optical path on a scale of 4 to 8 hours which changed the sign of the helicity. A second pseudo-IHP which was made of the same material as the IHP, but did not change the light polarization was also used. The goal was to provide a systematic check on the effect of using the IHP. The pseudo-IHP was deployed starting with the second half of the experiment.

4.1.3 Primary Target

A 34.4 cm long liquid hydrogen (LH₂) target of ~58 L was placed incident to the electron beam to provide the large luminosities required by the experiment. The 180 μ A electron beam deposited 2.1 kW of power on the target, which was then dissipated by a specially designed heat exchanger (HX) which also provided an additional 0.7 kW of reserve cooling for other heat sources[32]. The geometry of the cell containing the LH₂ was designed with the aid of Computational Fluid Dynamics software to reduce the noise contributions due to rapid fluctuations (boiling) in the LH₂ target. Tuning of flow rates and the impact of the helicity flip rate were chosen to further minimize density fluctuations, known as target boiling as shown on fig. 4.4. Further descriptions of minimization of noise in the measurements due to the LH₂ target can be found in [32].

The geometry of the cell was a conical form in the direction of the beam momentum, and the downstream side was designed so that scatterings of electrons less than 14° passed through the downstream exit window. The downstream exit window was 305 mm in diameter and 0.64 mm thick. In comparison the upstream entrance window was 22.2 mm in diameter with a thickness of 0.097 mm. The beam was rastered into an uniform distribution of 4 mm \times 4 mm for two critical reasons, first to prevent damage to either exit window due to the low intrinsic diameter of the beam being ~200 μ m[32]. Secondly, the raster reduces the effects of target boiling.

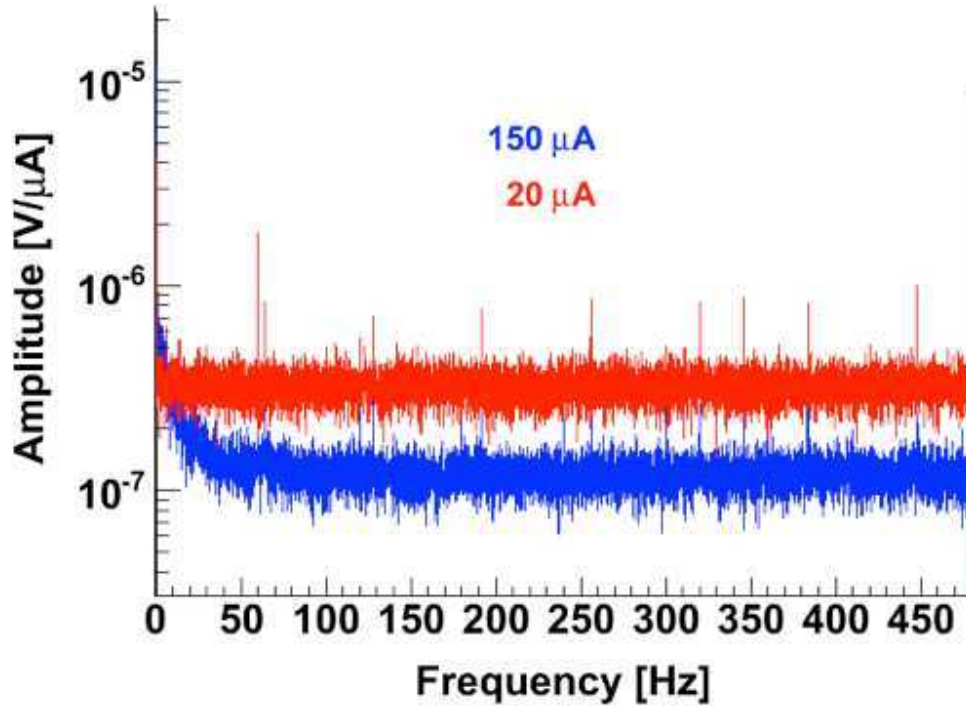


Figure 4.4: Noise on the Main Detectors due to rapid density fluctuations in the LH_2 target[34].

4.2 Main Detectors

Each of the eight Main Detectors (MD) are made up of two 1 m long fused silica synthetic quartz bars (Spectrosil[®] 2000) glued end to end with optical glue. They are 18 cm wide and 1.25 cm thick and were chosen due to their radiation hardness. Additionally, the lack of scintillation means that the bars are not sensitive to neutral particles[35]. At both ends are attached 20 cm long light guides of identical quartz material, also with optical glue. The light guides in turn are optically glued to a 12.7 cm (5") photomultiplier tube (PMT). The light guides serve to move the PMTs out of the elastically scattering region, and further allow them to be protected with lead shielding.

The base of the PMT depends on the running condition. During nominal running conditions of beam current up to 180 μA a base with a gain of $\sim 2 \times 10^3$ is attached. During the special low current period where each particle is tracked independently, a base with gain of $\sim 2 \times 10^6$ is attached[36]. I will refer to these two running conditions as the “integrating mode” and the “event mode” respectively.

The bars are enclosed in an aluminum housing and covered with light tight tape. They are placed radially symmetric around the beam direction on an a Ferris Wheel. A ninth bar was built and placed further from one of the MD bars to be used for background studies (see section 4.6). Refer to fig. 4.5 for relative positions of the MDs around the beamline, as well as simulation of the relative rates. A pre-radiator was placed in front of each of the MDs to increase the overall elastic electron signal, while simultaneously reducing soft/neutral backgrounds. The observed flux of electrons on each individual MD bar was above 850 MHz during nominal running conditions with beam current of 180 μA [32].

4.3 Spectrometer Magnet

The Q_{weak} Torodial Magnet (QTor) is an azimuthally symmetric resistive magnet responsible for bending the elastically scattered electrons and centering them on the MD bars. Fringes in the field are responsible for characteristic mustache shape on the MD bars[36] seen in fig. 4.9. Matching the symmetry of the main detectors, QTor has an eight-fold azimuthal structure composed of eight copper based “race track” packages evenly separated around the beam direction. The integrated field $\int \mathbf{B} \cdot d\mathbf{l}$ is 0.67 T · m along the scattering path, and is nominally zero at the center

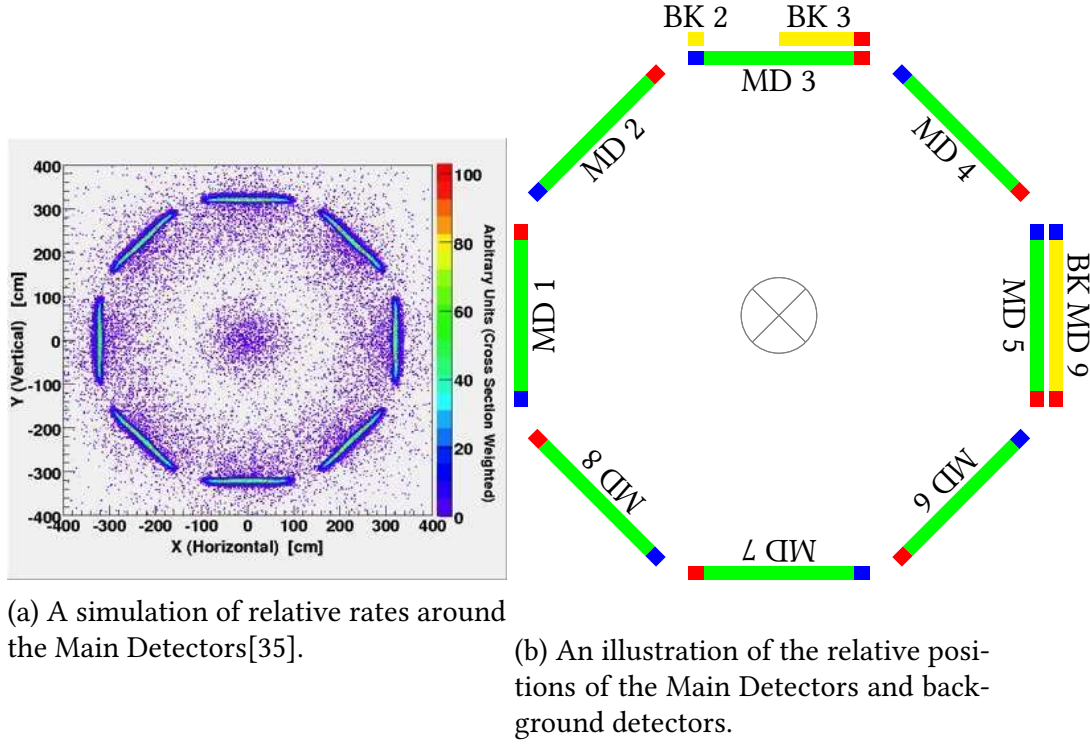


Figure 4.5: Figures showing the relative rates around the Main Detectors (left) and the relative positions of the various detectors (right).

of the magnet. Each package contains a center hole of 2 cm in diameter that houses a water-cooling tube. The magnet is powered by a water cooled DC power supply that converts 420 V of AC to a maximum of 9500 A of DC current with a total power of 1.5 MW[37].

4.4 Collimation and Shielding System

A dedicated shielding and collimation system was deployed to maximize the elastically scattering signal and to minimize other backgrounds.

A set of three collimators of Lead Antimony (95.5 % Pb and 4.5 % Sb) is placed

just upstream of QTor as shown in fig. 4.2. The first and third collimator serve to clean up backgrounds and to reduce the overall rates to the entire detector stack. The second collimator defines the angular acceptance for both the upstream and downstream ends of the target. The overall area of each opening is $\sim 400 \text{ cm}^2$ [2]. The total angular acceptance for all openings was 4 % of π in the scattering angle θ and of this 49 % of 2π in the azimuthal angle ϕ was accepted[24]. In terms of the experimental kinematics this corresponds to an acceptance of $\theta = 5.8^\circ$ to 10.2° and $\theta = 6.6^\circ$ to 11.5° on the upstream and downstream ends of the target respectively[32].

Electrons which scatter at small angles, $\sim 0.75^\circ$ to 4° from the front to the back of the target respectively, can potentially interact with various beamline elements and produce background showers to the detectors. To reduce these signal contributions while still allowing safe passage of the $4 \text{ mm} \times 4 \text{ mm}$ rastered beam, a primary beam collimator was installed within the first collimator at a distance of 47 cm downstream of the target's exit window and allowed a maximum scattering angle of $\theta_{max} = 0.88^\circ$ [32]. This collimator was referred to as the tungsten plug given to its tungsten-copper composition. Simulations performed by the group at Virginia Tech showed that the tungsten plug may see deposited power on the order of 1.3 kW[2] which necessitated a water cooling system for the plug. During normal running the tungsten plug was measured to receive $\sim 1.6 \text{ kW}$ of deposited power[32].

10 cm thick lead collimators (referred to as lintels) were installed within the coils of QTor[2] as seen on fig. 4.6. These were 16 cm long in the radial direction, with 70 cm in length between the coils. The lintels were placed 70 cm upstream of the magnet's center[32]. The last shielding seen in fig. 4.2 is a 80 cm thick wall made of non magnetic, high density barite loaded concrete (Ba_2SO_4) reinforced with stainless

steel rebar.

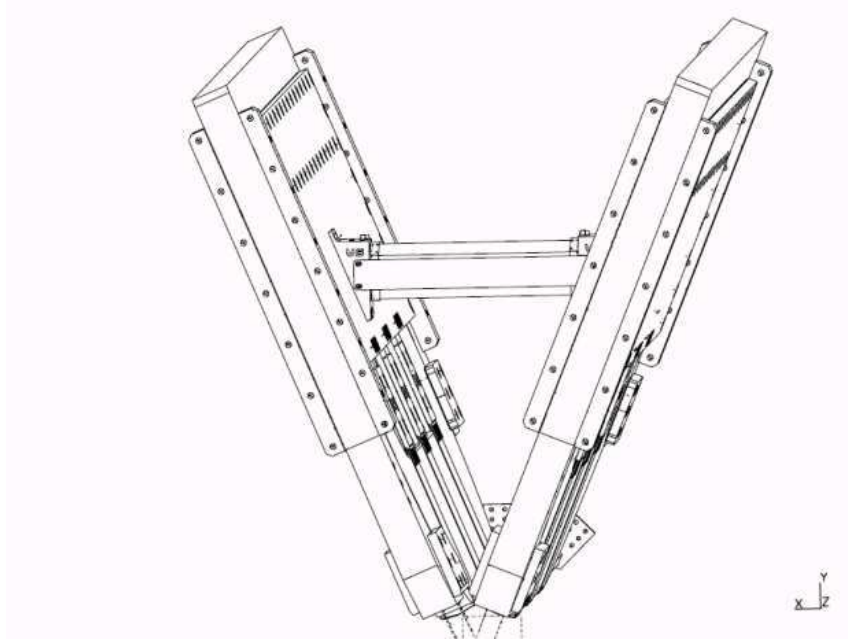


Figure 4.6: Figure showing the lead lintels installed within the coils of the Q_{weak} Toroidal Magnet. CAD drawing provided by the JLab Engineering group.

During commissioning, additional regions of secondary interactions along the beamline were identified which produced large backgrounds on the MDs. To reduce these rates, cylindrical layers of 5.1 cm lead were clamped to the beamline. Upstream of the second collimator this lead shielding was 30.5 cm long and the downstream side was 38.1 cm long.

4.5 Tracking Detectors

Tracking of individual scattered electrons allows one to determine the interaction's corresponding Q^2 . By using the following formulation

$$Q^2 = 2E^2 \frac{(1 - \cos \theta)}{1 + \frac{E}{m}(1 - \cos \theta)} \quad (4.1)$$

we are required to know only the incident beam energy E and the scattered electron angle θ , where m represents the electron mass. Through this formulation we are limited only by the determination of the electron scattering angle which we achieve by the combination of specialized detectors called drift chambers.

The concept of a drift chamber as a detector is based on the generally well known and studied drift and diffusion properties of charged particles through gasses[38]. Essentially a sense wire is held at voltage around parallel grounded conductor planes all immersed in a gas mixture. A passing charged particle will then leave a trail of ionized gas along its path, where the ionized gas will then drift towards the sense wire. The drift time will determine the distance from the wire to the particle's path view a well determined conversion of drift time to distance[39]. By overlapping layers of sense wire planes in alternating directions one can reconstruct both the incident angle and position of a passing charge particle.

Two drift chamber configurations were used in unison for the experiment, the aptly named Horizontal Drift Chamber (HDC) and the Vertical Drift Chamber (VDC) whose traditional names stem from the direction of the ion drift. In terms of performance, an HDC configuration has higher angular resolution at a loss of spacial resolution, while a VDC has a higher spatial resolution at a loss of angular, as will

be explained in the following sections.

4.5.1 Horizontal Drift Chambers

The HDC configuration contains three planes (x, u, v) of 32 sense wires each strung in alternating directions. The first plane is the x plane whose wires are strung in the radial direction, while the other two planes (u and v) are strung in $\pm 53^\circ$ respectively. Each sense wire is spaced 1.1684 mm apart from the nearest sense wire and placed in the center of that gap is a field wire to help maintain the field perpendicular to the plane. The electric field is made perpendicular by two aluminized mylar plates placed on either side and parallel to the wire plane. Each field wire is held at 2150 V while the mylar plates and the sense wires are grounded[39].

Each HDC is composed of a pair of three wire planes (x, u, v) and (x', u', v') with a total of seven mylar plates separating the planes. There are a total of four HDCs employed in the experiment arranged in packages or groups, where one package is placed radially around the beamline and the second opposite the first. Each HDC in a package is separated by ~ 40 cm[2] in the beam direction. The HDC setup is rotatable by hand in order to be able to measure the scattered electrons in any of the eight octants.

During the first running period a mixture of 50 % argon and 50 % ethane that was bubbled through isopropyl to prevent back flow of atmospheric mixtures into the chambers[2]. The ethane included in the mixture absorbed X-rays produced in the chambers. During the second running period the mixture was changed to 65 % Argon and 35 % ethane[39] for an overall better performance.

The total active area of each HDC is $50 \text{ cm} \times 70 \text{ cm}$ and requires a flux of elec-

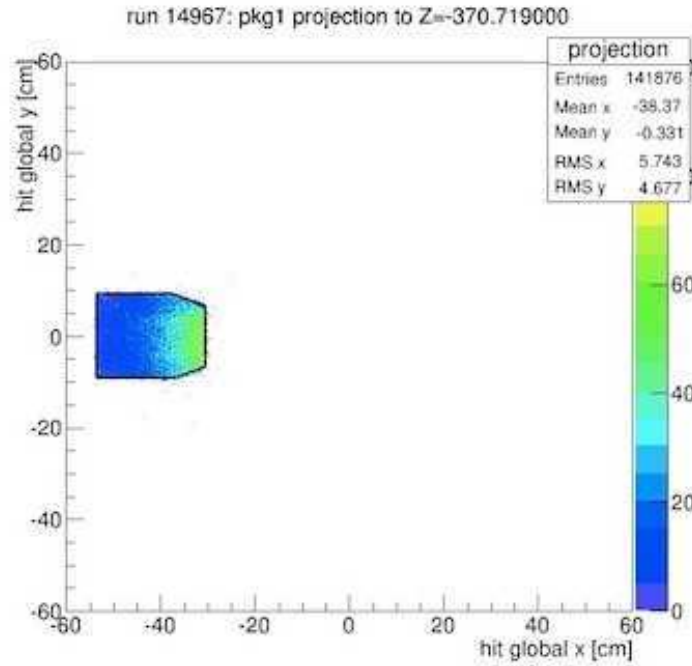


Figure 4.7: A profile of tracks projected back to the defining collimator near the HDCs. The few projections seen outside of the enclosed region are likely improperly reconstructed tracks due to multiple scattering of the particles before detection. Image provided by David Armstrong.

trons of less than 1 MHz to operate efficiently. During the planning stages of the experiment, it was estimated that the flux of electrons through the HDCs would be of the order of 2.6 MHz/nA. This meant that the tracking system could not run at the nominal beam current of 180 μ A that the experiment required. As such, special running periods were set up where the beam current was reduced to the pA range.

The expected angular resolution is ~ 0.6 mrad while the spacial resolution is expected to be ~ 200 μ m. Figure 4.7 shows the reconstruction of tracks to the defining collimator and the HDCs. The black outline represents the defining collimator and the tracks placed outside the collimator's opening are likely improperly reconstructed due to multiple scattering of the particle prior to detection.

4.5.2 Vertical Drift Chambers

The VDC configuration contains only two wire planes (u, v) arranged $\pm 26.5^\circ$ with respect to the wire frame as seen on fig. 4.8. Each plane is composed of 279 wires spaced ~ 0.5 in apart (12.62 mm) and each chamber is composed of four planes of wires (u, v) and (u', v') . Similar to the HDCs, a package composed of two VDCs placed 53 cm apart in the beam direction were placed ~ 1.8 m from the beamline. The corresponding package was placed on the opposite quadrant. The center of both packages was ~ 107 cm upstream of the MDs. A mechanical system would rotate the VDCs around the beamline so that they could cover any number of the MDs. While rotations were limited, the range of 0° to 180° allowed for a redundancy at octants 3 and 7. A hydraulic system would then move the VDCs inward and behind the shield wall during high current running.

To achieve better spacial resolution than an HDC configuration, a VDC configuration relies on particles incoming with nominal trajectory of 45° with respect to the wire planes. This corresponds to a tilt of 24.4° with respect to the beamline.

Unlike the HDC case, each individual wire is held at ground and instead the $12.7 \mu\text{m}$ thick mylar foils surrounding each plane are held at 3800 V[37]. The mixture use in the gas was the similar 50 % Argon and 50 % and bubbled through an isopropyl alcohol[37]. At 279 wires per plane, the entire VDC system had a total of 4464 wires that needed to be read out for each triggered event. The cost associated with this was large, so a compromise was made by using multi-plexed electronics that combined the signal of every eight wires together. This reduced the total readout requirements by a factor of 9[37].

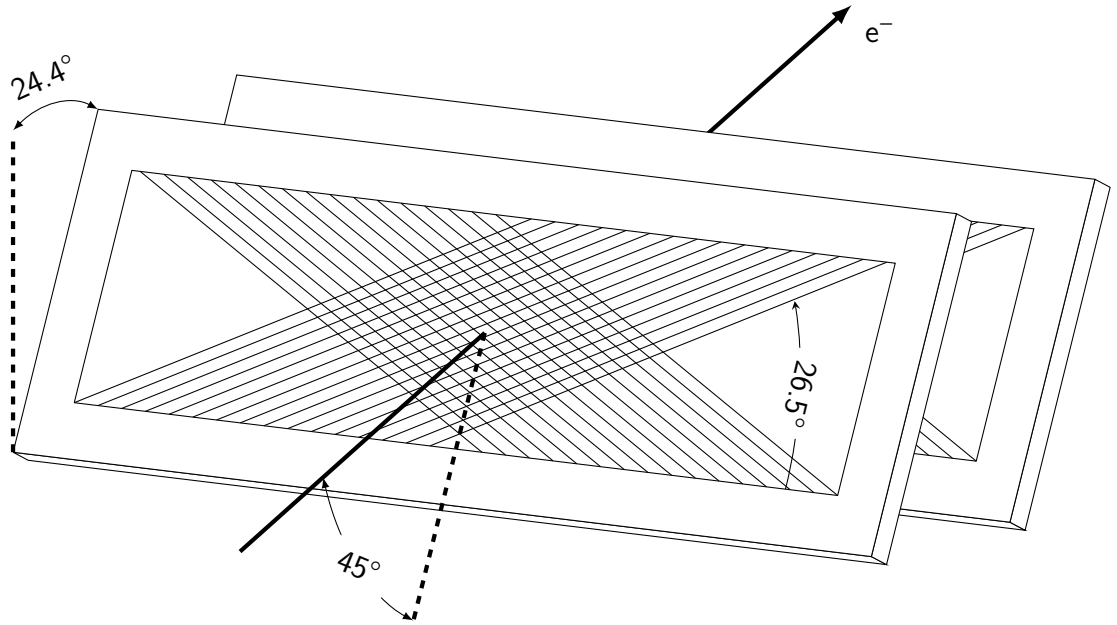


Figure 4.8: A drawing of the Q_{weak} Vertical Drift Chambers as seen from Octant 3. The particle's nominal trajectory intersects the VDCs at a 45° angle with respect to the VDCs plane. The sense wires are strung perpendicular to each other and 26.5° with respect to the edge of the frame.

4.5.3 Triggering Scintillator

During normal measurements of Q^2 in the pA range, tracks were triggered by a scintillator mounted on both VDC packages and sandwiched by a VDC on either side. Other triggering mechanisms were used for various other diagnostics, such as MD triggered as well as individual VDC and HDC triggered and will not be discussed here further.

The two plastic BC-408 scintillators, sensitive to both charged particles and X-rays alike, were manufactured by Saint Gobain. The long attenuation length of 210 cm was not deemed problematic given the 218.45 cm length of each scintillator. Additionally each had a width of 30.48 cm and thickness of 1 cm. Due to the sen-

sitivity to virtually any particle a Channel Constant Fraction Discriminator (CFD) was used to reduce the noise and achieved a better triggering time[2].

4.5.4 Focal Plane Scanner

Mapping of the relative flux over the entire area of a MD bar was highly desirable. A focal plane scanner was designed and positioned in octant 7, with a flexibility of being placed either upstream or downstream the corresponding MD bar. The focal plane scanner used two overlapping crystal cubes of the same Cherenkov material as the MDs. The $1\text{ cm} \times 1\text{ cm} \times 1\text{ cm}$ cubes are overlapped together and produce an effective area of 1 cm^2 that can handle a maximum electron flux of 1 MHz/cm^2 making them able to handle the more than 0.472 MHz/cm^2 each MD bar sees at high current. After the commissioning period and for the remainder of the run the scanner was positioned upstream of the MD bar which gave it greater range of mobility. However, this new position also made its use disruptive to normal data taking, and was only used sparingly throughout the experiment.

Two stepper motors controlled motion in the x and y axis independently, which allows one to map the relative flux anywhere in the face of the MD bar. One such map is show in fig. 4.9 where we can see the distinct and expected “moustache” shape predicted by simulation.

4.6 Background Detectors

A number of dedicated components were also placed on or near the various Q_{weak} detectors to monitor backgrounds coming from non elastic electron-proton pro-

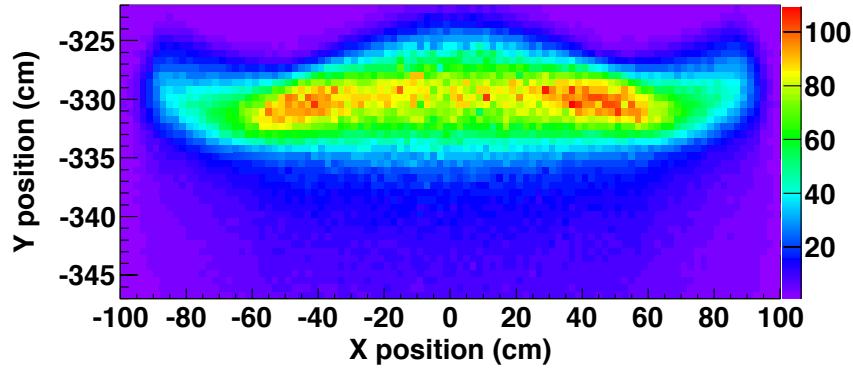


Figure 4.9: Relative rate map of the flux over the MD bar as seen by the focal plane scanner in octant 7 (see fig. 4.5b) [32]. The vertical y-axis is in the radial direction and the x-axis is tangent to the radial direction and perpendicular to the beam direction. The characteristic “mustache” shape seen in the rates on the MD bar in octant 7 as mapped out by the scanner apparatus.

cesses. To ensure a proper comparison, the materials used were all similar to the materials used to build the Main Detectors.

The first two background detectors were composed of a single PMT attached to an integrating mode style base (of gain $\sim 2 \times 10^3$). Each PMT was placed in a separate light tight box along with a reference LED light source and all enclosed in double layers of mu-metal[32]. One was placed in a well shielded location and fixed throughout the experimental running. The purpose of this detector was to provide an electronic noise baseline for the Main Detector electronics chain. In particular it was designed to measure any leakage of the helicity reversal signal onto the Main Detector electronics[32]. Over the course of eight hours the detector produced a low-noise signal of ~ 8 ppb reference.

The second detector was placed in the super elastic region near Main Detector 3 (see fig. 4.5b) to monitor the effects of particles incident on the Main Detectors

PMTs. A third PMT was assembled similar to the first two, but attached to it was a quartz light guide configured exactly as on the Main Detectors. This background detector was again placed in the super elastic region next to a different PMT. The purpose was to monitor and understand the effects of particles incident on the light guides of the Main Detectors.

The last background detector was an exact replica of the Main Detectors, which we conveniently named Main Detector 9, and placed in the super elastic region of Main Detector 5. It was used to provide information on the background contributions to the Main Detectors signal. The backgrounds included general radiation noise inside the experimental Hall, as well as energetic scatterings off the surrounding support structure. As it was positioned in the super elastic region, it also provided a measurement of some of the neutral particles scattered from the target but unaffected by the magnetic field.

4.7 Beam Monitors

Along the beamline were special components that monitored the beam characteristics and included a special five step modulation system that measured the effects of varying characteristics of the beam on the MD measurements.

4.7.1 Polarimeters

Two polarimeters were used to measure the electron beam longitudinal polarization via measurements of asymmetries of known QED scattering processes. The first polarimeter used was the standard Hall C Møller polarimeter which, as the name

suggests, relies on Møller scattering. Polarization measurements using the Møller polarimeter benefit greatly from many years of use in Hall C that made this polarimeter become such a well understood absolute measurement device. However, it is not without its limitations and requires that the electron beam be run with substantially lower current than needed by the Q_{weak} experiment, and measurements are invasive to the main experiment. These limitations necessitated the development of a second polarimeter which instead is based on Compton scattering.

The remainder of this section will briefly discuss the details of the Møller polarimeter. The Compton polarimeter discussion will be deferred to the next chapter as it constitutes the majority of this dissertation.

Møller Polarimeter

The Møller polarimeter has been a standard Hall C system for at least 15 years prior the Q_{weak} experiment and is the sole polarimeter to provide polarization for the commissioning period (also known as “Run 0”) results published in late 2013[40].

Similar to the Compton polarimeter, the Møller polarimeter relies on the fact that a polarized electron scattering off a polarized target will have a non-zero asymmetry for two longitudinally different helicity states. The asymmetry relates the measured asymmetry A_{msr} with the theoretical asymmetry for 100 % polarized beam and target (called the analyzing power) A_{th} and the polarizations of both the electron beam (P_e) and the target (P_{tgt}) as[41]

$$A_{msr} = A_{th}(\theta)P_eP_{tgt}. \quad (4.2)$$

The target is a thin foil of pure Fe and a 3.5 T solenoid drives the foil into magnetic

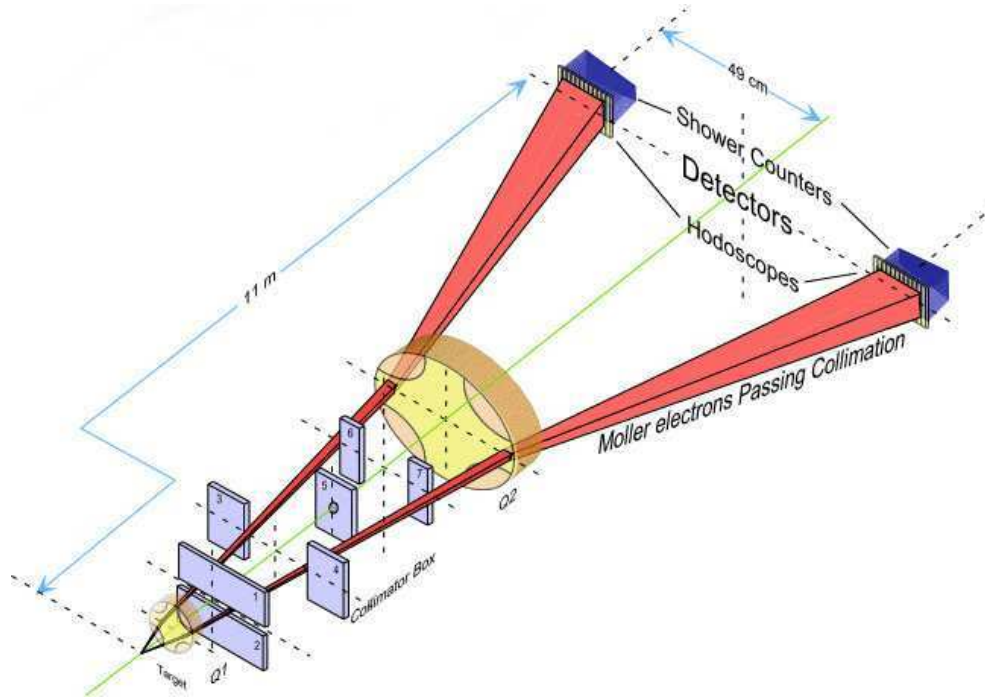


Figure 4.10: Drawing of the Møller Polarimeter layout showing the main components of the polarimeter. Møller scattered electrons from the target would be selected by a quadrupole-collimator-quadrupole configuration. The resulting Møller scattered electron pairs were detected in coincidence by the detectors on either side of the beamline. Figure courtesy of Howard Fenker.

saturation. The effective target electron polarization is $\sim 8\%$. As seen on fig. 4.10 the scattered recoil electrons pass through a quadrupole magnet that separates the two electrons and directs them to two lead-glass calorimeters where they are detected simultaneously. A collimator on each calorimeter defines the acceptance, and one collimator is slightly smaller such that it primarily defines the coincidence acceptance.

After the asymmetry has been measured, special care must be taken in determining the analyzing power through simulation so that one may properly account for scattering from the inner shell electrons in the Fe target which are unpolarized.

Additionally, a short in the quadrupole magnet used during Run I required careful studies of the resulting magnetic field before being able to determine the beam polarization.

While the fifteen year history of the Møller polarimeter deemed it a reliable measurement of polarization, the presence of a solid Fe foil in the path of the electron beam meant it was a invasive measurement to the main experiment. Additionally, the polarization induced on the Fe foil quickly deteriorated with increased beam current, limiting the maximum current of the polarimeter at $\sim 5 \mu\text{A}$. This lead to the development of the Compton polarimeter, to be discussed in the following chapter.

4.7.2 Current Monitors

The beam current - overall charge through the target - was monitored by two components: a parametric dc current transformer and several resonant cavities. The parametric current transformer, commonly referred to as an Unser in reference to [42], is the only component capable of being calibrated to an absolute standard independent of any other component [43] and is non-invasive to the beam. The gain is well known ($40 \text{ mV}/\mu\text{A}$) and has an excellent linearity which allows it to span a wide dynamic range[44]. However it suffers from poor signal to noise² and is susceptible to small offset and drifts over time. The Unser signal is sent to a Voltage-to-Frequency converter (V/F) through a level translator that matches the Unser output to the full 10 V range of the V/F. The output of the V/F, now at $400 \text{ Hz}/\mu\text{A}$ are, then sent to a Data Acquisition system (DAQ).

To supplement the Unser monitor, several resonant cavities, referred to as the

²The gain was raised by an order of magnitude from $4 \text{ mV}/\mu\text{A}$ to $40 \text{ mV}/\mu\text{A}$ in an attempt to overcome this limitation. However, a higher gain means higher DC drifts.

Beam Current Monitors (BCMs), were deployed throughout the beamline. Three such BCMs were located near the entrance to Hall C (BCM1, BCM2 and BCM17) while an additional two were being developed for later part of the experiment. However, for purposes of the analysis in the following chapters, BCM1, BCM2 and BCM17 were the only ones monitored and recorded.

The BCMs operating frequency was calibrated to the natural accelerator frequency of 1497 MHz, such that the individual hall's beam frequency of 499 MHz will couple to the cavities 1497 MHz TM₀₁₀ node.[43]. As long as the beam is relatively centered on the cavity, BCMs are independent of absolute beam position[2]. However, BCMs have no absolute reference standards since the signal depends not only on the beam current but also on the surface finish of the cavities. As such, the absolute calibration must be determined by simulation, or as is used in the experiment, by calibration against a limited range of the Unser (see section 6.1.1 for a detailed discussion of the calibration). Additionally, a limitation exists that for imprecise tunings then the output power will depend on the temperature of the cavity[43]. To minimize this effect, the temperature of the BCMs was stabilized during the experimental running period.

4.7.3 Position Monitors

Several switched electrode electronics beam position monitors (SEE BPM) were used throughout the accelerator beamline to monitor the beam position, and adjust the trajectory if needed. A four-wire stripline antenna system was placed inside the beamline and laid out symmetrically around the center. The four wires were isolated by a SEE setup and the accelerator's 1497 MHz frequency was down converted to

45 MHz signals that can be read out by commercial data acquisition systems[45] as seen on fig. 4.11.

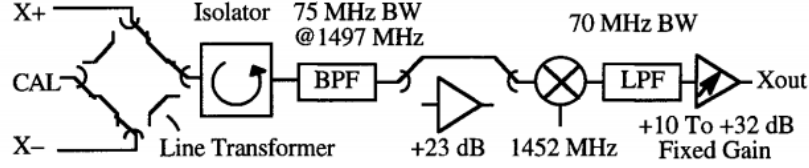


Figure 4.11: A schematic of the SEE BPM system employed at CEBAF showing the relative position of the four-wire stripline antenna. The antenna's are isolated by a SEE setup and 1497 MHz signal is down converted to 45 MHz to be read out by commercial data acquisition systems. Taken from [45]

The relative signal differences between opposing antennas (X^+ , X^-) and (Y^+ , Y^-) allows one to determine the beam position within the beamline to within $100\ \mu\text{m}$ in a range of $\pm 5\ \text{mm}$ [45]. The coordinate x, y relative to the BPM coordinate system by

$$x_i^{bpm} = k f_i \left(\frac{X_i^+ - \alpha_i X_i^-}{X_i^+ + \alpha_i X_i^-} \right), \quad (4.3)$$

where k is the BPM's conversion constant, which varies by the size of the BPM but is nominally $18.88\ \text{mm}/\text{adc channel}$, f_i is the gain of the BPM, α_i is the relative gain of the antenna and lastly X_i^\pm is the antenna signal. The BPMs are rotated to 45° with respect to the vertical axis to minimize the antenna's exposure to synchrotron radiation. This was true for all BPMs except for two placed in the Compton chicane where the dispersive region was vertical, and whose detailed calibrations can be found in section 6.1.2. To determine the position relative to the accelerator and hall coordinate system we then rotate the coordinates by the BPM angle ϕ with respect

to the vertical axis

$$\begin{pmatrix} x \\ y \end{pmatrix} = \begin{bmatrix} \cos \phi & -\sin \phi \\ \sin \phi & \cos \phi \end{bmatrix} \begin{pmatrix} x^{bpm} \\ y^{bpm} \end{pmatrix}. \quad (4.4)$$

4.7.4 Luminosity Monitors

Luminosity monitors (Lumis) were placed around the beamline at two locations; one set at the upstream face of the primary collimator, and another 17 m downstream of the target. The four upstream Lumis were designed to monitor the (mostly) Møller rate scattering from the target at 5°[39]. They are 2 cm thick rectangles of similar quartz as the MDs and have an active area of 27 cm × 7 cm with the shortest side positioned radially with respect to the beamline. Two 35 cm long PMTs were attached to either side of a 2 cm notch cut out at both sides of the upstream Lumis.

On the downstream side there are eight smaller Lumis positioned radially around the beamline to monitor scattering particles of 0.5° from the target. At this range they are to be more sensitive to helicity correlated beam properties than their upstream counter parts and the MDs[39]. Each downstream Lumi is 4 cm long and 1.3 cm in depth. One side of the rectangle is tapered, giving it a sort of trapezoidal shape with the longest side having width of 3 cm and the shorter down to 1.7 cm. A 35 cm air-cone light guide folded from a single highly reflective aluminum sheet attached to each Lumi and a PMT[39].

4.7.5 Beam Modulation System

Since another requirement for the measurement of a precise asymmetry were relatively stable beam properties, and the beam properties were known to exhibit small natural changes, we also required a controlled method of studying the effects of these changes. Four pairs of air-core conductive copper coils were installed just upstream of the Hall's entrance. These coils modulated the beam in a controlled manner, with two pairs of coils controlling the beam in the x -direction, and the other two pairs controlling the beam in the y -direction[46]. Independently they were to modulate the beam such that four beam properties beam position (x, y) and their corresponding slopes (x', y') were modulated independent of each other. The fifth modulation was in the beam energy E_{beam} which was driven by modulating one of the cryomodules in the south linac. All five modulations were driven by a sinusoidal signal that ran for roughly one second every minute, with a complete cycle of modulations requiring five minutes.

The extracted responses could then be used to determine the contribution to the measured asymmetry as[46]

$$A_{false} = \frac{1}{\langle Y \rangle} \left(\sum_{i=1}^5 \frac{\partial Y}{\partial X_i} \Delta X_i \right), \quad (4.5)$$

where Y represents the detector integrated signal (yield), X_i and X_i corresponds to the beam property being modulated and its deviation from its mean respectively. Lastly the $\frac{\partial Y}{\partial X_i}$ term represents the sensitivity on the detector signal to a given beam property.

4.8 Auxiliary Targets

Additional targets were attached to the bottom of the LH₂ support structure and a remotely controlled 2-axis motion system could position them in the beam path. These auxiliary solid targets provided a variety of checks for the detector system as well as playing a crucial role in understanding some of the background rates and processes to the main experiment. A total of 24 targets were grouped into three arrays from top to bottom (see fig. 4.12) and each attached to an aluminum frame that was kept in close thermal contact to the LH₂ cooling system.

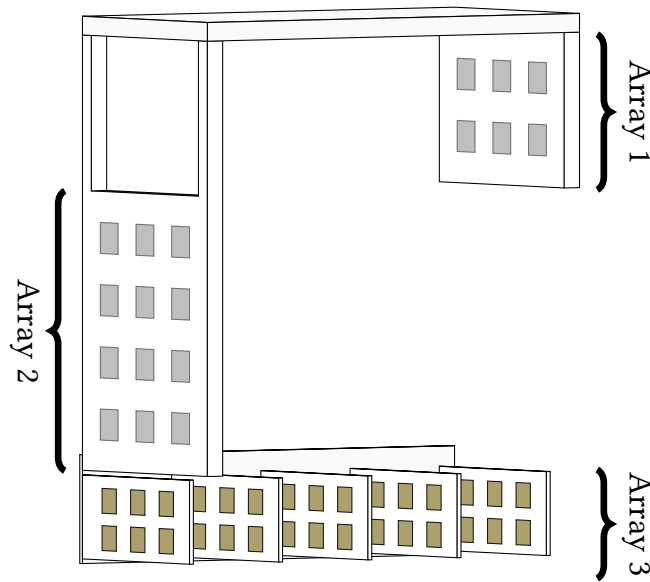


Figure 4.12: An illustration showing the relative positions of the solid auxiliary targets. In the real setup not all available positions were used, particularly in the case when they would overlap one of the targets downstream.

The top two arrays were composed of similar $2.5\text{ cm} \times 2.5\text{ cm}$ targets positioned in z at either the downstream exit window z -position (Array 1) or the upstream entrance window z -position (Array 2). The first array was divided into two rows and

three columns while the second array was divided into four rows and three columns. Among the targets at these two arrays were varying thicknesses of pure Al foils which, at these exact z -positions, provided direct studies of the overall contribution to the Main Detector signals due to the Al windows of the LH₂ target. The varying thicknesses of those targets were used to understand the necessary radiation corrections.

A few aluminum targets were included in these arrays which had holes of varying size cut out of the foil. These targets allowed us to precisely calibrate and position all targets with respect to the beam path[32]. Using information from these targets also allowed us to determine the exact position as well as offset angles of the entire ladder system.

Finally, the third array contained targets arranged into five different z -positions spanning the length of the LH₂ target. The purpose of this spread was to understand and calibrate the tracking detectors discussed in section 4.5 and collectively these targets were known as “optics targets”. Figure 4.12 shows only the relative position of possible targets, though many of these positions correspond to open holes as to accommodate targets further downstream. Some targets were purposely asymmetric (such as an asymmetric wedge) to properly map the coordinate system of the tracking detectors during track reconstruction.

Chapter 5

Compton Scattering and Polarimetry

The Q_{weak} experiment required not only a highly polarized electron beam, but also imposed tight constraints on the determination of the beam polarization to an absolute precision of at least 1 % [47]. To accompany the already present Møller polarimeter, a new polarimeter based on the principles of Compton scattering was designed and commissioned for the Q_{weak} experiment. In this chapter, I will introduce the concept of polarization measurements with a Compton polarimeter, as well as the specific setup that was used during the Q_{weak} data-taking periods.

5.1 Polarimetry Through Compton Scattering

Compton scattering can be used to determine the polarization of the electron beam when both the electron and photon in the interaction are polarized. This technique can be dated back as early as the late 1960's to early 1970's [48–50]. To summarize

the technique, we first consider the special case where both the electron and photon in the interaction have well-defined helicities. Then define the cross section of an electron with well-defined helicity h interacting with a photon with well-defined helicity h' as $\sigma(e_h\gamma_{h'})$. When we work out the mathematics we find that the cross section of a left-handed electron $\sigma(e_L\gamma_{h'})$ is not equal to the cross section of a right-handed electron $\sigma(e_R\gamma_{h'})$ when the initial helicity of the photon (h') is the same in both interactions. Therefore, when we build a “left-right” asymmetry of the following form

$$A_{\gamma_{h'}}^{\text{LR}} \equiv \frac{\sigma(e_L\gamma_{h'}) - \sigma(e_R\gamma_{h'})}{\sigma(e_L\gamma_{h'}) + \sigma(e_R\gamma_{h'})}, \quad (5.1)$$

we find that it must be nonzero. I will later show how this asymmetry is directly affected by the polarizations of both the electron and photon, and will work out a technique by which we can work backwards to determine the electron polarization. First, however, I will start with a description of the kinematic equations of Compton scattering.

5.1.1 Kinematics of Compton Scattering

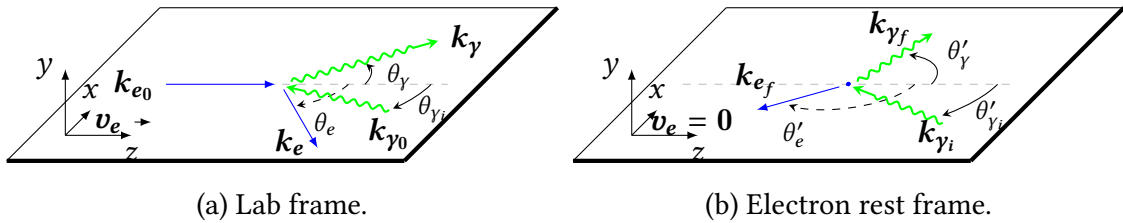


Figure 5.1: Compton scattering on the x - z plane as show in the lab frame and the electron rest frame. The electron rest frame is the conventional Compton scattering frame, which we then boost into the laboratory frame at the end.

The interaction of two particles can be described in a two dimensional plane as

seen on fig. 5.1a where the interaction has been drawn in the Q_{weak} lab frame in the x - z plane. A single electron from the beam moves downstream in the $+z$ direction with momentum \mathbf{k}_{e_0} and velocity \mathbf{v}_e . A photon moves opposite with momentum \mathbf{k}_{γ_0} in the $-z$ direction with a small polar angle θ_{γ_i} with respect to the $+z$ axis. After Compton scattering the electron and photon have momentum \mathbf{k}_e and \mathbf{k}_γ in the scattering plane, respectively. In order to derive the kinematic equations, it is easier to boost the system into the conventional Compton frame where the electron is at rest as seen in fig. 5.1b. In this frame the photon moves in the $-z$ direction with momentum \mathbf{k}_{γ_i} , the scattered electron and photon have momentum \mathbf{k}_{e_f} and \mathbf{k}_{γ_f} , respectively, and the transformation can be described with the following Lorentz transformations:

$$k_{\gamma_0}^\mu \rightarrow k_{\gamma_i}^\mu = \Lambda_\nu^\mu k_{\gamma_0}^\nu, \quad (5.2)$$

$$k_\gamma^\mu \rightarrow k_{\gamma_f}^\mu = \Lambda_\nu^\mu k_\gamma^\nu, \quad (5.3)$$

$$k_{e_0}^\mu \rightarrow k_{e_i}^\mu = \Lambda_\nu^\mu k_{e_0}^\nu, \quad (5.4)$$

$$k_e^\mu \rightarrow k_{e_f}^\mu = \Lambda_\nu^\mu k_e^\nu. \quad (5.5)$$

Before continuing, we must define a few more variables, namely, the θ_e and θ_γ which are the in-plane scattering angles of the electron and photon in the lab frame with respect to the $+z$ axis. Likewise, in the electron rest frame, we have the in-plane scattering angles θ'_e and θ'_γ for the electron and photon in the rest frame respectively. For future reference we can also define the electron and photon out-of-plane scattering angles (ϕ_e, ϕ_γ) and (ϕ'_e, ϕ'_γ) for the lab frame and rest frame respectively.

We can now write down the scattered photon momentum in the electron rest

frame as

$$k_{Yf} = \frac{m_e k_{Yi}}{m_e + k_{Yi} (1 - \cos \theta'_Y)}, \quad (5.6)$$

where m_e is the electron mass in units of MeV/c^2 . In this form we can already see that the maximum scattered photon energy k_{Yf} is occurs at $\theta'_Y \rightarrow 0$. Finally we can use the Lorentz transformation relations from eq. (5.5) to derive the equation in the lab frame as

$$k_Y = \frac{4ak_{Y0}E^2}{m_e^2 + a\theta_Y^2 E^2}, \quad (5.7)$$

where we now use the electron beam energy E and include a unitless parameter a defined as

$$a \equiv \frac{1}{1 + \frac{4k_{Y0}E}{m_e^2}}. \quad (5.8)$$

Here we again note that when $\theta_Y^2 \rightarrow 0$ we get the maximum scattered photon energy in the lab frame written as

$$k_Y^{max} = \frac{4ak_{Y0}E^2}{m_e^2}. \quad (5.9)$$

See fig. 5.3a for a graph of the Q_{weak} beam energies vs the scattered photon in-plane angle, which shows that the majority of the photons scatter at small angles (back scattered with respect to their initial direction). Lastly, we can define ρ as the fractional energy of the scattered photon energy to the maximum possible scattered energy, which corresponds to

$$\rho \equiv \frac{k_Y}{k_Y^{max}} = \frac{m_e^2}{m_e^2 + a\theta_Y^2 E^2}, \text{ where } \rho \in (0, 1]. \quad (5.10)$$

5.1.2 Compton Cross Section

The contributing processes to Compton Scattering can be visualized with Feynman diagrams as seen on fig. 5.2 which contain two primary tree level channels, the s -channel and u -channel when expressed using Mandelstam variables. We can start

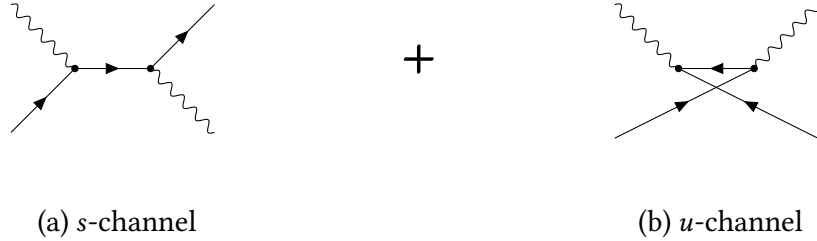


Figure 5.2: The main contributing processes of Compton scattering expressed via Mandelstam variable channels s and u respectively.

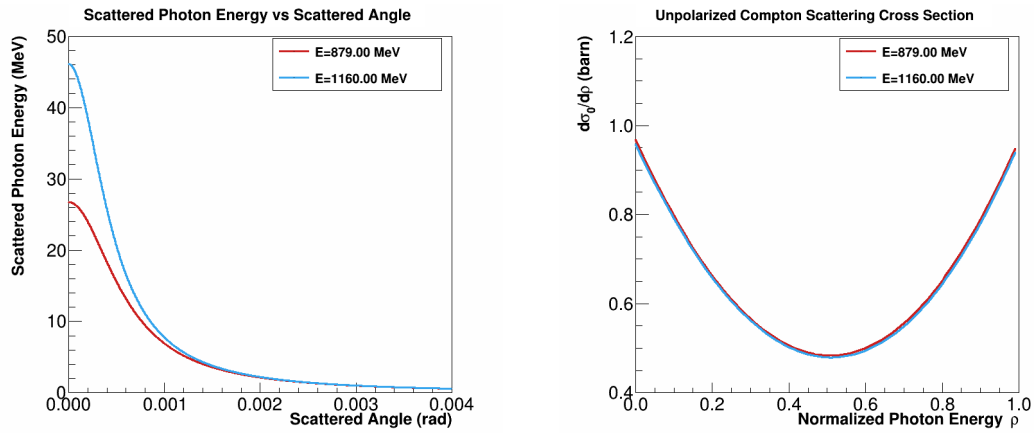
from the prescription outlined in Peskin and Schroeder[51] to write the scattering matrix for fig. 5.2 as

$$i\mathcal{M} = -ie^2 \varepsilon_\mu^*(k') \varepsilon_\nu(k) \bar{u}(p') \left[\frac{\gamma^\mu \not{k} \gamma^\nu + 2\gamma^\mu p^\nu}{2p \cdot k} + \frac{-\gamma^\nu \not{k}' \gamma^\mu + 2\gamma^\nu p^\mu}{2p \cdot k'} \right] u(p), \quad (5.11)$$

where k (p) is the initial photon (electron) momentum and k' (p') the scattering momentum, respectively. The square of this matrix is proportional to the differential cross section $d\sigma/d\Omega$. By summing over all polarized states and integrating by the azimuthal angle ϕ , we can derive the Klein-Nishina cross section for un-polarized Compton scattering, which we can then parametrize in terms of eqs. (5.8) and (5.10) to reach[50]

$$\left(\frac{d\sigma}{d\rho} \right)_{unpol} \equiv \frac{d\sigma_0}{d\rho} = 2\pi r_0^2 a \left[\frac{\rho^2(1-a)^2}{1-\rho(1-a)} + 1 + \left(\frac{1-\rho(1+a)}{1-\rho(1-a)} \right)^2 \right]. \quad (5.12)$$

We can already use these equations to understand the characteristics of Compton scattering in the laboratory. Figure 5.3b shows the relationship between the the un-polarized component of the cross section with respect to photon scattering energy. However, in order to extract the electron polarization, we will need to evaluate individually the polarized terms of eq. (5.11) for states of either right and left handed electrons and expand the sum of the polarized states of photons $(\sum \varepsilon_\mu^*(k')\varepsilon_\nu(k))$.



(a) The scattered photon energy as a function of the photon's scattering angle. This also shows the expected result that the low scattering angles carry the most energized scattered photons.

(b) The un-polarized component of the cross section ($d\sigma_0/d\rho$) as a function of the normalized scattered photon energy. In terms of the normalized energy (ρ) there is little difference between the two Q_{weak} kinematics.

Figure 5.3: Graphs showing the properties of the photon scattered energies and cross sections under the Q_{weak} kinematics and a special running period during the Q_{weak} running. The two energies correspond to the nominal Q_{weak} energy of 1160 MeV and the special running period at 879 MeV.

The polarized cross section can be written in terms where the electron is purely longitudinally polarized and similarly the case where the electron is purely trans-

versely polarized. The longitudinal component is written as[50]

$$\left(\frac{d\sigma}{d\rho}\right)_{long} \equiv \frac{d\sigma_1}{d\rho} = \mp 2\pi r_0^2 a P_e P_\gamma \left[(1 - \rho(1 + a)) \left(1 - \frac{1}{1 - \rho(1 - a)} \right)^2 \right], \quad (5.13)$$

where P_e and P_γ represent the electron and photon polarization, respectively. Similarly the transverse component is[50]

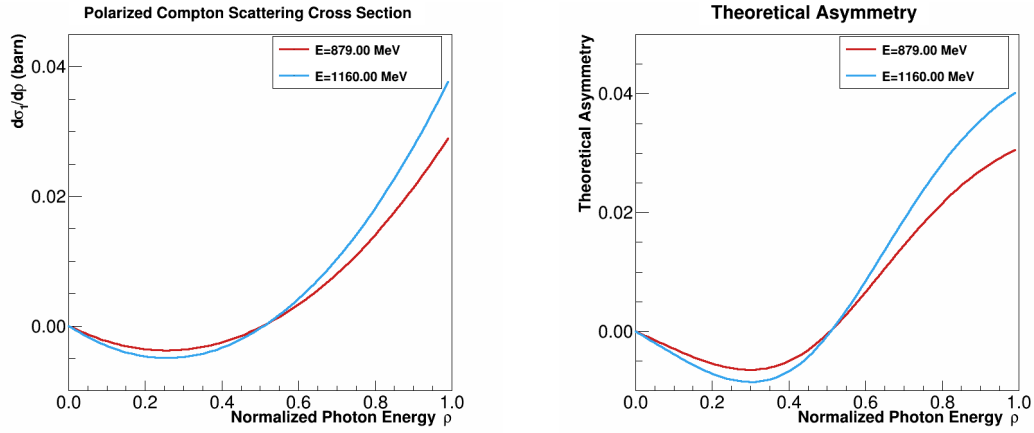
$$\left(\frac{d\sigma}{d\rho}\right)_{trans} \equiv \frac{d\sigma_2}{d\rho} = \mp 2\pi r_0^2 a P_e P_\gamma \cos \phi \left[\rho(1 - a) - \frac{\sqrt{4\rho a(1 - \rho)}}{1 - \rho(1 - a)} \right], \quad (5.14)$$

where ϕ is the azimuthal scattering angle. In the laboratory the electron spin may contain both longitudinal and transverse components given by the angle ψ with respect to the $+z$ axis. Combining eqs. (5.12) to (5.14) we get the total differential cross section[50]

$$\frac{d\sigma}{d\rho} = 2\pi r_0^2 a \left[\left(\frac{d\sigma_0}{d\rho} \right) \mp P_e P_\gamma \cos \psi \left(\frac{d\sigma_1}{d\rho} \right) \mp P_e P_\gamma \sin \psi \cos \phi \left(\frac{d\sigma_2}{d\rho} \right) \right]. \quad (5.15)$$

As will become important in later sections, we note that the transverse dependent parts of eq. (5.15) drop out when integrating over the azimuthal angle ϕ . An important feature of eq. (5.15) is that the total cross section is directly dependent on the handedness of the electron as is evident in fig. 5.4a. We can use the same definition of helicity from section 4.1.2 to build an experimentally measurable asymmetry for the longitudinal component of the two electron states in the differential cross section as

$$A_m(\rho) \equiv \frac{(\frac{d\sigma}{d\rho})^+ - (\frac{d\sigma}{d\rho})^-}{(\frac{d\sigma}{d\rho})^+ + (\frac{d\sigma}{d\rho})^-} = \mp P_e P_\gamma \cos \psi \left[\frac{d\sigma_1/d\rho}{d\sigma_0/d\rho} \right], \quad (5.16)$$



(a) The longitudinally polarized component of the cross section ($d\sigma_1/d\rho$) as a function of normalized photon energy ρ .

(b) The theoretical asymmetry of the differential cross sections from eq. (5.17).

Figure 5.4: Plots of both the longitudinally polarized component of the Compton scattering cross section and the respective asymmetry. Note that the sign of the asymmetry is dependent on the definition of the handedness of the electron and the polarization direction of the photon. The transverse component has been excluded as it goes to zero under an integral over the azimuthal angle ϕ .

where we can define A_ϵ as

$$A_\epsilon(\rho) \equiv \frac{d\sigma_1/d\rho}{d\sigma_0/d\rho} = \frac{(1 - \rho(1 + a))^2 - 1}{\rho^2(1 - a)^2(1 - (1 + a))} - \frac{(1 - \rho(1 - a))^2 + 1}{\rho(1 - a)(1 - (1 + a))}. \quad (5.17)$$

From eq. (5.16) we can see that when system is completely longitudinally polarized ($\psi \rightarrow 0$) the total polarization of the system can be extracted from the ratio of A_m/A_ϵ . Similarly, when the system is completely transversely polarized ($\psi \rightarrow \pi/2$) the asymmetry should measure zero. Finally, we can summarize the asymmetry as

$$A_m(\rho) = A_\epsilon(\rho)P_eP_\gamma \cos \psi = \begin{cases} A_\epsilon(\rho)P_eP_\gamma & \text{for } \psi \rightarrow 0 \\ 0 & \text{for } \psi \rightarrow \pi/2. \end{cases} \quad (5.18)$$

Though the goal is to reach a beam purely longitudinally polarized, the more likely scenario is that a small component of transverse polarization is present. As far as the analysis of the electron detector is concerned (section 5.2.2), the formulations of eq. (5.18) are sufficient to determine the electron's longitudinal polarization. However in a case of the photon detector, which sees only the sum over a range of energies, as will be shown in section 5.2.3, then we can expect the asymmetry to be scaled linearly by energy[50] as $A_m(\rho) \rightarrow \rho A_m \epsilon(\rho)$, where $\epsilon(\rho)$ accounts for any non-linear effects of the detector. The total measured asymmetry is then an integral of all the asymmetries of the range $[\rho_{min}, \rho_{max}]$, which we can then normalize by the integral of cross sections to get a measured asymmetry of the form[23]

$$\langle A_{th} \rangle = \frac{\int_{\rho_{min}}^{\rho_{max}} d\rho A_\epsilon(\rho) \epsilon(\rho) (d\sigma_0/d\rho) \rho}{\int_{\rho_{min}}^{\rho_{max}} d\rho \epsilon(\rho) (d\sigma_0/d\rho) \rho}. \quad (5.19)$$

5.2 The Hall C Compton Polarimeter

The Hall C Compton Polarimeter is positioned 11 m upstream of the LH₂ target and is composed of two independent detectors. Each of the detectors is capable of independently determining the beam polarization by detecting either the Compton scattered electron or photon, respectively. The electron beam trajectory is diverted 57 cm towards the floor by two dipole magnets so that its path intersect a laser beam (the interaction point) (see fig. 5.5) produced by a laser system developed at the University of Virginia. The laser beam serves as the photon target in Compton scattering and the point where the two beams intersect is referred to as the interaction point. Further downstream, two additional dipole magnets return the beams to its nominal

trajectory towards the LH_2 target. This temporary deviation of the beam allows us to position the photon detector directly downstream of the interaction point, while the third dipole in the system directs the Compton scattered electrons towards the electron detector. The four identical dipoles are wired in series and are aligned so as to minimize any disruptions to the portion of the beam which did not interact with the laser. By borrowing the term “chicane” from road design, where it is used to describe an artificial and temporary deviation of the road path, we refer to this four dipole configuration as a chicane.

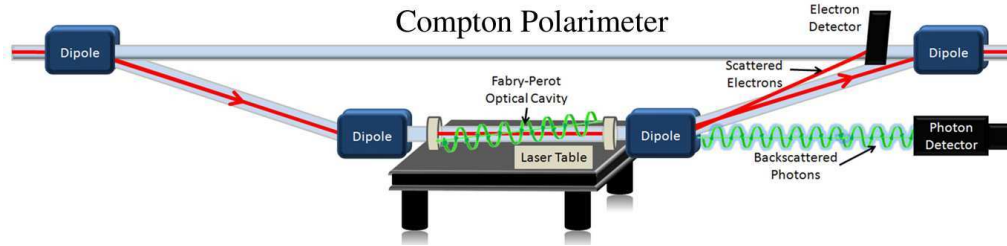


Figure 5.5: Drawing of the Compton Polarimeter. We see the four dipole chicane diverting the beam towards the laser table. The third dipole selects the Compton scattered electrons and allows the photons to pass through to the photon detector. The fourth dipole then diverts the remainder of the beam towards the LH_2 target. Thanks to Donal Jones for providing this picture.

Each dipole is made out of two water cooled copper coils of 220 m in total wire length and wrapped around 64 times in the $+z$ direction and placed on either side of the electron beam pipe. The physical length of each dipole is 121.46 cm so that the electron path length through the magnetic field is 124.6 cm at the Q_{weak} electron beam energy and magnetic field of 0.54 T. The four dipoles were designed by MIT, built by Buckley Systems, and shipped to Jefferson Lab for final installation.

The Compton scattered electron energy determined by the electron detector is directly related to the magnetic field of the third dipole as I will explain on sec-

tion 5.2.2. Because of this a special effort was made to fully understand the characteristics of the produced magnetic field before installation. A current scan from 0 A to 150 A revealed that at currents below 50 A and above 150 A the magnetic field quickly became non-linear. However, at the two Q_{weak} electron beam energies, the magnetic currents were consistently more linear as seen by the two vertical lines of fig. 5.6 where the non-linear effects were much smaller than 0.5 %.

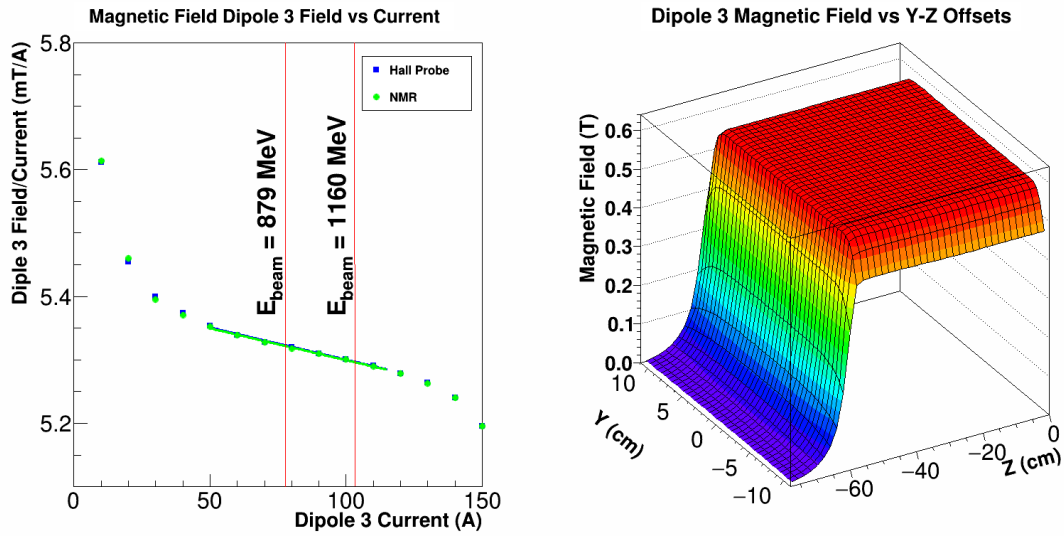


Figure 5.6: A map of the magnetic field normalized to the supplied current and plotted versus the current shows a well behaved linear relationship within the nominal settings for the two beam energies used in Q_{weak} . The right figure shows a map of magnetic field of one half of the dipole and shows the relationship to the beam direction z and the vertical axis y . We can see the relatively uniform behavior under minimal deviations from the central regions.

5.2.1 Laser System

The laser target was provided by a Coherent Verdi 10 diode-pumped solid-state laser which outputs 10.5 W of linearly polarized light at a fixed wavelength of 532 nm[32].

The linearly polarized light with $\sim 0.2\%$ vertical polarization was fully horizontally polarized by a high extinction ratio (100,000:1) Glan-Laser Calcite Polarizer GL10-A from Thorlabs. The GL10-A is a polarizing beam splitter (PBS) that transmits the horizontally polarized light while reflecting the vertically polarized light at 90° . While the high extinction ratio ensures virtually no transmission of vertically polarized light, a small fraction of horizontally polarized light is reflected at 90° along with the vertically polarized light. At this point the fully horizontally polarized light is converted to $\sim 99.99\%$ circular polarization through the use of a quarter wave plate (QWP) positioned further downstream of the optical path. A half wave plate (HWP), which flips the sign of the circular polarization, is positioned after the QWP and allows for complete control over the resulting photon helicity[52].

The resulting circularly polarized light was coupled through the back of a highly reflective dielectric mirror and into a low gain Fabry-Pérot optical cavity 85 cm in length. A Fabry-Pérot (FP) cavity is built with two mirrors on either side where the position and curvature radius of the mirrors are selected so that there is a buildup of standing waves inside the cavity[53]. Specifically the condition is defined by the length of the cavity (L) given as a half-integer multiple of the wavelength of the laser (λ), or simply written as $n\lambda = 2L$ [52]. To maximize the gain, the cavity must be “locked” to a specific frequency mode of the laser. Early tests at the University of Virginia proved the feasibility of reaching a cavity with a gain of 200. The resulting laser system was placed on an optical table and the cavity built inside the beam pipe with the mirrors positioned so that this amplified laser beam would intersect the polarized electron beam at 1.3° . Measurements of the transmitted power through the cavity determined the net power inside the cavity, which reached ~ 1700 W[54].

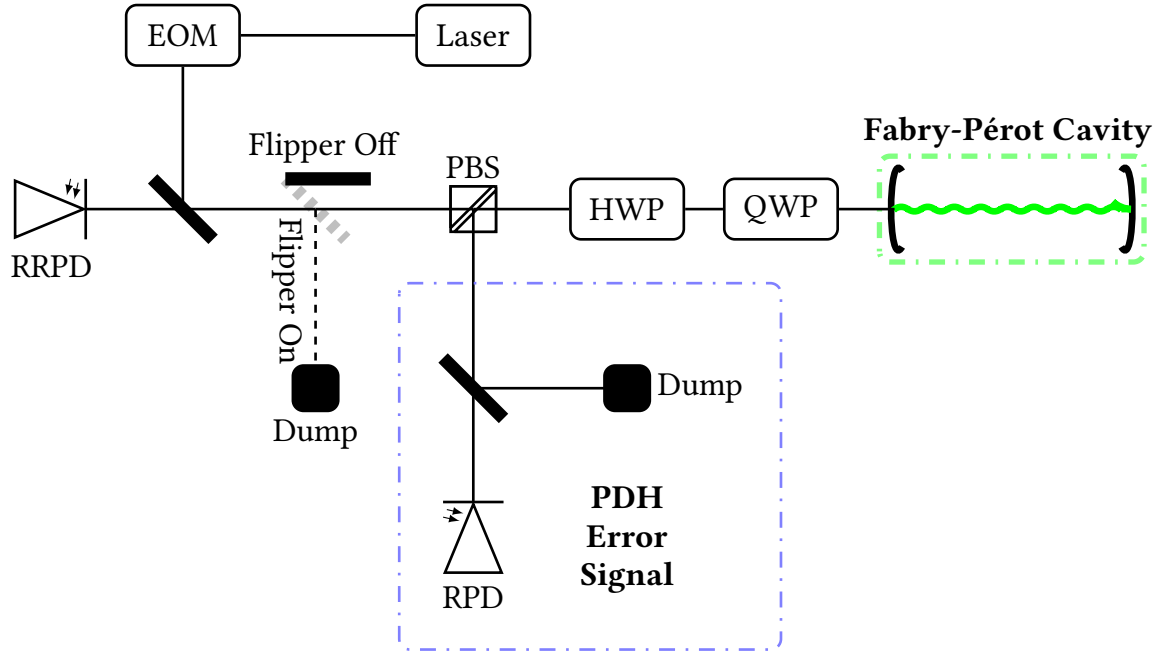


Figure 5.7: A simplified layout of the optical path of the Compton laser. Additional components not described by this thesis were not drawn.

The term “locking” in this case means that the Verdi output frequency was directly controlled by a fast feedback system. In this case, the lock was performed to the external Fabry-Pérot cavity using an interferometer technique known as the Pound-Drever-Hall technique (PDH) first described by Pound in 1946[55] and expanded by Drever and Hall in 1983 [56]. The PDH uses a rapidly modulated signal being mixed with the laser signal to produce phase-modulated sidebands that are well outside the FP passbands. The modulation was provided by an upstream Electro-Optic Modulator (EOM) set to modulate at 6 MHz[52]. The resulting sidebands are then reflected from the first FP mirror and are in anti-phase with the output of the EOM. Following the optical path back to the PBS part of these linearly polarized

anti-phased components are reflected 90° and mixed with the incoming laser light into a photo-diode (RPD). The components of these two signals cancel out and the resulting signal functions as an error signal. The locking electronics were provided by a DigiLock 110, which is a commercial laser locking apparatus from Toptica. The DigiLock electronics would then mix the PDH error signal with a signal from the laser modulated light and send to one of two inputs on the Verdi laser. One input responded to rapid changes in the signal, where the other one would correspond to a longer integrated signal. Within the Verdi laser, a Piezo-Electric mirror mount (PZT) would be physically modulated the internal cavity of the laser to produce the desired output frequency. The results of the locked state vs the unlocked states can be seen from the transmitted and reflected power in fig. 5.8a. An example of a clean error signal from the PDH technique can be seen on fig. 5.8b.

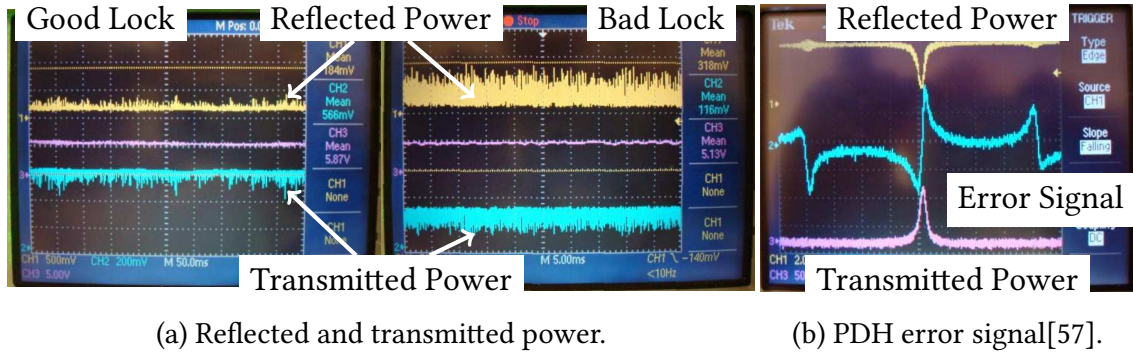


Figure 5.8: The Pound-Drever-Hall technique uses an error signal of a reflected signal from a band outside the Fabry-Pérot passband to lock the cavity to a laser. A clean scope trace of the error signal is seen in fig. 5.8b. The effectiveness of the locking technique is evident in the scope traces of the transmitted and reflected power from the cavity is seen on fig. 5.8a. The left trace shows good locking with low reflection and stable transmission, while the right shows a bad lock where the reflected power is large and noisy and the transmitted power decreases and has broad noise.

While the optical path of the laser to the FP mirror, under good conditions, al-

ready guaranteed near 100 % circular polarization, we still needed a technique to measure the health and overall output polarization of the laser. Initially, dedicated measurements were made, during the off period of the accelerator, to measure the degree of circular polarization (DOCP) inside the cavity. During these periods, a strong relationship was observed between the DOCP inside the cavity and the measured residual reflective power (RRPD) of light reflecting off the first FP mirror[58, 59]. This power was measured by a photo-diode, the RRPD, placed behind a partially reflective mirror along the optical path back to the laser, which when placed in the position shown in fig. 5.7 should correspond to the degree of linearly polarized light (DOLP). In particular, the dedicated measurements showed that DOCP was inversely proportional to DOLP for all configurations of the quarter-wave plate and half-wave plate (see fig. 5.9) and as expected the DOLP was proportional to the measured RRPD. This relationship was further solidified by discovery of a paper which outlined a technique for remote control of polarization[60]. The researchers proved mathematically that the reflected light from the first FP mirror is circularly polarized if and only if the incident light on the PBS is linear orthogonal to residual reflected light[60]. Taking advantage of this fact, the minimization of the RRPD throughout the second running period of Q_{weak} ensured maximal DOCP inside the cavity. The result is that the laser polarization for this period was 100 % with a net error of -0.2% [52].

As I will describe later, the desire to periodically make direct background measurements necessitated that the power stored in the laser cavity be removed. For this reason a mirror positioned along the optical path (see fig. 5.7) was periodically positioned (flipped in) to intersect the optical path of the beam and reflect the beam

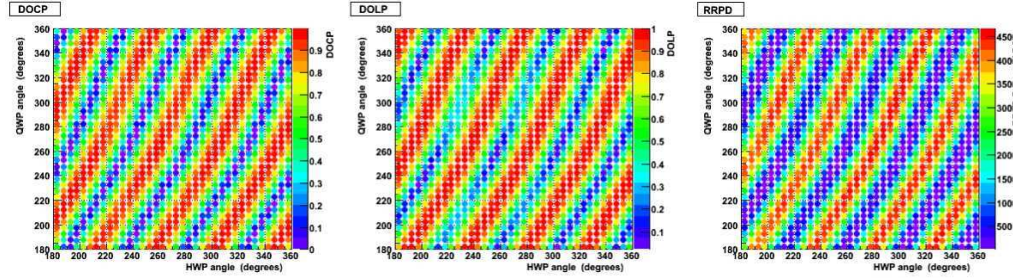


Figure 5.9: A figure showing the relationship of laser polarization to the setting on the quarter-wave plate and the half-wave plate, taken from [61]. By comparing both plots we see the inverse relationship between the degree of circular polarization to linear polarization. The third figure shows the corresponding residual reflected power measured.

away from the cavity. This provided the simplest way to guarantee total removal of the photon target incident on the beam without the need to turn off the laser. However, due to suspected heating effects on optical components of the laser, which lead to poor stability of the cavity locks, it was decided in March, 2012 to stop using the flipper mirror, and instead simply unlock the cavity. While the gain of 200 was not achieved without a lock, the low laser light inside the cavity could still accidentally lock for brief periods, so to mitigate this risk the laser was scanned over its frequency range. The residual light inside the cavity was observed to contribute only a minimal effect, as seen when monitoring background rates[62].

5.2.2 Electron Detector

The electrons that interact with the laser propagate downstream with the remaining electrons in the beam and are bent upwards by the third dipole. The dipole bends the scattered electron slightly more than the remaining un-scattered electron beam given their slight differences in energies. Shortly before the fourth dipole, an

electron detector is placed at ~ 6 mm above the nominal beam trajectory in order to intercept and detect the scattered electrons. The remaining un-affected beam is bent by the fourth dipole and proceeds on its way towards the LH_2 target. The full details of the electron detector are discussed in Amrendra Narayan's thesis[63], but will be summarized here.

The electron detector is composed of four planes of diamond plate detectors 0.5 mm thick placed ~ 1 cm apart[63]. There are 96 horizontal electrode strips composed of layered Ti, Pt and Au depositions per plane. Each strip is $180\text{ }\mu\text{m}$ wide and 21 mm long with a gap of $\sim 20\text{ }\mu\text{m}$ between each strip. This effectively gives a resolution per plane of $180\text{ }\mu\text{m}$ which is not a problem considering that the intrinsic position width of the beam is $\sim 200\text{ }\mu\text{m}$ [63]. In principle the use of multiple planes provides a higher resolution overall. The active area of each plane is roughly $21\text{ mm} \times 21\text{ mm}$. All four planes are rotated $\sim 11.3^\circ$ with respect to the vertical so that the incident electrons strike the planes at close to 90° as seen on fig. 5.10. Lastly each plane is held at -400 V providing a typical detector signal of ~ 9000 electrons[63].

The choice of diamond over traditional silicon detectors was due to diamond's large tolerance to radiation[63]. This is due in part to the large band gaps and the highly packed lattice of diamond suppresses leakage currents. Lattice defects are also unlikely in diamond. After an estimated electron rate with a total dose of $\sim 10\text{ MRad}$ during the entire 2 year experimental running, we did not observe a significant degradation in the electron detector signal[63]. This estimated rate is likely higher as it does not include a dose due to photons.

The measured asymmetry was determined for each strip in each plane, after cor-

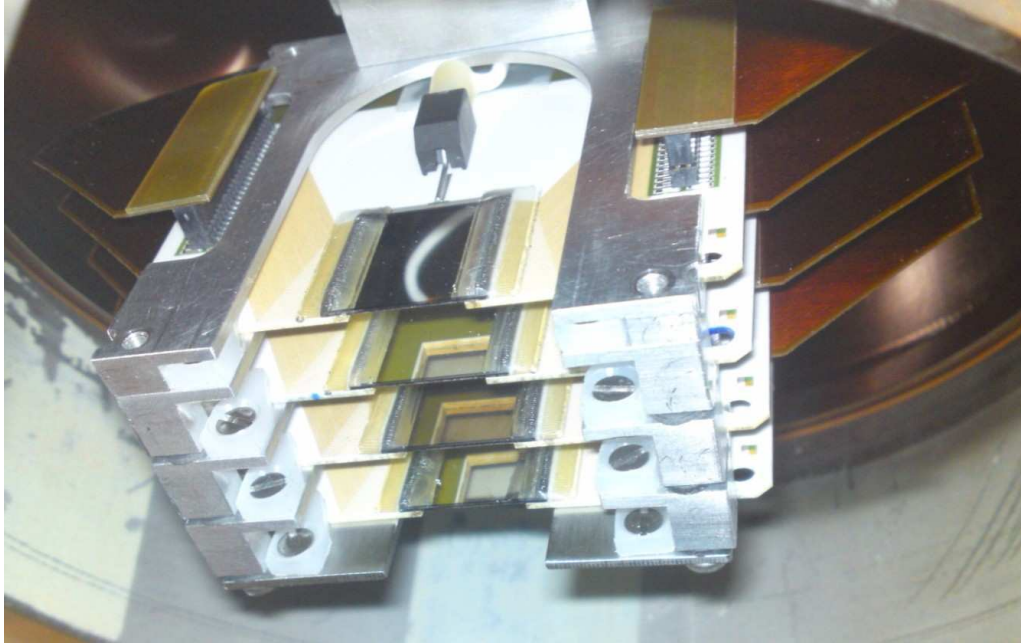
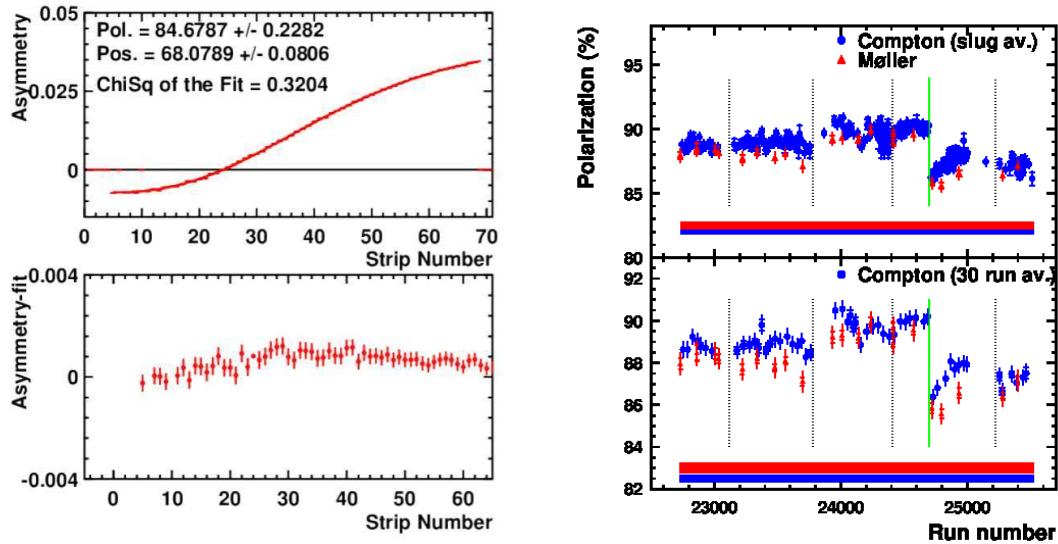


Figure 5.10: The electron detector was housed inside an aluminum can that sits atop the beamline. In this picture, looking at it from below, we see the four mounted planes, where the inner dark gray rectangles are the actual diamond strips.

rections for background contributions. A two parameter fit, seen in fig. 5.11a, was then performed against the simulated theoretical asymmetry. One of the parameters is the Compton edge, which can be a free parameter or a fixed parameter, and the other represents the beam polarization. Once the Compton edge is determined the final polarization for that run is determined. Final electron beam polarization for all of Run II determined from the electron detector are on fig. 5.11b[64].

5.2.3 Photon Detector

The Compton back-scattered photons are unaffected by magnetic fields and thus pass straight through the third dipole in the chicane and into a calorimeter array



(a) An illustration of the two parameter fit on the electron detector strip asymmetry. One of the determined parameters represents the electron beam polarization[63].

(b) The final electron detector based polarizations for all of Run II. They are grouped by Compton slugs (explained later) and listed as a function of Compton run number[64].

Figure 5.11: A two parameter fit and final Run II electron detector based polarizations.

built by collaborators from the Alikhanyan National Science Laboratory in Yerevan, Armenia. The calorimeter is composed of four 20 cm long stacked PbWO_4 (lead-tungstate) crystals each with a cross section of $3 \text{ cm} \times 3 \text{ cm}$. Stacked two-by-two the cross section of the calorimeter is $6 \text{ cm} \times 6 \text{ cm}$ and the front face is positioned 3.5 m downstream of the interaction point. Three non-scintillating optical fibers run the longitudinal length of the crystals with the upstream side of the cables exposed to the crystal and the downstream side coupled to Straight Tip (ST) connectors. The stacked crystals were then wrapped with a highly reflective mylar foil with the downstream face exposed, and the upstream face was also covered with the same material, and the three fiber ends inside. This downstream face is attached with

optical grease to a single 3 in diameter Hamamatsu R4885 PMT with a maximum gain of 5×10^6 [65]. The bialkali photo-cathode measures 77 mm in diameter and sticks out slightly past the back edge of the stacked crystals as evident from fig. 5.12 . To prevent saturation of the PMT signal and to make use of the dynamic range of the cathode, the PMT was held at -1750 V supplied by a CAEN High Voltage System (SY403). At this voltage the gain of the PMT is lower at $\sim 2 \times 10^5$.

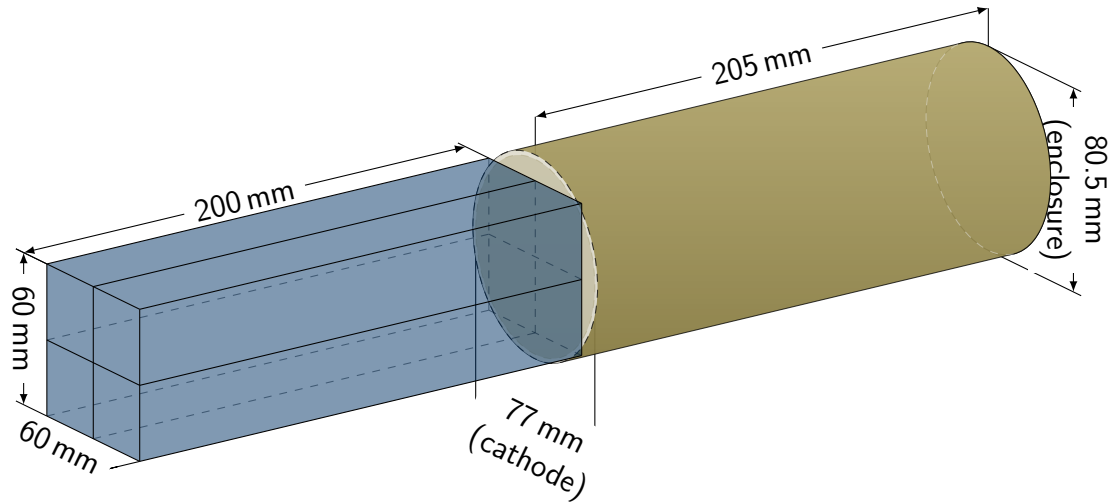


Figure 5.12: A drawing of the stacked crystals attached to the PMT. The PMT is a little larger than the four stacked crystals.

The entire detector, which includes the crystals, optical fibers and PMT, were wrapped with light tight black tape and placed inside a thermally isolated box cooled to $\sim 14^\circ\text{C}$ by a piezoelectric cooler (see fig. 5.13b) attached to the top of the box. The total light yield from PbWO_4 have shown to increase by $2\text{--}2.5\text{ \%/}^\circ\text{C}$ cooled[66]. Overnight bench tests showed temperature stability to within $\sim 1\%$ when cooled to $\sim 10^\circ\text{C}$ below room temperature and a total $\sim 20\%$ gain on light output from the crystals[67].



(a) Spare crystals which show the details of how the PbWO_4 crystals are stacked and wrapped before placing inside the enclosure.



(b) A view of the photon detector once fully enclosed inside the the thermal box. The blue box at the top is the pizoelectric cooler.

Figure 5.13: Photographs of the photon detector crystals as they are wrapped before placed inside the enclosure (left) and after inserted inside a thermally cooled enclosure (right).

Photon Detector Linearity System

The non-scintillating fibers were used with an external electronics system to map the linearity of the detector for a wide dynamic energy range. The fibers within the enclosure were coupled to ST-to-ST coupling connectors attached to the back side of the enclosure without optical grease. To decrease the possibility of cross talk between the detector and linearity electronics signals, additional 1 m long cables were used to place the electronics further away from the detector. A single light emitting diode (LED) was placed inside one end of an ST-to-ST coupling connector and filled with optical grease and wrapped around many layers of black electrical tape. The other was attached to one of the ST terminated fibers. The LED ends were soldered

onto a cable of fixed length whose other end was coupled to a LEMO connector. Identical LED and cable pairs were made to ensure proper timing between the LEDs and each was attached to an isolated electrical box which powered and controlled the LEDs.

5.3 Compton Data Acquisition

Analog signals from the Compton Photon Detector were routed upstairs through 200 ft low impedance cables to a patch panel in an electronics room situated next to the experimental control room inside the “Counting House” building. The Counting House is situated above ground and near the experimental halls where the radiation levels are safe for researchers to remotely control the experiment. Furthermore, the low radiation levels and lower electromagnetic noise are far more favorable conditions to the sensitive electronics compared to the extremely noisy environment of the experimental hall. Fast read-out electronics were installed on three VME based Read-Out-Controllers (ROCs) which combined to form our Data Acquisition system (DAQ). The ROCs were subsequently read out over the network by a Linux machine running an instance of the CEBAF Online Data Acquisition (CODA) software [68]. Any necessary logic signal processing or timing gates were generated and controlled through several racks containing a variety of Nuclear Instrumentation Modules (NIM) connected together through LEMO terminated RG-174 cables and spread out over various electronic crates. The read-out rate of the entire DAQ was synchronized to the 960/s helicity signal and was quickly written to disk for later processing. The Compton polarimeter DAQ was independent from the main Q_{weak}

DAQ, which was contained in a different floor of the Counting House and controlled by a different computer running its own instance of CODA. Though, attempts were made to ensure they were configured as similar as allowed by constraints of each system. Furthermore the Compton DAQ was divided into three main components, two different ROCs and a central triggering system that keep them in synchronization.

5.3.1 Timing and Helicity Trigger

The helicity information was encoded into several electronic signals generated at the injector then converted to optical signals and delivered to the Counting House electronics rooms via long fiber optic cables. The optical signals were then converted to NIM/TTL signals via a Fiber Translator module[24]. The main timing information is encoded in the Macro Pulse Signal (MPS) where the width of the large pulse defines the stable period of the helicity (T_{stable}) as illustrated by fig. 5.14. Likewise the low period of the MPS defines the transition time required for the helicity to become stabilized (T_{settle}). For the Q_{weak} helicity reversal rate of 960 Hz the corresponding settle and stable time periods were $T_{\text{settle}} = 70 \mu\text{s}$ and $T_{\text{stable}} = 972 \mu\text{s}$ respectively[69]. In the case of the Q_{weak} DAQ, the custom built integrating Q_{weak} ADCs (VQWKs) exhibited a start delay of $\sim 43 \mu\text{s}$ due to the internal electronic switching delays[69].

A custom VME board designed for the HAPPEX experiment and built by the electronics group at Jefferson Lab was used to provide the final timing information for the Compton DAQ[70, 71]. The HAPPEX timing board (HAPTb) has an effective clock of 400 kHz[71] which limits each step precision to $2.5 \mu\text{s}$. The trailing edge of the accelerator produced MPS provides the master trigger to the HAPTb, where a

configurable start delay of $17.5\ \mu\text{s}$ (7 HAPT B steps) was set to match the start delays of the main Q_{weak} DAQ. This configurable delay is in addition to the hardwired $15\ \mu\text{s}$ delay for the HAPT B integrating signal to stabilize and an additional $2.5\ \mu\text{s}$ (1 step) baseline pulse produced by the board. When measured by an oscilloscope it was confirmed that an additional $5\ \mu\text{s}$ delay was present[72] possibly due to misalignment of signals with respect to the internal HAPT B step size of $2.5\ \mu\text{s}$. With all delays added in the integrating signal is delayed by $\sim 40\ \mu\text{s}$, which is fairly close to the Q_{weak} start delay. A configurable integration time of $925\ \mu\text{s}$ (370 steps) was specified, which when accounting for misaligned timing with respect to the HAPT B step gives a total integrating time of all DAQ components of $930\ \mu\text{s}$ for each helicity. This gives us a buffer of $\sim 2\ \mu\text{s}$ before the end of the T_{stable} period and the start of the helicity flip.

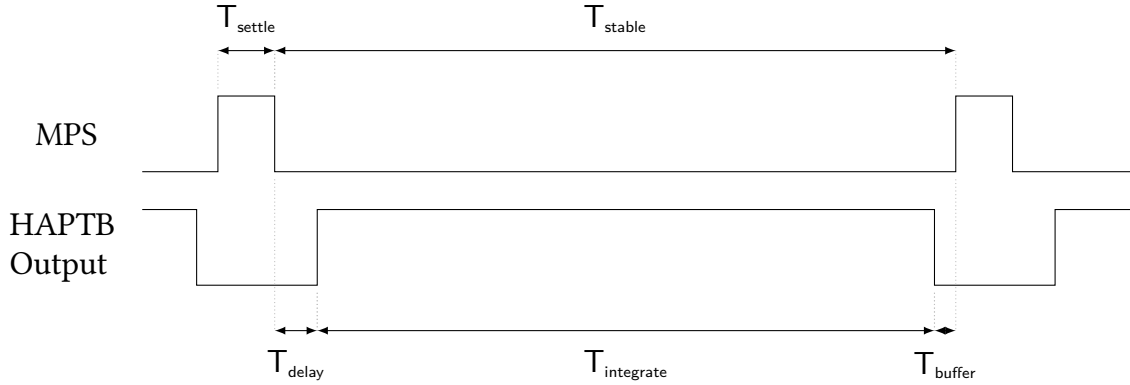


Figure 5.14: Timing diagram of the Compton DAQ showing the main trigger from the MPS and the output pulse from the HAPT B that defines the integrating window.

Due to the requirements of the HAPPEX experiment, the internal electronic switching of the HAPT B requires a minimum of $35\ \mu\text{s}$ to $40\ \mu\text{s}$ delay before accepting another trigger after the end of the integrating period. This did not present a

problem given that it fits well within the $T_{\text{settle}} = 70 \mu\text{s}$ period.

The data in the two distinct ROCs were properly read out and kept in synchronization by using the Jefferson Lab Trigger Supervisor System[73]. This custom built system, designed by the DAQ group at Jefferson lab, is composed of a main board referred to as the Trigger Supervisor (TS) which acts as the central directory for all buffered data in the various ROCs' buffers. The larger size 'D' VXI TS card requires that the TS board sit in a custom built VME/VXI hybrid crate. The VXI portion of the crate houses up to three VXI boards while the VME side can house twelve standard VME boards[73]. Communication between the TS crate and the individual ROC is done via a ribbon cable connected to a specialized board on each ROC referred to as the Trigger Interface (TI) board.

Among the many functions of the Trigger Supervisor system is the ability to consolidate the read-out of up to eight prior events in the ROCs buffers, where each event in this case corresponds to one helicity state. The TS board buffer, in this case, holds the link to the fragments of data on the various ROCs for each event[73]. Additionally the Trigger Supervisor keeps track of all the system busy signals and was used to provide a veto signal for any external trigger and a "stop" signal to the ROCs when no valid data is expected.

5.3.2 Scalers

Several Struck SIS3801 scaler modules were used and configured in either 24 bit or 32 bit resolution on each of the individual 32 input channels of each module. Scaler electronics are essentially counting devices that increments when a signal comes in. A full map of all the scaler inputs can be found in table A.1. Special consid-

eration must be made to account for any dead time which can be caused by the scaler electronics being slower than the incoming input rate. To account for these effects we also sent signals from precisely known frequency generators, which we call clocks, of 4 MHz and 1 MHz respectively. This served two purposes as the total number counts of the clocks by the scalers give us a precise determination of the time window the scalers were counting, and any deviation from the specified time could indicate scaler dead time. So every one of the remaining 30 scaler channels were normalized to the 4 MHz clock as such

$$N_{cn} = N_s \left(\frac{t_s f_c}{N_c} \right), \quad (5.20)$$

where t_s is the time window the scalers were counting, f_c is the nominal frequency of the clock (in this case 4 MHz), N_s and N_c are the raw counts of the the desired scaler channel and clock respectively, and lastly N_{cn} is the clock-normalized counts of this scaler channel. However, should we want to instead convert it to the input frequency on that scaler channel, we can instead use

$$F_s = N_s \left(\frac{f_c}{N_c} \right), \quad (5.21)$$

where F_s is now the frequency of the corresponding to the scaler channel. If a V-F was used, then this frequency can be directly correlated to the output voltage from the attached source. Lastly we can get the length of the integrating window on the scalers by using the counts on the clock: $t_s = f_c N_c$.

For the total 930 μ s integrating time specified by the HAPPEX timing board, the number of counts from the 4 MHz clock on the scalers was 3720 counts per helicity

window. Overall I observed no more than two missed counts, and never an over-count. This gives an upper limit to the overall scaler dead time of less than $\sim 0.05\%$. While such a small dead time is insignificant and means that the scaler channels can be used without any clock-corrections, it was a necessary check to ensure scaler dead time remained low during the entire running.

A feature of the Struck SIS3801 is the capability to accept multi-triggers, that in consequence allows one to start and stop the scaler count without resetting the overall count. When coupled to one of the fast clocks, such as the 4 MHz discussed above, provides a decent timing for the incoming trigger. This plays a crucial role in the next section when I discuss the photon self-trigger.

5.3.3 Photon Detector Signal

The PMT anode signal was split into three components by a LeCroy 428F Quad Linear Fan-IN/Fan-OUT module¹. One of the three outputs was digitized by a CAEN V792N QDC (charge to digital converter). The second copy was first amplified twice by a Phillips Scientific 771 Quad DC-300 MHz Amplifier before being sent to be digitized by a Struck SIS3320, a commercial digital to analog converter with flash memory (FADC) from Struck. The Struck SIS3320 is capable of sampling at up to 250 MHz from a range of 0 V to 4 V with 12 bit precision and flash storage for 32 million samples per channel. A single channel was used to digitize the single PMT signal at 200 MHz. The third and final copy was used to build a trigger for the “snapshots,” as I will describe in detail at the end of this this section. First, I will focus on

¹In actuality, the signal first passed through a second Fan-IN/Fan-OUT (a Phillips Scientific 740DS Quad Linear/Logic Fan-IN/Fan-OUT). However, this was a remnant of testing phase when we were connecting one of the outputs to an oscilloscope and/or to the Møller DAQ for testing.

the digitization of the second output.

While digitization of the photon signal can be made by reading out the individual samples of the Struck SIS3320 for a given photon pulse, this method is very time-costly and unfeasible at the high rates seen throughout the running. This is further complicated by the fact that events must properly be timed with the relatively high helicity flip rate of 960/s. Instead we rely on a feature of the Struck SIS3320 that provides six integrating modes, known as accumulators, that rapidly integrate all samples over a given gate and each governed by a different threshold, where the gate in this case is the helicity flip rate. The first accumulator (Accum0) integrates over the entire helicity window without restriction, while the next three are defined by two set thresholds V_{v1} and V_{v2} , where $V_{v1} < V_{v2}$. Accum1 integrates over samples that are less than V_{v1} , Accum2 integrates over samples between V_{v1} and V_{v2} , and Accum3 over samples above V_{v2} . The resulting integrated value corresponding to these four accumulators can be expressed as

$$V_{\text{raw}}^n = \sum_{s=0}^{f\tau} (V_s \kappa_n(V_s)), \quad (5.22)$$

where V_s is an ADC value corresponding to sample s , f is the integrating frequency (200 MHz), $\tau = T_{\text{integrate}}$ specified in the previous section, and κ_n is an accumulator

dependent value defined as:

$$\kappa_0(V_s) \equiv 1, \quad (5.23)$$

$$\kappa_1(V_s) \equiv \begin{cases} 1 & \text{for } V_s < V_{v1} \\ 0 & \text{for } V_s > V_{v1} \end{cases}, \quad (5.24)$$

$$\kappa_2(V_s) \equiv \begin{cases} 0 & \text{for } V_s < V_{v1} \\ 1 & \text{for } V_{v1} < V_s < V_{v2} \\ 0 & \text{for } V_s > V_{v2} \end{cases}, \quad (5.25)$$

$$\kappa_3(V_s) \equiv \begin{cases} 0 & \text{for } V_s < V_{v2} \\ 1 & \text{for } V_s > V_{v2} \end{cases}. \quad (5.26)$$

An important distinction is that while the total number of samples taken during the integrating period of eq. (5.22) is $N = f\tau$, the total number of samples in each accumulator may differ as they are dependent on κ_n like so

$$N_n = \sum_{s=0}^{f\tau} (\kappa_n(V_s)). \quad (5.27)$$

In the case of Accum0 the total number of samples in the integral is $N_0 = f\tau = 232,500$ samples per helicity. The remaining two accumulators (Accum4 and Accum5) could have different timed gates but were unused in our configuration. As far as the analysis of this thesis is concerned, only the measurements from Accum0

were analyzed and considered.².

While reading out all 232,500 samples is time-costly, there is still sufficient time to read out a few blocks of samples corresponding to arbitrary photon signals. We configured our DAQ to read out a single block of 256 contiguous samples which comprises a single photon “snapshot”. Each snapshot provided a complete $\sim 1\ \mu\text{s}$ view of a photon centered at the window. Since the capabilities of the SIS3320 in accumulation mode did not provide timing information to identify individual photons in the large $\sim 1\ \text{ms}$ helicity window, we instead relied on the timing information of the multi-triggered SIS3381. The trigger to the scaler was in essence the third output of the Fan-IN/Fan-OUT from above.

The third output was first amplified three times by another channel in the Phillips Scientific 771 Amplifier before passing through a Phillips Scientific 706 Leading Edge Discriminator set to $\sim 30\ \text{mV}$. Both lower and larger discriminator values were tested: at lower settings there is a higher probability of triggering on noise, while a higher setting discards too many of the low energy region photons in the Compton spectrum. Since the SIS3381 could not keep up with the $\sim 250\ \text{kHz}$ rates observed during the laser period, a pre-scaler device was set to 10^3 . In essence, the pre-scaler blocks all but one out of the 10^n input events, where n is a configurable integer. The pre-scaled signal would then be sent to a LeCroy 365AL Dual 4-Fold Majority Logic Unit. During normal operations the logic unit was configured to require at least one input signal to be active before firing a new trigger.

²Though, initially the intention was to use Accum2 with known thresholds, but due to the difficulty in identifying the Compton edge during the beginning of the experiment, and the ease of which we could already perform an analysis on Accum0, the goal of relying on Accum2 was abandoned. While all accumulator data was still recorded, there is no guarantee that the thresholds were optimally set.

Out of the four inputs of the LeCroy 365AL logic unit, one was passed onto a channel of a LeCroy 222 NIM Dual Gate and Delay Generator that generated a $\sim 10 \mu\text{s}$ gate that was sent to the LeCroy 365AL veto signal to suppress any further triggers being created while the present one was being processed. This same channel also mixed the signal from the busy channel of the photon detector trigger interface or the inactive signal from the HAPT B produced MPS signal. This further insured that no triggers were produced while the system was busy.

A second output of the LeCroy 365AL was sent to another channel of the LeCroy 222 Gate Generator to produce a $\sim 1 \mu\text{s}$ gate sent to the QDC trigger input. The third output was sent through a level translator and then delayed via a cable and NIM delay module before being passed onto a final level translator and onto the Trigger Supervisor module. This input was mostly used during the testing phase of the experiment when the accumulator mode of the Struck SIS3320 was not being used.

Finally, the fourth output was sent to another channel of the LeCroy 365AL logic unit in tripled coincidence with the MPS and inverse MPS signal from the HAPT B board. One of the two outputs of this channel was sent to an input on an SIS3381 scaler module to count the number of triggers, while the second output was sent to control the trigger on the second SIS3381 scaler module to provide timing information. Then to get the exact memory address in the Struck SIS3320, that contains the samples of this snapshot, we simply compare the counts of the FADC clock and the SIS3381 counts of its clock as such:

$$\text{memory address} = \frac{1}{2} \left(\frac{N_{\text{prescaled}} N_{\text{scaler}}^{4 \text{ MHz}}}{N_{\text{FADC}}^{\text{Accum0}}} - S_{\text{offset}} \right),$$

where S_{offset} is a manually set number of samples offset to ensure the photon signal

is centered in the window. Throughout this running period $S_{\text{offset}} = -170$.

5.3.4 Linearity Electronics

The external linearity electronics were modeled after a system developed for the Hall A Compton Polarimeter[74] and modified to match our requirements, as necessary. The key characteristic of this system is the use of a central control board that provides timing and state information to two external boards which themselves power an LED based on the signal from the control board. The use of a single board ensures proper synchronized timing between all other components, and the use of external boards for the LEDs minimizes cross talk between the two LEDs.

5.3.5 Slow Data (EPICS)

The Experimental Physics and Industrial Control System (EPICS) plays a key role in the operation of the accelerator by collecting and publishing information that can be accessed throughout the entire accelerator network. Throughout the data taking period we relied on EPICS to monitor the health of the experimental components. Some of this information should prove useful during the analysis phase of the experiment. However, most of this information represents slowly changing settings, such as the reversible half wave plate setting and other magnet set points. Hence, the information was not always read out at the helicity reversal rate of 960/s. Instead the Compton DAQ system read out a portion of the EPICS at a much slower rate of once every ~ 30 s.

This “slow data” allows us to record information not directly associated with our experiment. Information such as settings on the other halls, such as their respective

beam energies and current, or general settings of the accelerator itself, all of which may have an indirect effect on our experimental data. The caveat however, is that some of the EPICS values may have been set manually, and not read out, so can not be guaranteed to be up to date and exact. Regardless of this limitation the system provided additional information useful in diagnosing problems with the analysis.

5.3.6 Data Processing

I conclude this chapter with a discussion of the data and the various stages of analysis that go into producing the final result. The goal is not to detail the specific types of analysis for any given detector, but rather to show the general flow of the analysis. Figure 5.15 we see the steps required before reaching a result and I will describe them accordingly next.

Raw Data and the Pre-Analysis Stage

The information read out of the ROCs by an instance of CODA are written to disk into individual files whose content is structured in an event-by-event format known as evio. An event in this context corresponds to the read out of all integrals from each of the electronics in the three ROCs at the end of a helicity period. The data written at this point is mostly considered “raw,” and divided into hourly periods called runs. To limit the size of each individual file, CODA was configured to write to a new file once 2 GB of data is reached, which means that each typical hourly run is divided into several “runlets” corresponding to each of the raw data files written for each run. An average of four to five runlets were written per run determined mostly by the exact length of a run.

The raw data runlets are then processed through QwAnalysis the Q_{weak} C++ Analyzer Framework designed to be a flexible parity data analyzer. QwAnalysis was extended to produce a dedicated version to specifically process the Compton polarimeter data (QwCompton). This ensures that both data from Q_{weak} DAQ and the Compton DAQ are analyzed in a similar fashion, but with the flexibility of addressing the unique differences of the Compton polarimeter. Each detector measurement corresponds to a yield (Y_{mps}), which, after proper calibration, represents a specific measurements with its corresponding units. For example, the BCM yield represents the beam current in units of μA . We then leverage the features of ROOT, an object oriented data analysis framework[75], to organize this data into individual ROOT branches on a ROOT tree, which are then written to disk as ROOT files.

We also write a second tree that contains the yields, differences and asymmetries for every helicity quartet pattern in the runlets. Here the helicity level yields, and corresponding yield differences, are averaged and determined as

$$Y_{hel} = \frac{1}{4}(Y_1^+ + Y_2^+ + Y_1^- + Y_2^-) \quad \text{and} \quad \Delta Y_{hel} = \frac{1}{4}((Y_1^+ + Y_2^+) - (Y_1^- + Y_2^-)), \quad (5.28)$$

with the helicity level asymmetry determined as the ratio of the two:

$$A_{hel} = \frac{\frac{1}{4}((Y_1^+ + Y_2^+) - (Y_1^- + Y_2^-))}{\frac{1}{4}(Y_1^+ + Y_2^+ + Y_1^- + Y_2^-)} \equiv \frac{\Delta Y_{hel}}{Y_{hel}}. \quad (5.29)$$

A third tree is also written containing the EPICS readouts of section 5.3.5. This process of producing ROOT files can be repeated multiple times as needed to address issues found by deeper analyses, each time labeled as an incremental “pass” starting with one.

Up to this stage we have maintained the analysis process and software as identical to the Q_{weak} analysis scheme as possible. From here forward the the analyses of the two diverge given to their unique features. I will not discuss the specific differences, choosing instead focusing exclusively on how I have processed these produced ROOT files.

Second Stage Data Organization and Analysis

In order to minimize any biasing effects arising from any time dependent components on the detector measurements, the analysis of the photon detector data was based on shorter time periods structured around the state of the laser. The necessary background corrections described in section 6.1.3 dictated that the data be structured from a laser off time period immediately followed by a laser on period and finally followed by a laser off period. The individual runlet ROOT files are chronologically linked together and an a custom written program automatically determines the good laser patterns for the entire run.

This program, which I refer to as RunMacros, is the center piece for all the following Photon Detector based analyses. After determining the laser patterns, they are stored on a MySQL[76] database and linked to the appropriate run number. RunMacros will then load and run a specified analysis stored in a macro. Each macro must be compiled as a specially formatted dynamic loading library, with extension .so. Each analysis described in the preceding chapter has a corresponding library associated with it and RunMacros will then store the results on the MySQL database for each of the laser patterns. The main goal of using RunMacros to run the analysis was to ensure that all macros use the same data when performing their independent

laser pattern based analysis. In addition it also provides common central functions so that writing these individual macros becomes easier.

The end result of this stage is the filling of the MySQL database with values and measurements that are all linked together by their corresponding laser pattern for the entire data. This tends to be significantly much smaller in size than the large runlet ROOT files. At this point we may choose to go back to the previous stage and start another pass, which would require that this stage be repeated too. Alternatively, if we are satisfied with the information stored in the database, we can proceed to the next stage.

Final Data Subset and Analysis

At this stage the values stored in the database must be organized into time periods and configurations for final polarization extraction. To make it easier to perform this analysis, and to limit choke points due to limited network bandwidth, I then produce small ROOT file containing the entire results on the database. Since the database contains results organized by pattern, at this stage I have the option to organize the ROOT files either by pattern, or to average them by either run or a larger period referred to as a slug. A slug contains anywhere between four to eight hourly runs, and correspond to periods of similar settings. The most common changed setting was the insertible half wave plate discussed in the previous chapter. For run, slug or larger groupings, I perform an error weighted average of all good run pattern data within the grouping.

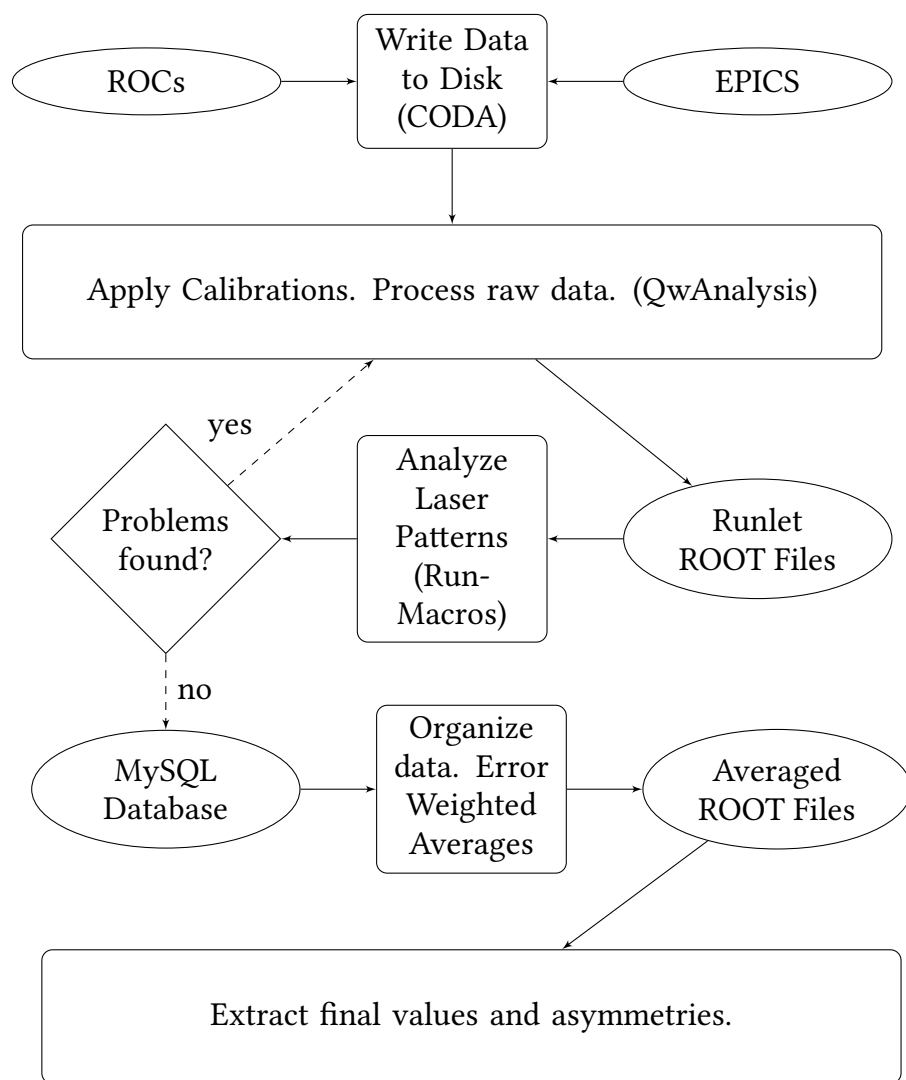


Figure 5.15: Flow chart illustrating the steps used in processing the data. Starting with the initial acquisition at the top and ending with the final results at the bottom.

Chapter 6

Photon Detector Analysis

This chapter will highlight my primary contribution to the Q_{weak} experiment, which is the analysis of the data collected, and the subsequent determination of absolute time based polarizations, from the photon detector.

As the key central piece of data from this detector system is the signal from the single PMT, the task of determining a beam polarization comes down to determining the independent components of the following equation

$$A_m = P_e P_\gamma A_{th}, \quad (6.1)$$

where A_m and A_{th} are the measured asymmetry and analyzing power of the photon detector respectively and P_e and P_γ are the beam and laser polarization respectively. As such, I will break up this chapter in a detailed discussion of my work to determine the measured asymmetries and analyzing power accordingly. I will also discuss the work performed by others to determine the laser polarization. I will conclude the chapter with a discussion of the results of this analysis.

6.1 Measuring the Experimental Asymmetry

The measured asymmetry that we report corresponds to the asymmetry on the integrated yields of the first Accumulator (Accum0) in the FADC described in section 5.3.3. This requires that any measurement used in the determination of these yields must be properly calibrated and corrected, if needed. While the processing of data is already introduced in section 5.3.6 a special note should be made on the determination of any value from a device. Most notably, a digital device usually reports values in some internally defined fashion, either as a channel number from an ADC or a count from a counting device and so forth. To calibrate this value and convert it to a known quantity, one would have to apply a calibration factor f that converts from internal units to known units of quantities, such as channel number to volts, counts to frequency and so forth. We must also make note of the zero offset, that is the value a device reads when a null reading is expected. This can be due to electronic offsets or part of the design of a device, such as an ADC reading voltage drop rather than voltage gain. We call this zero offset a pedestal and denote it as V_{ped} . Then the detector measured value (V_{det}) is defined as a function of the pedestal, calibration, and the raw measured value V_{raw} as

$$V_{\text{det}} = (V_{\text{raw}} - V_{\text{ped}}) \cdot g. \quad (6.2)$$

Then the helicity level measurements and corresponding asymmetry from eqs. (5.28) and (5.29) can now be defined as

$$A_{\text{det}}^{\text{hel}} = \frac{\Delta V_{\text{det}}^{\text{hel}}}{V_{\text{det}}^{\text{hel}}}. \quad (6.3)$$

In the case of the FADC described in the previous chapter, the measurement corresponds to the first accumulator setting which integrates over the entire helicity window. I distinguish the detector asymmetry is distinguished from the real polarized electron-photon scattering asymmetry in that it does not inherently take into account effects which can dilute the asymmetry. In section 6.1.3, for example, I will describe the effects of backgrounds on the asymmetry, and the respective methods to remove these effects.

6.1.1 Calibrating the Charge Monitors

In order to calibrate the beam current monitors, introduced in section 4.7.2, a special run was taken (run 22617) where the beam current was alternated between on and off periods. Whenever the beam would be turned on it would be turned on to an increment of $20 \mu\text{A}$ more than the previous on period, all the way up to $\sim 180 \mu\text{A}$, at which point the process would reverse until the current reached $20 \mu\text{A}$. The repetition of beam off states are so that we can monitor the stability of the Unser.

The beam off periods allowed us to determine the Unser pedestal and since the signal of the Unser system is a frequency we use eq. (5.21) to convert scaler counts back to an unser frequency (F_{unser}), define the Unser pedestal to be F_{unser}^{ped} and using the unser calibration $f_{unser} = 2.498 \times 10^{-3} \mu\text{A}/\text{Hz}$ we can determine the absolute beam current by

$$I_{unser} = (F_{unser} - F_{unser}^{ped}) \cdot f_{unser}, \quad (6.4)$$

where I_{unser} is the Unser current in μA . The calibrated current vs time can be seen in fig. 6.1a. Cuts as a function of time had to be applied manually to ensure only good periods were considered for the calibration, and any period with beam instability

was excluded.

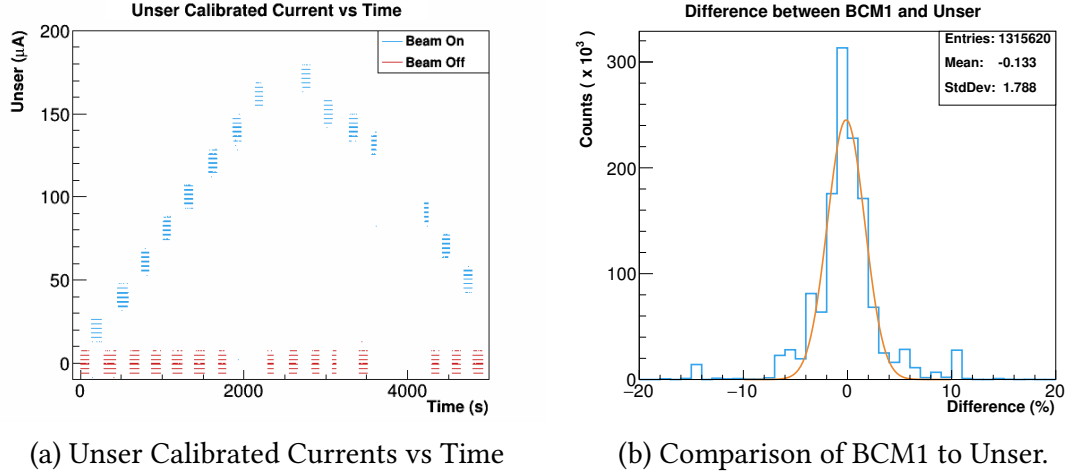


Figure 6.1: Left: The calibrated Unser current for run 22617 plotted as a function of time. The horizontal dashes are caused by the bit-level precision of the scalers. Right: The difference between the calibrated BCM1 and Unser measured currents.

Since the remaining BCM devices lack a known absolute calibration, they are calibrated against the Unser. Using the BCM frequency ($F_{bcm,i}$) measured by the scalers, we perform a fit against the Unser of the form

$$F_{bcm,i} = f_{bcm,i} \cdot I_{unser} - F_{bcm,i}^{ped} \quad (6.5)$$

and determine from the fit the BCM calibration $f_{bcm,i}$ and corresponding pedestal $F_{bcm,i}^{ped}$. The fit residuals of all three BCMs 1, 2 and 6 show that the precision of the calibration is best at currents greater than 60 μA . A different calibration had to be performed and determined for lower currents ($I < 5 \mu\text{A}$) and a third calibration run was taken (run 25362) near the end of the experiment. However, midway through the data taking period the Unser stopped responding and we were unable to use it in the calibration. Instead, the calibrations were performed against the previously

determined calibrations in order to deduce the overall stability over the data taking period and found them to vary by no more than 2.8 %, well within two standard deviations as taken from fig. 6.1b. A summary of the determined calibrations and pedestals for the beam monitors are on table A.2.

Normalizing Measurements to Beam Current

When dealing with measurements of rates or the integrated signals of Accum0, we have to consider that these quantities are dependent on the beam current at the time of the measurement. So for example, take the measurements of Accum0 V_1^0 and V_2^0 for two distinct helicity periods, with corresponding beam currents I_1 and I_2 respectively. Then under the condition that $I_1 \neq I_2$ we should also equally find that $V_1^0 \neq V_2^0$ for all things considered. So instead we choose to normalize them by beam current to reach $I_2 V_1^0 = I_1 V_2^0$, however, doing so at the helicity level will add noise due to the bit-precision of the BCM scalers. Hence, in order to normalize by beam current while minimizing the effect of the BCM precision, we average the measurements for a sufficiently large time such that the current normalized value $\langle V_{\text{norm}} \rangle$ is now dependent on the average $\langle I \rangle$ is

$$\langle V \rangle_{\text{norm}} = \frac{\langle V \rangle}{\langle I \rangle}. \quad (6.6)$$

I find that averaging the charge above 15 seconds is already sufficient to reduce the noise on the current.

6.1.2 Calibrating the Position Monitors

Unlike the charge monitors, a position monitor required calibration of the relative gains of the individual antennas as outlined in eq. (4.3). Right after the calibrating run of the charge monitors another special run (22619) was taken that alternated between beam on and off states. The beam off periods allowed us to determine the pedestal of the individual BPM antennas while the beam on states allowed us to determine the conversion between beam current and the output of the individual antennas. Choosing the nominal current of the experiment $\sim 180 \mu\text{A}$ will guarantee that we map the full dynamic range of the BPM. We perform the same fit as eq. (6.5) replacing the BCM terms by the corresponding BPM terms, where the slope terms now correspond to the calibration factor $f_{bpm,(i,j)}$ for the i -th antenna on the j -th BPM. Then from eq. (4.3) we define the relative gains of the antennas as the ratio of slopes:

$$\alpha_i = \frac{f_{bpm,(i,j)}^+}{f_{bpm,(i,j)}^-}. \quad (6.7)$$

Then we plug in the ADC to position conversion constant of $k = 18.81 \text{ mm}/\text{adc}$, and we set the overall BPM gain to $f_i = 1 \text{ adc}$ to complete the calibration. This calibration was performed once for the entire second running period and the results are in table A.3.

Centering the Electron Beam on the Compton Laser

The process of centering the electron beam on the laser, by scanning over a wide range in the vertical, proved incredibly useful in the calibration of the BPMS. Figure 6.2a is an example of one such period, which started about fifteen minutes into

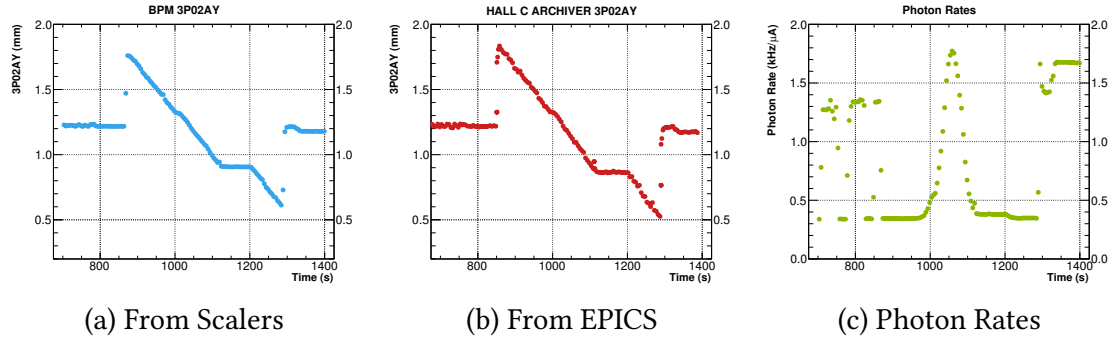


Figure 6.2: An example of the five minute beam motion as it scans the vertical axis to identify central position of the laser, as measured by BPM 3P02A, which is upstream of the IP. The horizontal axis corresponds to the time since the start of the run (23678). A comparison between the Scaler calibrated data (left) and the EPICS values retrieved from the Hall C Archiver (center). The corresponding current normalized photon rates are also shown (right).

the run. The data shown correspond to BPM 3P02A, which is on the laser table and upstream of the interaction point and have been averaged over 5000 helicity periods (roughly five seconds) to smooth out the resolution of the scalers. Around the fifteen minute mark the beam was abruptly moved in the positive vertical direction and then slowly moved down and scanning over a ~ 1 mm region. From fig. 6.2c we see that before the scan the photon detector rates were ~ 1.35 kHz/ μ A and after proper centering jumped to ~ 1.65 kHz/ μ A which corresponds to a net gain of $\sim 22\%$ in signal. We ignore the drastic 1 kHz/ μ A jumps before this period as the jumps correspond to the periods when the laser was unlocked for background measurements. During the scanning the laser was left in the locked state for the duration of the scan. The Gaussian distribution shown in fig. 6.2c is a convolution of the width of the laser and electron beam.

As a consequence of these scanning periods, the predicted behavior of the beam allowed us to quickly test the calibration against values provided by the accelerator

control system through EPICS. In particular, we were quickly able to identify the sign of the calibrations and the relative angles of the corresponding BPMS. The lack of an exact match is not worrisome, as the calibration and offsets of the EPICS values were likely not optimal. One thing that becomes apparent when we take a look at the horizontal direction is that there appears to be a horizontal component when scanning vertically as seen on fig. 6.3a. The accelerator provided values also seem

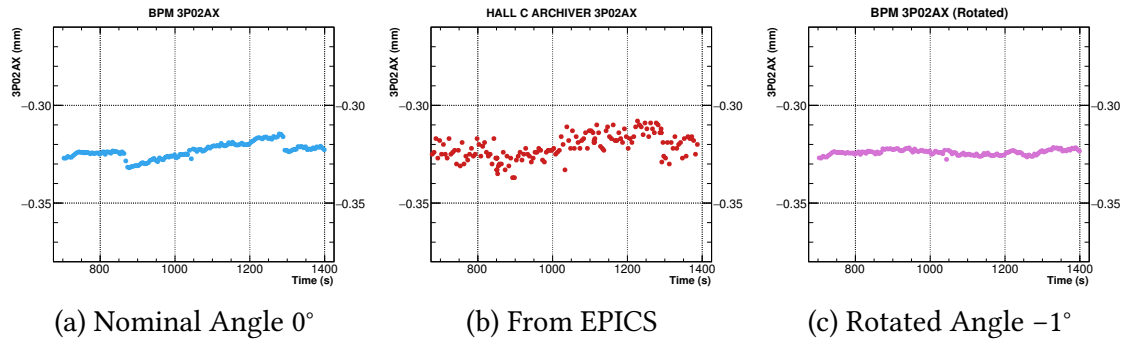


Figure 6.3: During special periods where the beam is re-centered on the photon target by scanning purely in the vertical direction, BPM 3P02A shows evidence of horizontal motion. This is seen both on the data (left) as well as the accelerator read-outs (center). However, by introducing a small angle offset of just -1° the horizontal component disappears, which points to an offset as the likely culprit.

to exhibit this behavior (fig. 6.3b), at first indicating that it may be a real effect not due to the calibration. However, after finding no evidence of this motion on other monitors, the suspicion laid on a misalignment of this single BPM. Unlike all other BPM's, 3P02A is un-rotated with respect to the beam axis giving it a nominal angle of 0° , and the introduction of an offset of just 1° is enough to remove any horizontal component as seen on fig. 6.3c. The introduction of this small offset did not significantly affect the more important vertical axis, and hence the calibrations were left at the nominal 0° angle.

6.1.3 Background Sources and Corrections

Before discussing how we account for any background contributions, let me first expand on some known sources of background on the detector. One such source is Synchrotron radiation, the unavoidable consequence of charged electrons bending in a magnetic field.

Synchrotron Radiation

A charged particle will radiate photons when accelerated such as when bending through a magnetic field. Each photon carries energy ϵ in a direction specified by the polar angle θ and azimuthal angle ϕ with respect to the direction of the electron momentum. In each helicity window, the number of electrons passing through the magnetic field of the third Dipole is on the order of 10^{12} when the electron beam current is $180 \mu\text{A}$. Each of these electrons is capable of emitting one or more photons which may hit the photon detector. Therefore, to understand and quantify the expected contribution of synchrotron radiation to the signal on the photon detector we follow the procedure detailed in [77].

Start with the total power emitted by a single electron bending in a dipole given by [77]

$$P_0 = \frac{2r_0mc^3\beta^4\gamma^4}{3R^2}, \quad (6.8)$$

where r_0 is the Bohr radius, m is the mass of the electron, c the speed of light, β and γ are the velocity coefficient and Lorentz factor, respectively. The last term R is the called the radius of curvature a particle in an uniform magnetic field moving in a circular trajectory and is commonly referred to as the bending radius. We will see

later that the probability distribution of emitting a photon behaves logarithmically with respect to energy of the emitted photon. We can identify a cut off energy ϵ_c such that the probability of a photon being emitted with energy ϵ' where $\epsilon' > \epsilon_c$, can be treated as zero. This cut off energy is called the “critical energy” and is defined by [77]

$$\epsilon_c \equiv \frac{3hc\gamma^3}{4\pi R}, \quad (6.9)$$

where h is the plank constant. Let $P(P_0; \epsilon, \theta, \phi)$ be the density function of emitted photons. Then by taking the partial derivatives of P with respect to the solid angle $\Omega = \sin \theta d\theta d\phi$ and photon energy ϵ we get[77]

$$\frac{\partial^2 P}{\partial \Omega \partial \epsilon} = \gamma \frac{P_0}{\epsilon_c} F(\xi, \psi), \quad (6.10)$$

where ψ is the angle of the emitted photon with respect to the bending plane and $\xi = \epsilon/\epsilon_c$. Recall that ϵ_c is the maximum energy with nonzero probability, and therefore it is safe to treat $\xi \in [0, 1]$. The function F is defined as

$$F(\xi, \psi) = \left(\frac{3}{2\pi}\right)^3 \left(\frac{\xi}{2}\right)^2 \eta \left[\eta K_{2/3}^2 \left(\frac{\xi}{2} \eta^{3/2}\right) + \gamma^2 \psi^2 K_{1/3}^2 \left(\frac{\xi}{2} \eta^{3/2}\right) \right] \text{ for } \xi \leq 1, \quad (6.11)$$

where $\eta \equiv 1 + \gamma^2 \psi^2$, and K_ν are the modified Bessel functions.

The bending radius of an ultra relativistic electron with energy E_e passing through an uniform magnetic field of intensity B is given by

$$R = \frac{E_e}{cB}. \quad (6.12)$$

Using the nominal Q_{weak} beam energy of $E = 1.16 \text{ GeV}$ and the dipole beam field

set at 0.54 T, we find $R = 7.1122$ m. Then we use eqs. (6.10) and (6.11) to produce the density of emitted photons as a function of mean photon energy $\langle\epsilon\rangle$ and out of plane angle ψ seen in fig. 6.4a where I used $\gamma \sim 2.66 \times 10^{13}$ and $\beta \sim 1$. We quickly notice in

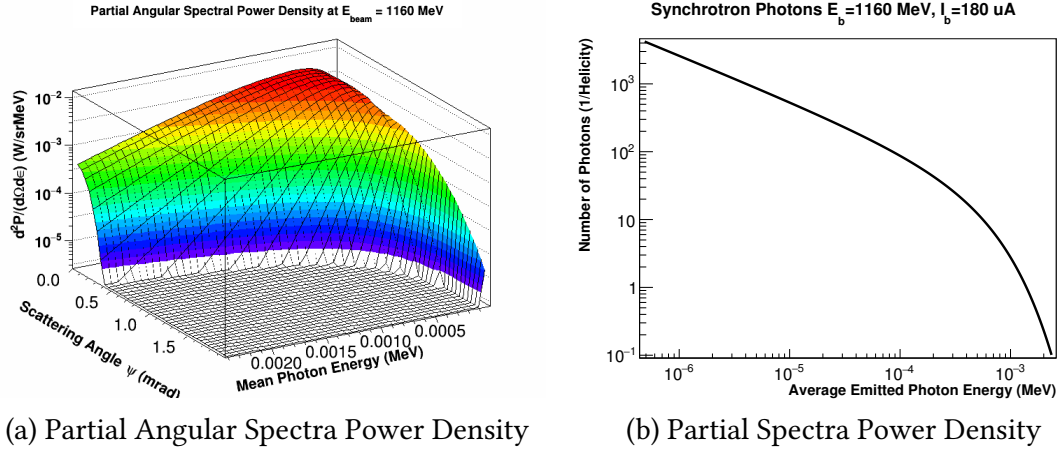


Figure 6.4: By following the procedure of [77] we can get the density of power incident on the photon detector as a function of the out of plane angle ψ (left). By integrating over all ψ and the entire helicity window we can get the expected density of Synchrotron photons (right).

fig. 6.4a that at $\psi = 1.5$ mrad the density of emitted photons is already three orders of magnitude smaller than the $\psi = 0$ mrad. This means that the majority of photons are emitted at very forward angles and tangentially to the direction of the electron motion. Therefore, we can integrate eq. (6.10) for all ψ without loss of generality to get [77]

$$\frac{\partial n'}{\partial \xi} = \frac{P_0}{x\epsilon_c \xi} \left(\frac{9\sqrt{3}}{8\pi} \xi \int_{\xi}^{\infty} K_{5/3}(u) du \right), \quad (6.13)$$

where $n' = dn/dt$ represents the rate of emitted photons per unit time. Then using the above equation and integrating the rates over an entire helicity window ($t \sim 1$ ms) we produce fig. 6.4b. At this beam energy and current we expect minimal Synchrotron photons with energies larger than 1 keV. Though the net deposited



Figure 6.5: Scarring of the copper beam pipe exit window after two years of running at high current. The narrow burn mark is a characteristic sign of Synchrotron radiation.

power integrated over all emitted photons can still be substantial, as is evident in burn marks seen in fig. 6.5 after ~ 8000 h of exposure. The narrow width of the burn mark is consistent with the angular power density from fig. 6.4a.

One important result to note is the absence of an inherent beam helicity dependent effect. While the emitted photon can be polarized, and is related to the angle ψ , the actual helicity of the electron is not a direct factor into the calculations.

Scattering from Residual Gas in the Beam Pipe

The low photon energies of Synchrotron radiation incident on the photon detector cannot account for the distribution of background energies seen experimentally, as seen on fig. 6.18.

Another potential source of backgrounds could be due to the electron beam scat-

tering off any residual gas in the beamline. Though, since the beamline is maintained at vacuums below 100 nTorr, we would expect this effect to be small.

To quantify the effect, I performed a Monte Carlo simulation with Geant4[78–80]. The simulation was kept simple, where 5,000,000 electrons were simulated passing through the beam pipe filled with 1 atm of air. The low probability of scattering at pressures μ Torr scale would require a significant number of electrons to be simulated and so to speed up the simulation the pressure was kept at 1 atm and later scaled to three different pressures shown in fig. 6.6a. The third and fourth dipole

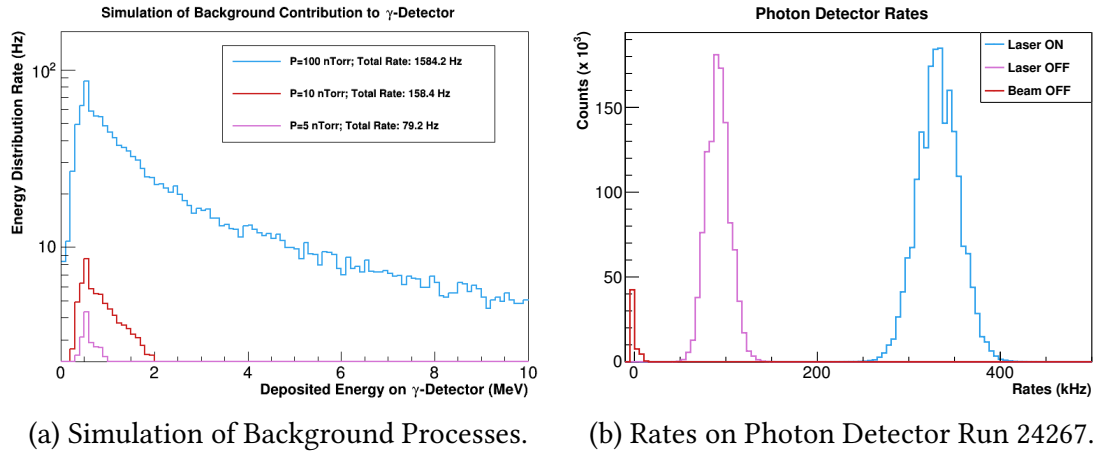


Figure 6.6: Figures showing the rates of particles incident on the photon detector. A simulation of the electron beam interacting with the residual gas in the beam pipe is shown on the left. Shown on the right are the rates seen in run 24267. The simulated rates are not sufficient to explain the background rates seen in run 24267.

were simulated as simple rectangular volumes of 3 cm width in the horizontal direction, and 22 cm height in the vertical direction. The length of the volume in the beam direction was 156 cm to accommodate the entire magnetic field map. The first and second dipole were not included in the simulation. The electrons were shot from the interaction point with an energy of 1.16 GeV and a momentum direction entirely in

the $+z$ direction in the Q_{weak} coordinate frame. The electrons were tracked through the dipole at 1 mm steps, though were not recorded on disk.

The total deposited energy on the four PbWO_4 crystals was recorded per simulated electron. The energy was binned into the histogram shown on fig. 6.6a, where the horizontal axis corresponds to energy deposited on the crystals. In order to convert the content of each bin from a count to a rate of energy deposited for the corresponding bin-energy by scaling by a factor given by

$$R = \frac{I_{\text{beam}}}{e \times N_e^{\text{simulation}}} \times \frac{P_{\text{beamline}}}{P_{\text{simulation}}}, \quad (6.14)$$

where I_{beam} is the beam current of $180 \mu\text{A}$, e is the electron's charge, $N_e^{\text{simulation}}$ is the number of simulated electrons, and lastly P_{beamline} and $P_{\text{simulation}}$ are the pressures of the beamline and the simulation, respectively. In order to compare to data all the rates were summed to get a total rate of incident particles on the photon detector.

The rates of run 24267 are shown in fig. 6.6b in which we can see that the background rates, as measured when the laser is unlocked, are of the order of 100 kHz. However, the simulation shows total rates of at most 1.5 kHz at a worst case scenario when the beamline vacuum is poor at 100 nTorr.

Beam Halo

If neither synchrotron radiation nor scattering off residual gas in the beamline can explain the backgrounds seen in the photon detector, then the last remaining explanation must come from the extremities of the beam profile. While the width of the electron beam is $<200 \mu\text{m}$, there can be sufficient number of electrons at large enough extremities where they interact with any of the beamline. Furthermore,

dispersion through bending magnets could give the beam a “tail” of unknown characteristics. These extremities are often referred to as the beam “halo.” The properties of the halo itself were unmeasured, but is known to exist from dedicated measurements for the Q_{weak} experiment.

It is very difficult to model the beam halo without dedicated measurements, and hence neither a model or simulation will be presented in this thesis. Instead, a discussion about correcting for background in general follows.

Correcting for Background

Now that two likely candidates have been identified as possible sources of background, let us move towards understanding the effect on the asymmetry and then to deriving a method to subtract the effects of background.

To quantitatively understand the effect of background, start by expanding on eq. (6.3) and explicitly write $Y = Y_{e\gamma} + Y_B$ where $Y_{e\gamma}$ is the real integrated signal from Compton scattered photons off the laser and Y_B is any background signal from other sources. This means that any uncorrected (raw) asymmetry measured is really written as

$$A_{msr} = \frac{(Y_{e\gamma}^+ + Y_B^+) - (Y_{e\gamma}^- - Y_B^-)}{(Y_{e\gamma}^+ + Y_B^+) + (Y_{e\gamma}^- + Y_B^-)}, \quad (6.15)$$

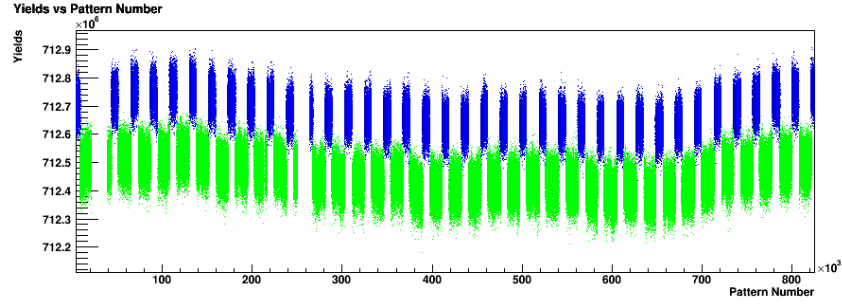
where if we assume that the background is to first order helicity independent, we can approximate the background yield as $Y_B \approx Y_B^+ + Y_B^-$ and by that same notion the background difference is negligible $\Delta Y_B \approx \Delta Y_B^+ - \Delta Y_B^- \approx 0$, which gives the simplified form

$$A_{msr} = \frac{\Delta Y_{e\gamma}}{Y_{e\gamma} + 2Y_B}. \quad (6.16)$$

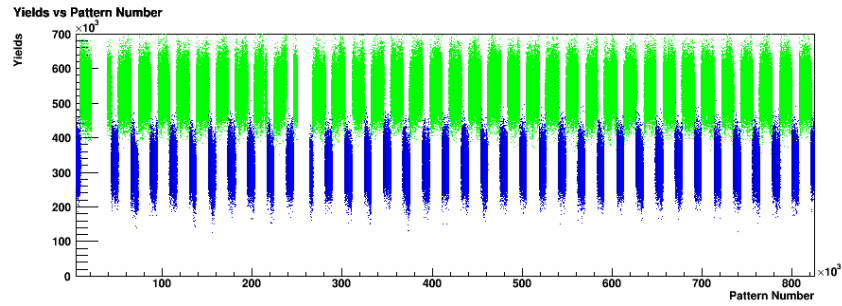
In this form we see that the background signals are actually amplified, contributing an effect of twice their yield into the measured asymmetry. It is also evident that for any nonzero background the measured asymmetry is actually smaller than the real physical asymmetry ($A_{msr} < A_{ey}$).

Fortunately, beam line backgrounds are directly measurable by removing the photon target, namely turning off the laser, and taking dedicated measurements of the yields. Recalling from section 5.2.1 where a flipper mirror allowed us to remove the power inside the laser cavity, which in essence allowed us to periodically remove our photon target. This periodic removal of the photon target was performed for every run throughout the experiment. This allowed us to make more direct time-based background measurements as close as possible to the actual physics measurement. We can see an illustration of these background measurements in fig. 6.7b, where the green region represents the signal when the cavity is locked and the blue represent the signal when the cavity is unlocked.

To minimize the effect of slow changes in the beam line background, the asymmetry is determined around each cycle of laser on and off. The measurements are divided in “laser patterns” defined as a laser on measurement “sandwiched” by two laser periods on either side. The laser off period is further divided in half with each asymmetry having a unique background measurement independent of the others. Quantitatively this means that for a given n -th laser pattern, we can write t_{off}^n to represent the time at which the laser is turned off and likewise t_{on}^n represents the time at which the laser is turned on for this cycle. Then the background measurement for an asymmetry A_{msr}^n is the laser off period from $(t_{\text{off}}^n + t_{\text{on}}^n)/2$ to t_{on}^n and t_{off}^{n+1} to $(t_{\text{off}}^{n+1} + t_{\text{on}}^{n+1})/2$. The corresponding beam current normalized background measure-



(a) Accum0 yields with no corrections applied but with quality cuts applied.



(b) Accum0 yields with pedestal corrections and quality cuts applied.

Figure 6.7: An example of the Accum0 yields in units of integrated adc values. The top image shows the yields without pedestal corrections applied. The bottom image shows the yields after pedestal corrections were applied. Both images have quality cuts applied which are evident by the gaps in the data. The horizontal axis corresponds to a unit of time.

ments for these two periods are then $\langle Y_{\text{left,off}}^n \rangle$ and $\langle Y_{\text{right,off}}^n \rangle$ respectively, with $\langle Y_{\text{off}}^n \rangle$ being the current normalized average of the two periods.

We can now determine the average real (physics) signal of the Compton scattered photons for each laser pattern by directly subtracting the average background contribution for this period as

$$\langle Y_{e\gamma}^n \rangle = \langle Y_{\text{on}}^n \rangle - \langle Y_{\text{off}}^n \rangle. \quad (6.17)$$

With this result we can now construct the real beamline background corrected

physics asymmetry for each n-th laser pattern as

$$\langle A_{e\gamma}^n \rangle = \frac{\langle \Delta Y_{e\gamma}^n \rangle}{\langle Y_{e\gamma}^n \rangle} = \frac{\langle \Delta Y_{\text{on}}^n \rangle}{\langle Y_{\text{on}}^n \rangle - \langle Y_{\text{off}}^n \rangle}. \quad (6.18)$$

The process to determine the laser patterns is fully automated by an algorithm that looks for stable periods of “on” and “off” laser cycles and divides them into patterns as needed.

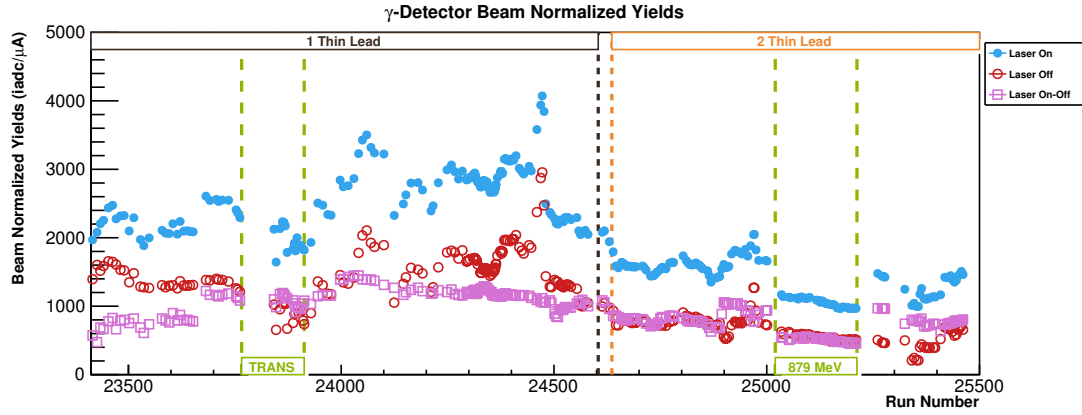


Figure 6.8: Shown here are the beam normalized slug averaged pedestal corrected yields (in units of integrated ADC channels per μA). The blue close circles correspond to the laser-on periods with no background subtraction. The red open circles are the laser off periods averaged by either side of the corresponding laser-on period. The pink closed squares correspond to the background subtracted real Compton scattered yields.

In fig. 6.8 I show the beam current normalized pedestal corrected yields for a subset of the Run II running period from January 27 to May 15 2012. The pedestal correction will be introduced and discussed in the next section. The squares represent the background subtracted yields, corresponding to the physical Compton scattered photons. The current normalization should remove any dependence on the beam current. However, the rates are still dependent on the intensity of the

Fabry-Pérot cavity. There is also a slight dependence on the shielding placed in front of the detector, which was used to minimize contributions of synchrotron radiation. As a systematic test of the effects of synchrotron radiation, three different configurations of shielding were used corresponding to either no shielding, 1 piece of ~ 2 mm thin lead placed in front of the detector, or two pieces of thin lead. In fig. 6.8 the corresponding periods of one or two pieces of thin lead shielding are highlighted, where any region outside of this contains no shielding in front of the detector. The resulting signals are slightly affected by the choice of shielding.

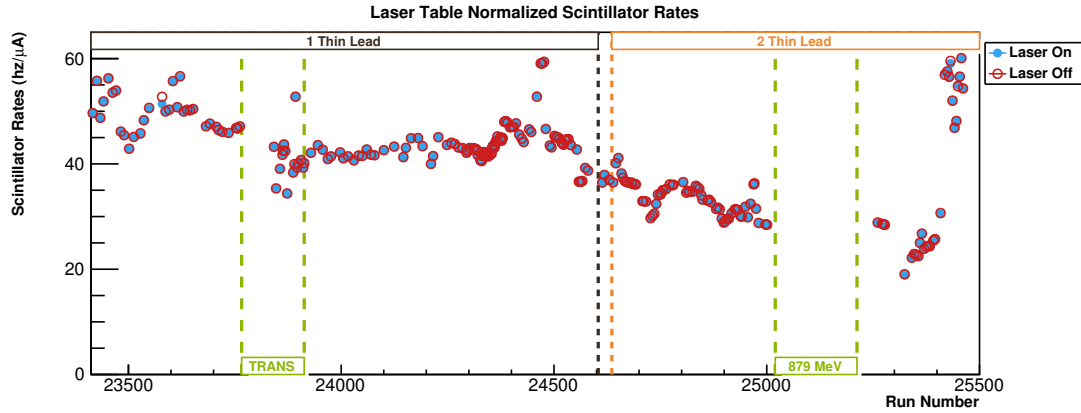


Figure 6.9: The rates seen by the “background” scintillator averaged by slug. No significant differences seen between the laser-on states and the laser off states, confirming that this scintillator only sees background signal. The running period with a beam energy of 879 MeV are not shown.

We can compare the background signal in fig. 6.8 with the rates seen in a scintillator at the laser table. The scintillator was installed to monitor the relative radiation levels seen by the laser optics, particularly, the beam downstream mirror of the Fabry-Pérot cavity. For the same period as the yields in fig. 6.8 I show the corresponding beam current normalized rates seen by the scintillators in fig. 6.9. Of particular importance is that the scintillators does not see the Compton scattered

particles by evidence of the excellent agreement between the two laser states. Another important comparison is that it sees and explains the sudden jumps seen in signal on the photon detector. For example the drastic jump in signal seen around run 24460 of fig. 6.8 is also seen by the scintillator in fig. 6.9. The last point to make is that the scintillator rates allows us to directly observe the effect of shielding on the photon detector. The rates seen by the scintillator for runs 24550 to 24675 are fairly consistent, with only a small excursion. Meanwhile the photon detector yields dropped by $\sim 20\%$ as a consequence of switching from using just one piece of thin lead for shielding to using two.

6.1.4 Determining and Correcting for Pedestal

The next step was to properly calibrate the Accumulator 0 values. However, since the end goal was to determine a unit-less asymmetry, calibration from the internal ADC channel reading to V was not needed we set $f = -1$. The negative multiplier is needed since a smaller number reported by the FADC actually corresponds to a larger signal. The next step was to determine an Accumulator 0 pedestal and understand its behavior as a function of time. In fig. 6.7a we can see the integrated signals as a function of time, and we clearly see a time dependent rate. To understand if this can be attributed to a pedestal shift we devised a technique to monitor the change on a smaller time scale.

Recalling from section 5.3.3 that 256 contiguous samples were taken as often as once or more times per helicity window. The triggered photon was centered at the window and this left ~ 110 channels prior to the pulse possibly empty as seen on fig. 6.10a. The average of this region will tell us the pedestal for that window to a

precision of ± 1 channel. This precision is not enough, so we averaged out this measurement across a larger time scale, choosing the same length as the measurement described in the previous section.

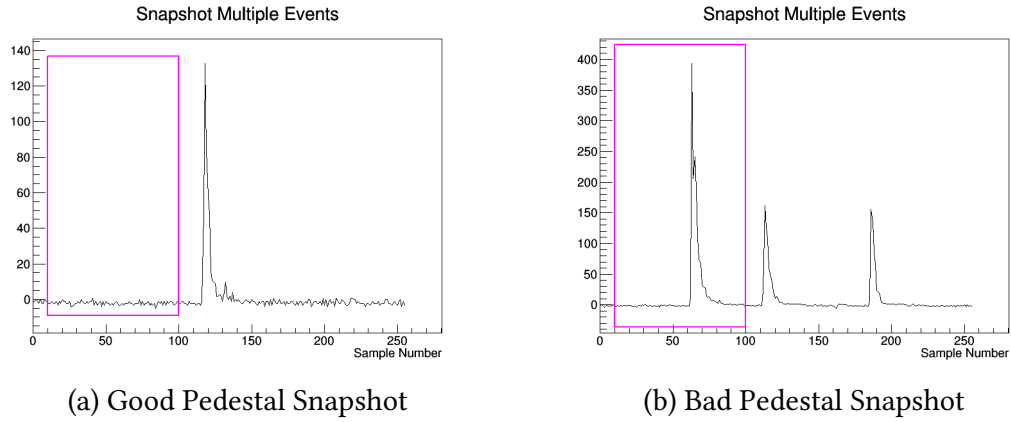


Figure 6.10: An illustration of two full snapshots containing 256 contiguous samples, where the main photon trigger is seen around sample 115 and the magenta box highlights the region used to determine the pedestal. The figure to the right shows a good clean single photon event useful for the pedestal determination, while the one on the right shows multiple photon events, one of which is in the pedestal region and must be discarded.

However, we could not rely on these 110 channels to always be empty, as the probability of a photon appearing in this time window is proportional to the total event rate. Figure 6.10b shows a window with multiple photons, including one photon larger than the triggering photon in the first 110 channels. A simple algorithm was developed that looked at the average value of channels 0 to 100 determined the standard deviation (σ) and discarded the window if any channel that was larger than 3σ . While this requirement threw away less than 0.3 % of false positives it also ensured that less than the same amount of photon signals were mistakenly allowed in the region. To avoid missing the tails of photons coming in slightly before the snapshot window and also avoid being biased by the photon in the center of the

window, the pedestal was determined from the average of channels 10 to 100.

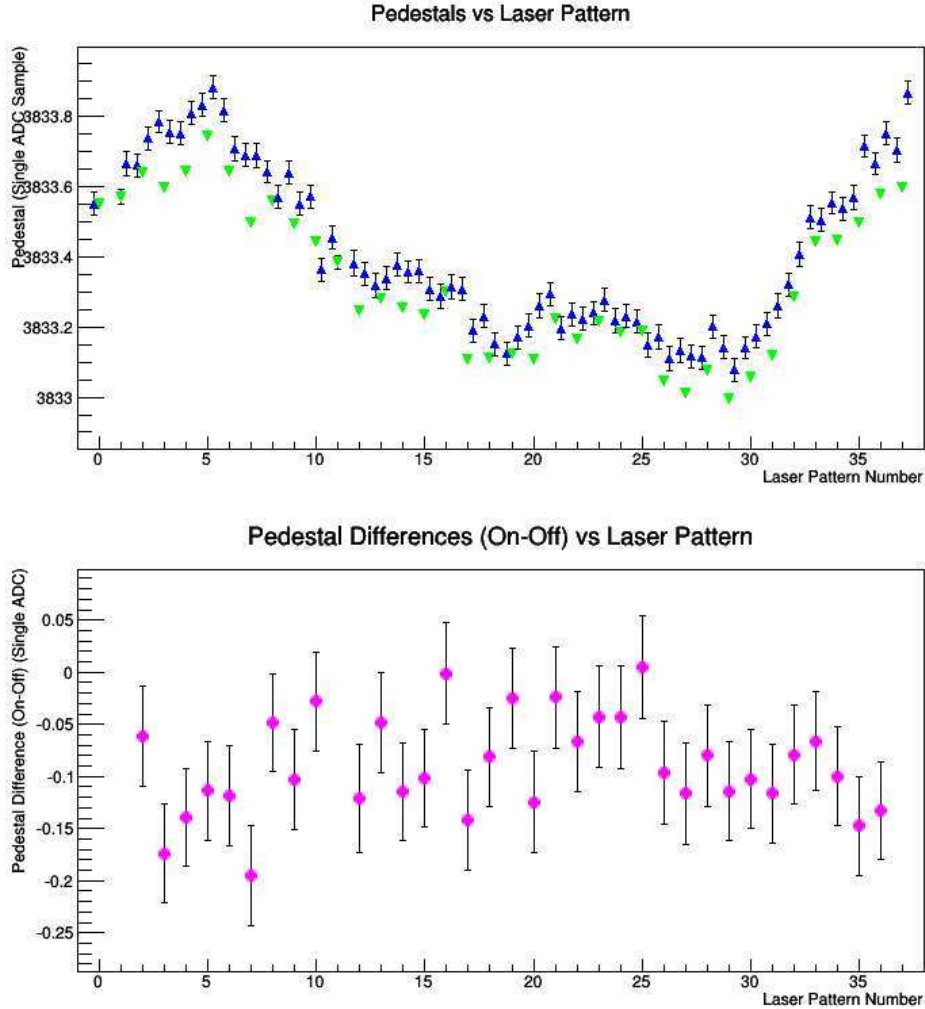


Figure 6.11: Pedestals vs time for run 24267. Each point corresponds to the average of the first 100 samples for all snapshots in a given laser state.

This study not only found a time dependent pedestal rate, but also accounted for a suspected pedestal shift between laser-on and laser-off states, which is critical for the background subtraction. Figure 6.11 we can see the time dependence and the measurable laser-on-off pedestal difference. This finding is not surprising, and can

be attributed to a rate dependent baseline shift. In fig. 6.11 the average difference is negative, which is due to the fact that the zero value of Accumulator 0 is for a high of 4 V at channel 4096. So a smaller number in this graph points to a smaller pedestal deviation from channel 4096. The rate dependence may be worrisome, as the Accum0 differences of eq. (6.18) are, by its nature, rate differences. Determining them directly using the methods described above, and subsequently correcting the Accum0 differences, was not desirable. The error on the pedestal determination for the helicity correlated differences was too large. I will instead place an upper limit on the differences. Taking rough numbers from fig. 6.11 we see the average pedestal difference between laser on and off is ~ 0.1 which corresponds to a 0.003 % difference out of the entire pedestal. This is already looking largely insignificant, and is even more so considering the difference in rates from fig. 6.7 is on the order of ~ 150 %. If we expect an asymmetry of ~ 2 % then the helicity correlated pedestal differences is already $< 1 \times 10^{-6}$ %.

Applying these corrections to the measured integrated signals of Accumulator 0 removed the visible time dependence rate shown on fig. 6.7b. Additionally we see that now the laser-on yields are larger than the laser-off yields, as would be expected. The reason for laser off yields to seemingly be larger is because the signals are compared to the true baseline at channel 4096 when no true pedestal correction is applied. We could have negated this effect by applying an initial global pedestal correction of 4096 and or applying the gain correction of -1 mV/adC, but would have been made obsolete when the true pedestals were determined.

In fig. 6.12 I show the determined pedestals for the Run II data from January 27 to May 15, 2012. The two ADC channel difference between the relatively stable run-

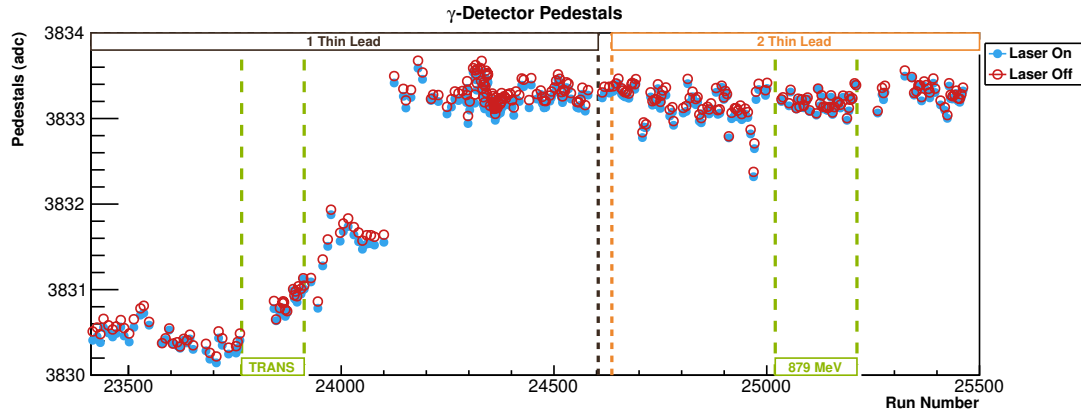


Figure 6.12: Run II pedestals from January 27 to May 15, 2012 and averaged by slug. The cause of drastic change in pedestal from the earlier running period (before run 24150) compared to the later periods is not known.

ning periods for runs before 23800 and after 24150 corresponds to a baseline shift of just ~ 2 mV. The cause for the gradual drop in pedestal seen between runs 23800 and 24150 is also unknown. While many factors may influence the pedestal, such as rate, one likely cause may be the temperature of the modules in the Compton DAQ. This is evident during a several hour period where the AC unit in the electronics malfunctioned. During this period we observed a ~ 2 mV baseline shift that quickly recovered once the AC unit was fixed as seen on fig. B.3 in the Appendix. Another possible source of pedestal drift could be the un-monitored temperature of the photon detector.

6.1.5 Measured Asymmetries

The data presented in this section are all averaged into groups of ~ 30 runs. The averaging was performed using an error weighted average. Since the sign of the helicity differences and asymmetries are dependent on the IWHF state (IN or OUT),

the Wien angle setting and the laser polarization. In order to properly average them together, the sign had to be corrected by using the convention

$$\text{sign}(\text{IHP}) = \begin{cases} +1 & \text{for IHP inserted} \\ -1 & \text{for IHP not-inserted} \end{cases}, \quad (6.19)$$

$$\text{sign}(\text{wien}) = \begin{cases} +1 & \text{for } \phi_{\text{wien}} > 0 \\ -1 & \text{for } \phi_{\text{wien}} < 0 \end{cases}, \quad (6.20)$$

$$\text{sign}(\text{laser}) = \begin{cases} +1 & \text{for laser right circularly polarized} \\ -1 & \text{for laser left circularly polarized} \end{cases}. \quad (6.21)$$

This applies only to quantities which are expected to flip with the sign of the helicity. Values such as yields and rates are not sign corrected.

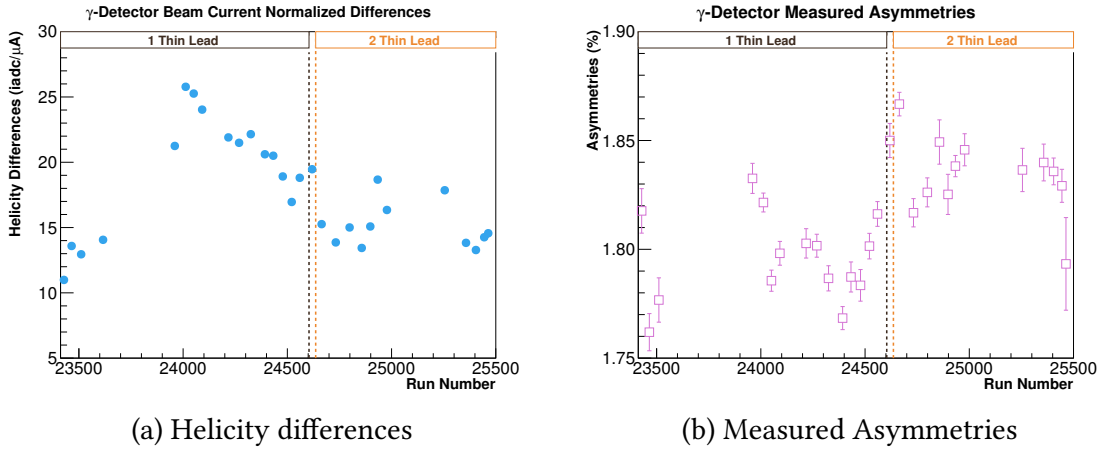


Figure 6.13: Shown here are the Run II helicity differences and the asymmetries, averaged into groups of ~ 30 runs. Only statistical errors shown.

In fig. 6.8 we see the beam current normalized background subtracted yields. The corresponding helicity differences, now grouped and averaged into groups of ~ 30 runs, are shown in fig. 6.13a. The transverse polarization and the low energy 879 MeV periods were excluded. The asymmetries, grouped in the same fashion, are shown in fig. 6.13b. Only the statistical errors were shown. The average statistical error for these groups is 0.42 %. We can easily see that the relative error of the helicity differences dominates the measurement by comparing the width of the distribution of the yields (fig. 6.14a) to those of the helicity differences (fig. 6.14b) for run 24846. Though the widths are fairly similar, by dividing by the mean we get the relative error of both.

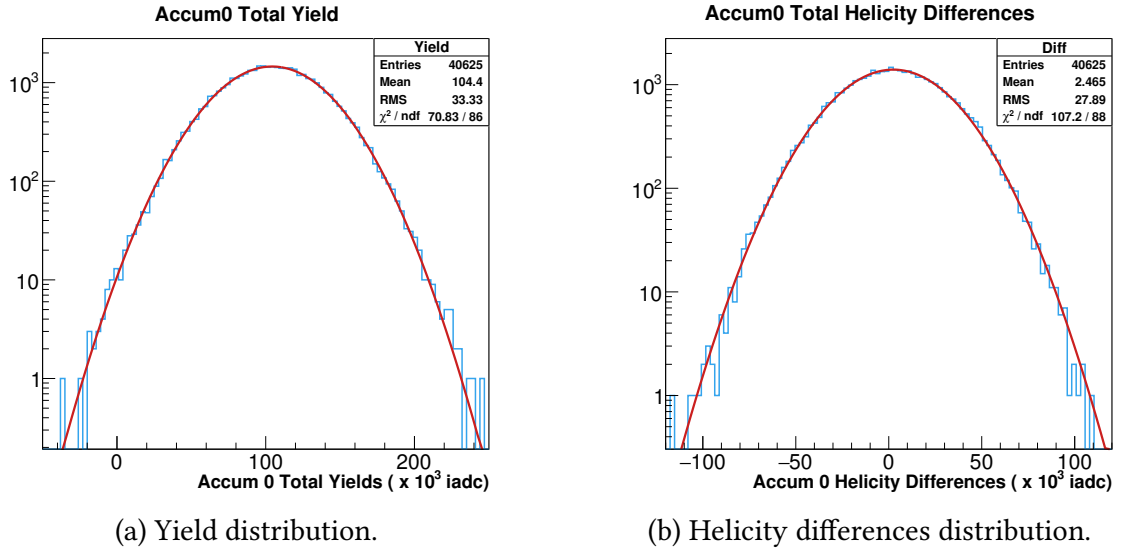


Figure 6.14: The average Accum0 yield (left) and helicity difference (right) per helicity quartet for run 24846 in units of integrated adc channels. The laser off data was removed from these histograms. No other corrections were applied for pedestal nor were the background contributions subtracted out. This run was 96 minutes long.

6.1.6 Corrections to the Asymmetry and Errors

Background Asymmetries

The asymmetry, if any, of the background signal has been ignored up until this point. We could have re-written eq. (6.18) to account for these background asymmetries, however, the higher statistical errors on the background asymmetries would add arbitrary noise to the measured Compton scattering asymmetry. Furthermore, the background differences are relatively small as evident on fig. 6.15a and even more evident by looking at the asymmetries show in in fig. 6.15b. The jump seen starting around run 24600 is particularly troublesome. This is believed to be associated with the $\sim 0.5\%$ of laser power still in the cavity as a result of the flipper mirror no longer being used.

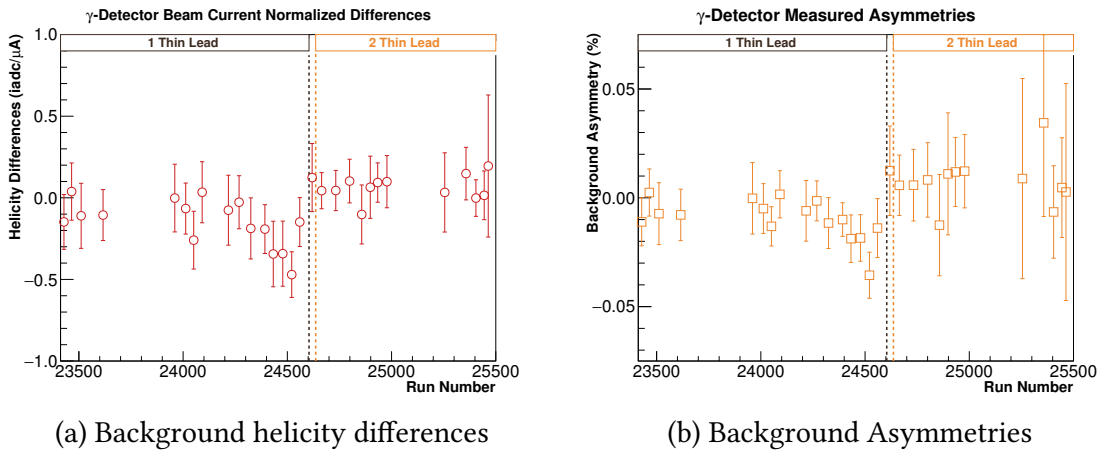


Figure 6.15: Shown here are the background helicity differences and the asymmetries, averaged into groups of ~ 30 runs. Only statistical errors shown.

We cannot simply subtract out these differences from the Compton scattering asymmetry, as these differences may correspond to real Compton scattered events. Likewise, adding it also poses a problem because a portion of these differences may

actually correspond to non Compton scattered events. I will instead simply add it as a systematic error for this period. The average difference measured is 0.04 iadc/ μ A to 0.01 iadc/ μ A, which corresponds to 0.5 % to 0.6 % of the Compton scattering helicity difference. Comparing this value to the measured asymmetry we find this contributes a 0.52 % error to the measured asymmetry.

6.1.7 Sensitivity to Beam Properties

The sensitivity of the measured asymmetries to the beam properties was also studied. This was done by plotting the asymmetries as a function of a specific beam property x_i . Then the sensitivity is defined as

$$\text{Slope} = \frac{\partial A_{ye}}{\partial x_i}. \quad (6.22)$$

Since we normalized to the beam current we would expect most of the sensitivity to changes in the beam current to be removed. In the end there was a residual slope of only $9.314\,36 \times 10^{-4} \mu\text{A}/\%$. Given that the average asymmetry measured is 1.8 % and the current is stable within the 1.78 μA of fig. 6.1b, then we can place an upper limit on the error of 0.18 % with a 95 % confidence level. Similarly the combined effect of any beam position or beam current helicity correlated differences is placed at an upper limit of 0.07 % with a 95 % confidence level.

Sensitivity to the absolute beam position produced larger errors overall. This was due to the fact that about one third of the laser patterns showed the beam moved by up to 240 μm , instead of the less than 100 μm motion of the remaining patterns. This can be corrected with tighter restrictions on the quality of the data. However, this

has the consequence of increasing the statistical error. The vertical position leads the sensitivity by changing the asymmetry by $10 \text{ } \mu\text{m}$ in beam vertical motion and contributes a 0.32 % uncertainty on the asymmetry. Overall the position sensitivities provide a maximum of 0.40 % relative error to the measured asymmetry.

Propagation of Uncertainties

The propagation of uncertainties for the measured helicity is pretty straight forward and can be approximated as

$$\delta(A_{e\gamma})^2 \approx \sum_i \left(\sigma_i \frac{\partial A_{e\gamma}}{\partial x_i} \right)^2, \quad (6.23)$$

where σ_i is the variance of the measurement x_i . To prove this, we first expand eq. (6.18) and write all the terms explicitly to get

$$\langle A_{e\gamma}^n \rangle = \frac{\langle \Delta Y_{\text{on}}^n \rangle / \langle I_{\text{on}}^n \rangle}{\frac{\langle Y_{\text{on}}^n \rangle - \langle P_{\text{on}}^n \rangle}{\langle I_{\text{on}}^n \rangle} - \frac{1}{2} \left[\frac{\langle Y_{\text{left,off}}^n \rangle - \langle P_{\text{left,off}}^n \rangle}{\langle I_{\text{left,off}}^n \rangle} + \frac{\langle Y_{\text{right,off}}^n \rangle - \langle P_{\text{right,off}}^n \rangle}{\langle I_{\text{right,off}}^n \rangle} \right]}. \quad (6.24)$$

The laser on terms were taken at different times than the laser off terms, and so their contributions are uncorrelated. Equally the pedestal determinations correspond to a different subset of the data, and are also uncorrelated with the other terms. The other remaining terms that may be correlated with each other are the beam current measurements and the yield and helicity level differences, respectively. However, as it turns out those terms are also driven mostly by their own independent statistical distributions and are entirely uncorrelated. We can see an example of the lack of correlation between the yields and the corresponding helicity differences in fig. 6.16.

Hence, in formulating eq. (6.23) I simply dropped all the covariant terms, or more explicitly we can write the covariant terms by using the Kronecker-Delta piecewise function and write $\sigma_i \sigma_j = \delta_{i,j}$.

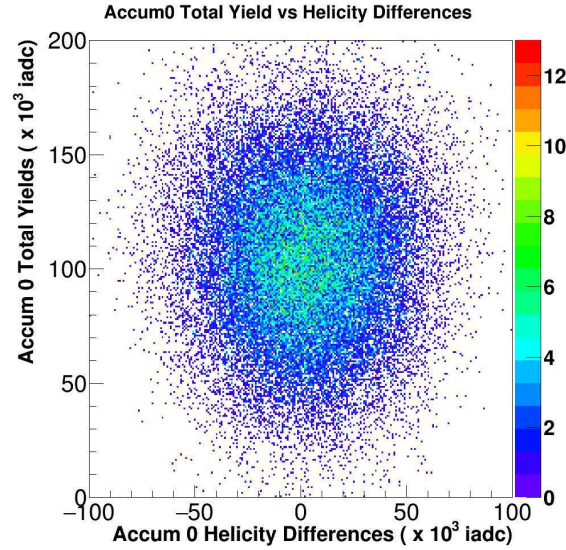


Figure 6.16: Showing the correlation of the Accum0 yields vs helicity differences for run 24846. No corrections for pedestal or background subtraction have been applied. There is no correlation between the two and so the variations can be treated as uncorrelated.

6.2 Determining the Analyzing Power

While the analyzing power is dependent on the theoretical asymmetry, it has to encompass more than just the asymmetry. A simple definition of the analyzing power would be the theoretical asymmetry measured by a polarimeter if the electron beam and laser were 100 % polarized and any detector offsets, asymmetries, efficiencies and non-linearity were taken into account. Lets begin by relating the analyzing

power to the properties of discrete events as

$$A_{th} = \frac{\sum_i \rho_i \epsilon(\rho_i) A_l(\rho_i) S(\rho_i)}{\sum_i \rho_i \epsilon(\rho_i) S(\rho_i)}, \quad (6.25)$$

where ρ_i is the unit-less fractional energy of the scattered photon given in eq. (5.10), and $A_l(\rho_i)$ its corresponding theoretical asymmetry, the detector efficiency and linearity are combined in $\epsilon(\rho_i)$ and lastly the response of the detector is quantified as $S(\rho_i)$. We can get the theoretical asymmetry from eq. (5.18) and the linearity must be determined from measurements of the detector (described later). This will be determined from a Monte Carlo simulation, which I will discuss next.

6.2.1 Monte Carlo Simulation

A special Monte Carlo simulation package was built using the Geant4 framework [78–80] and modeled on the dissertation work of Megan Friend[23]. The basic principle of the Monte Carlo was built around randomly selecting the starting kinematics of a Compton scattered photon and “shoot” it towards the detector. The first generated particle is referred to as the Primary particle, and Geant4 uses different random number distributions to simulate the trajectory and subsequent interactions. A series of built in, or user supplied, functions calculates the probabilities of scattering, production of “secondary” particles or absorption into a material. We repeat the process a total of N times where N is chosen to be sufficiently large to reduce the statistical error on the simulation.

In this simulation each event starts by selecting a ρ defined in eq. (5.10) sampled from a distribution of the differential un-polarized cross section of eq. (5.12). This ρ

was then converted to an absolute photon energy by using eqs. (5.7), (5.8) and (5.10). The polar scattering angle θ is determined from eq. (5.10) and the azimuthal angle is sampled from a uniform distribution from 0 rad to 2π rad. Only the photon was simulated and the corresponding scattered electron was not used in this simulation.

As the scattered photon was simulated, we used the feature of Geant4 to record the total energy deposited on the four PbWO_4 crystals as the first estimate of the simulated “signal” on the PMT. After $N \approx 1$ million events were simulated, the spectra of deposited energies were then compared to integrals of the pulses on the snapshot data used in the pedestal determination. As expected, this simple model was inadequate to properly match the snapshot data, and a more detailed simulation was required.

In lieu of relying on deposited energy alone, the software was modified to produce and fully track the optical transport of light in the crystals up to the point of detection by the PMT cathode. The characteristics and simulation of these optical properties makes use of special photons defined in the scope of Geant4 as optical photons. These optical photons are defined photons whose wavelength is much larger than the typical separation of atoms in a material[80], i.e. $\lambda \geq 300$ nm. At these wavelengths Geant4 uses the continuous wave-like nature of light to determine reflections, transmissions and “splitting” of light at the boundary of two mediums.

In order for Geant4 to be able to simulated these special optical photons, the optical properties of each material, for which tracking is to be performed, must be specified. At minimum the real component of the index of refraction is required which will be used to calculate the scattered angles at the boundaries using Snell’s

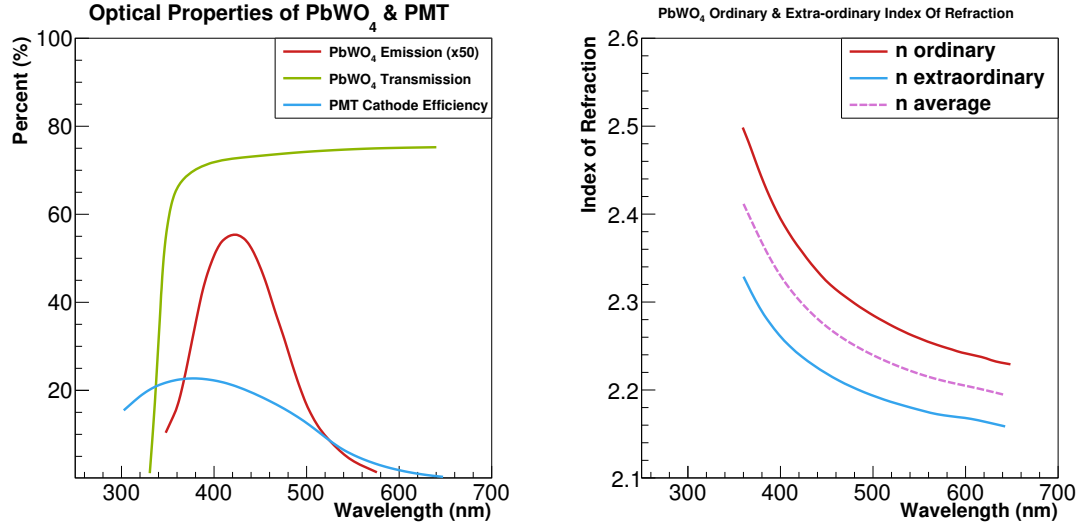


Figure 6.17: Optical properties of the PbWO₄ crystal showing the emission, transmission spectra [81] and the efficiency of the Hamamatsu PMT[65] (left). The integral of the emission spectrum has been normalized to 100 % and for display purposes were multiplied by 50 in this graph. The index of refraction averaged over the ordinary and extraordinary components from[82] (right).

law. However, the user may elect to also supply the transmission and reflective properties of the medium. The optical properties of PbWO₄ are shown in fig. 6.17 as extracted from [81] and [82] using WebPlotDigitizer[83], a web based application for digitizing plots. The index of refraction of PbWO₄ are dependent on the orientation of the crystal lattice[82] and since the orientation of our crystals are unknown, I applied the average of the two as input to the simulation.

The production optical photons in Geant4 is determined via two physical processes. The first is the use of Cherenkov radiation and the second is to use the scintillating nature of a material. The details of both will individually be discussed in the next two sub-sections.

Photon Emission due to Cherenkov Radiation

Cherenkov radiation is emitted in a medium in which the particle's velocity is greater than the local phase velocity[6]. The total number of emitted photons for a given step length in the Geant4 Monte Carlo method is given as[80]

$$\frac{dN}{dx} = \left(\frac{\alpha Z^2}{\hbar c} \right) \int_{\varepsilon_{\min}}^{\varepsilon_{\max}} d\varepsilon \left(1 - \frac{1}{n^2(\varepsilon)\beta^2} \right) = \left(\frac{\alpha Z^2}{\hbar c} \right) \left[(\varepsilon_{\max} - \varepsilon_{\min}) - \frac{1}{\beta^2} \int_{\varepsilon_{\min}}^{\varepsilon_{\max}} \frac{d\varepsilon}{n^2(\varepsilon)} \right], \quad (6.26)$$

where $\alpha/\hbar c \sim 370$, n is the index of refraction of the medium, z the net atomic number, and ε_{\max} (ε_{\min}) are the maximum (minimum) possible emitted photon energies as defined by the input optical properties of the medium. The emitted photons are radiated at an angle with respect to the direction of the particle given by[6, 80] as $\cos \theta = (n\beta)^{-1}$. For the case of PbWO_4 with the indices's of refraction given by fig. 6.17 the narrow cone of emission is bounded by the range of θ such that $63.1^\circ \leq \theta \leq 65.6^\circ$. The average number of emitted photons produced by Geant4 is calculated by a Poisson distribution where the mean is given by $\langle n \rangle = LdN/dx$, where L is the given step length. The final step is to determine the energy distribution of the emitted photons by sampling over the density function[80]

$$f(\varepsilon) = 1 - \frac{1}{n^2(\varepsilon)\beta^2}. \quad (6.27)$$

This process is fixed by Geant4 and the only property which influences the process is the specified index of refraction as a function of photon energy. Geant4 also sets the polarization vector of the emitted photons in the same direction as the emitted photon's velocity vector. The effects, if any, due to this polarization were unstud-

ied for this dissertation but are believed to be insignificant as no other polarization sensitive process was included in the simulation.

Photon Emission due to Scintillation

Unlike the case for Cherenkov Radiation, there is no built in method in Geant4 that determines the absolute scale of Scintillated photons produced by a particle interacting in the medium. The user is responsible for supplying this necessary information, and Geant4 will use this input to simulate the emission of photons due to scintillation.

The true light yield of our four specific PbWO_4 crystals were unmeasured, and instead we relied on the reported relative light output from literature. The relative light yield of PbWO_4 is reported to be on average 0.377 % of that of NaI[6, 81]. A good NaI crystal produces upwards of 40,000 photons/MeV of energy deposited on the crystals, which means we can estimate that our PbWO_4 crystals produce on average of 150.8 photons/MeV. In the case of PbWO_4 , the total yield is temperature dependent and increases by $\sim 2 \text{ \%}/^\circ\text{C}$ cooled below room temperature[81]. As described in section 5.2.3 the crystals were cooled down 10°C from room temperature, which provides a gain of 20 %. The average light yield of the cooled PbWO_4 crystals is expected to be ~ 181 photons/MeV.

In the simulation, the average light yield ($\langle Y_p \rangle$) is used by Geant4 to randomly determine a total number of optical photons N_γ to simulate as a response of a particle (p) depositing net energy ΔE_p in a scintillating material. First the mean number of photons is computed as[80]

$$\langle N_{\text{optical}} \rangle = \Delta E_p \langle Y_p \rangle. \quad (6.28)$$

Different particles can have a different corresponding average light yields, however, for a photon, the leading production of scintillating light is due to electron-positron pair production[23], we set $\langle Y_p \rangle = 181$ photons/MeV as determined above.

The next step is to determine N_γ by one of two statistical distributions. For cases when the incident particle deposited a small amount of energy such that $\langle N_{\text{optical}} \rangle \leq 10$, Geant4 determines N_γ by sampling from a Poisson distribution with mean value $\langle N_{\text{optical}} \rangle$ ¹. For larger energies Geant4 samples from a Gaussian distribution $G(\bar{\mu}, \sigma)$, where $\bar{\mu} = \langle N_{\text{optical}} \rangle$ is the mean of the distribution and the standard deviation is given by $\sigma = \sigma_\alpha \sqrt{\langle N_{\text{optical}} \rangle}$. In the last equation σ_α represents the resolution of the material, in which case 30 % was used to match the resolution of PbWO₄.

The direction and energy of each of the N_γ simulated optical photons are also determined. The direction is determined from a solid angle which is sampled uniformly from 0 to 4π sr. The corresponding energies were sampled from the emission spectrum shown in fig. 6.17 and the integral of the emission spectrum was normalized to 100 %.

An optional feature of Geant4 is to keep track of the realistic time it takes for particles to be transported across the detector. The emission of optical photons in a medium can be modeled as the linear combination of exponentially decaying functions of the form[80]

$$T(t') = \sum_i T_i(t') = \sum_i R_i \left(\frac{\tau_{ri} + \tau_{ci}}{\tau_{ci}^2} \right) e^{\frac{-t'}{\tau_{ci}}}, \quad (6.29)$$

where τ_{ri} is the time it takes for the process to reach peak light output, known as the

¹This restriction is hard-coded into the Geant4 and can only be changed by modifying the source code of the Geant4 toolkit.

rise time, t_{ci} is the time constant of the function T_i . R_i is the normalized fractional yield such that $\sum_i R_i = 1$.

Up to two time constants may be specified, a fast τ_{cf} with rise time τ_{rf} and a slower time constant τ_{cs} with rise time τ_{rs} . For PbWO_4 the time constants are $\tau_{cf} = 5 \text{ ns}$ and $\tau_{cs} = 30 \text{ ns}$, with corresponding fractional yields $R_f = 20.4 \%$ and $R_s = 79.6 \%$, respectively[6]. The rise time of both components were set to zero for this simulation. Including this time proved crucial to the commissioning of the simulation by comparing against real data. For completion, it should be noted that the Cherenkov radiation is emitted instantaneously in the simulation.

Modeling the PMT Signal

An energy calibration of the photon detector was unavailable, and the signal on the photon detector was measured in terms of integrated samples of the voltage of the PMT anode. We need a model for the PMT in order to validate the simulation by comparison to the real data. This was done by estimating the voltage induced by a single optical photon being “detected” by the cathode in the PMT. The term detected in this case means an optical photon that is both absorbed by the cathode and subsequently causes an electron to be emitted. The probability of an absorbed photon emitting an electron is driven by the quantum efficiency of the cathode. For our chosen Hamamatsu PMT the maximum efficiency is 22 % as shown in fig. 6.17 and taken from the manufacturer’s specifications[65]. Since the efficiency is also dependent on the incident photon’s energy, one has to be careful to match the properties of the detector to lie within the efficiency of the PMT’s cathode.

$$V_0^{\text{sim}} = e (k_{\text{PMT}}) (k_{\text{DAQ}}) N_s f_{\text{ADC}}, \quad (6.30)$$

where e is the charge of the electron, k_{PMT} is the gain of the PMT, k_{DAQ} is an additional amplification of the signal within the DAQ, N_s is the number of integrated samples and f_{ADC} is the sampling frequency of the ADC. For our case where the PMT was held at $V = 1750$ V the PMT gain from the manufacturer's specifications is $k_{\text{PMT}} \approx 2 \times 10^6$. The signal was amplified twice before being sent to the FADC and the snapshots were integrated over 25 samples. The sampling frequency of the ADC was set to 200 MHz.

The total voltage on the anode for N_{det} optical photons detected is now given by

$$V_{\text{sim}} = V_0^{\text{sim}} N_{\text{det}} k_c G_{\text{PMT}} + G_{\text{pedestal}}, \quad (6.31)$$

where k_c is a small correction to the simple V_{sim}^0 estimates, G_{PMT} is Gaussian function to match the statistical transport of electrons in the PMT and G_{pedestal} is another Gaussian function to account for small offsets in the pedestal of the real data. The latter Gaussian function is only used to match the simulation to the data and is not used in the determination of the analyzing power.

Comparison to Data

The same self-triggered snapshot data used in the determination of the pedestal in section 6.1.4 was used to validate the simulation. In fig. 6.18 I show the distribution of the integrated signal of individual photons using the snapshot data set. In order to determine only the Compton scattered photons we must subtract out the distri-

bution measured during the laser off periods from the laser on periods. We recall that the snapshot data are triggered on the incident photons whose signal is larger than a given discriminator threshold. We can see the effect of the discriminator by the sharp drop off as the voltage goes to zero. The sharp peak at zero voltage is due in part to the noise on the line randomly fluctuating high enough to satisfy the discriminator threshold. Another part is due to jitter in the discriminator threshold. It is for this reason that the snapshot data cannot be used to determine the analyzing power and hence we still need to rely on simulation to fill in the spectra to zero volts.

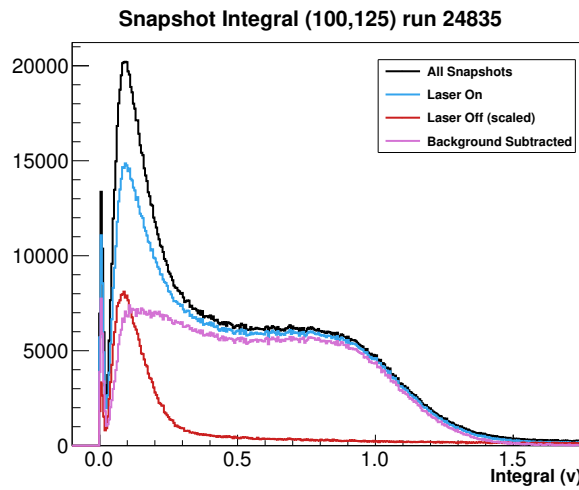


Figure 6.18: An example of the distribution of the integrated signal of individual photons in the snapshot data set. The black line corresponds to the sum of all incident photons on the detector. The blue and red histograms correspond to the laser on and off periods, respectively. The magenta histogram is the difference between the laser on and laser off histograms and should correspond to only Compton scattered photons. This includes the data from seven runs, whose average is 24835.

By using the model of the PMT described previously, we can convert the number of optical photons detected in the cathode and convert it to a voltage to make a similar plot. In fig. 6.19a I show the simulated spectra for the case when two thin pieces

of lead shielding were in front of the photon detector. The simulation is validated by matching the spectra at higher energies, which correspond to the higher voltages see on fig. 6.19a. The mismatch at lower energies is due in part to the discriminator effects discussed above. To illustrate this I simulated the discriminator by using an integrated threshold of 75 mV and smearing it by a Gaussian distribution with standard deviation of 50 %. The results are seen on fig. 6.19b which shows the same drop off around $V \sim 175$ mV. Part of the peak at $V \sim 0$ V is also explained by the use of this threshold, though, the rest of the peak is due to the fluctuations in the signal noise of the data and which are not included in this simulation.

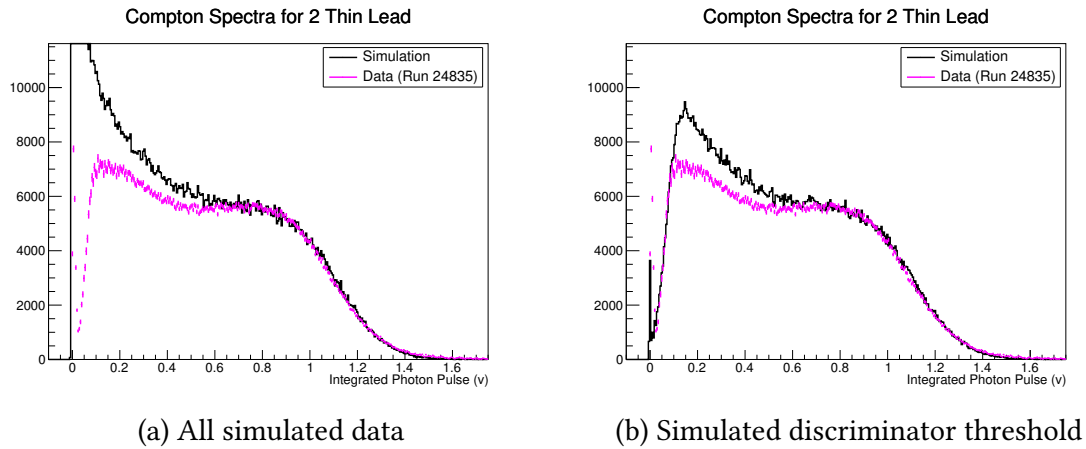


Figure 6.19: The distribution of the integrated signal due to the incident optical photons on the PMT of simulated Compton scattered photons. The full simulation (left) serves to fill in the gaps of the snapshot data which is restricted by a threshold. The discrepancy between the simulation and data at the lower voltages can be explained in part to the threshold of the discriminator. An example where the threshold is simulated (right) gives a better match. The remaining mismatch is thought to be associated with a non-linear response of the detector signal.

The remaining mismatch is thought to be due to a rate dependent non-linearity behavior of the detector signal. This rate dependence effect was unmeasured and is left as the single largest source of uncertainty. To get the sense of the impact of

of non-linearity in the signal I tried a simple model where I weight the spectra in fig. 6.19a by a Gaussian centered at $V = 0.2$ V and with a standard deviation spanning the entire range of the spectra. The result increased the determined analyzing power by 3 %. Such a drastic non-linearity is not expected in this system based on the results of [23] which measured a large non-linearity only in the lower energy region.

6.2.2 Determined Analyzing Powers

To determine the analyzing power from the modeled PMT signal discussed before we modify eq. (6.25) and now write the analyzing power in terms of the signal on the PMT anode. Let $\rho_i \epsilon(\rho_i) S(\rho_i) \rightarrow V_{\text{sim}}^i$ and the analyzing power becomes

$$A_{\text{th}} \approx \frac{\sum_i A_l^i V_{\text{sim}}^i}{\sum_i V_{\text{sim}}^i}. \quad (6.32)$$

The V_{sim} term should also contain the correction for the detector non-linearity, however, they were not determined for this dissertation. The corresponding analyzing powers are shown in table 6.1, where the error is only statistical.

Systematic Errors of the Analyzing Power

The dependence on the detector offsets with respect to the interaction point were also studied. During the six month data taking period we had occasional contact with the photon detector. This was due mostly to attempts to commission the system to measure the detector linearity during the data taking period. This resulted in accidentally shifting the position of the photon detector with respect to the in-

Runs	Shielding	Analyzing Power (A_{th})
23412 - 23653 23946 - 24581	1 thin lead	$(2.0012 \pm 0.0063) \%$
24612 - 24635	no thin lead	$(1.9770 \pm 0.0061) \%$
24636 - 25000 25250 - 25500	2 thin lead	$(2.0258 \pm 0.0066) \%$
Special 879 MeV running		
25030 - 25211	2 thin lead	$(1.5092 \pm 0.0052) \%$

Table 6.1: Analyzing powers determined from Monte Carlo for the three shielding configurations. Statistical errors only. Not corrected for detector non-linearity.

teraction point. In November 2011 an initial survey of the photon detector position in relation to the interaction point, and the results are shown in fig. B.4. At the end of the experiment, another survey was performed in May 2012 whose results are in fig. B.5. By comparing the two surveys we see that the photon detector was shifted in the horizontal direction by 4.6 mm and 0.6 mm in the vertical direction in relation to the interaction point.

A series of special simulations were made where the photon detector was offset by to 0.6 mm in the horizontal direction, relative to the interaction point. No effect was observed for the unshielded photon detector, but an effect of 0.08 % and 0.25 % was observed on the one and two thin lead shielding configurations, respectively.

Similarly, the sensitivity to the electron beam energy was studied. During normal operations the energy distribution of the beam is kept at a level of 10^{-4} . To study the effect of energy on the determined analyzing power, a simulation was performed where the electron beam energy was offset by +2.5 MeV, a much larger

deviation than the expected uncertainty during normal operations. An effect of 0.15 % was found on all shielding configurations, which when scaled to a more realistic ± 0.5 MeV corresponds to only a 0.02 % effect.

6.3 Beam Polarizations from the Photon Detector

With the analyzing powers from table 6.1 and the measured asymmetries of fig. 6.13b, we get the determined beam polarizations seen in fig. 6.20. Starting at run 24600, there is a large discrepancy between the photon detector and the electron detector results. Comparing further with the Møller measurements confirms that the outlier is the photon detector. I do not know the source of this discrepancy, and it does not show up anywhere else. It is possible that it can be due to a load dependence on the detector linearity. However, this has also not been confirmed.

Incidentally, the jump occurs near the same time that we made an aggressive effort to understand the system non-linearity. This was done by installing and testing a series of electronics near the photon detector that will systematically fire two LEDs into the detector. It is likely, though, still unconfirmed that this was the source of the discrepancy. All I can do, is assign an error to the measurement for this period on the scale of the discrepancy between the photon detector and electron detector results. This corresponds to an error of ~ 3 % on the polarization.

6.4 Additional Corrections and Errors

Before finalizing the polarization of the photon detector, let us first consider some special possible corrections or sources of errors.

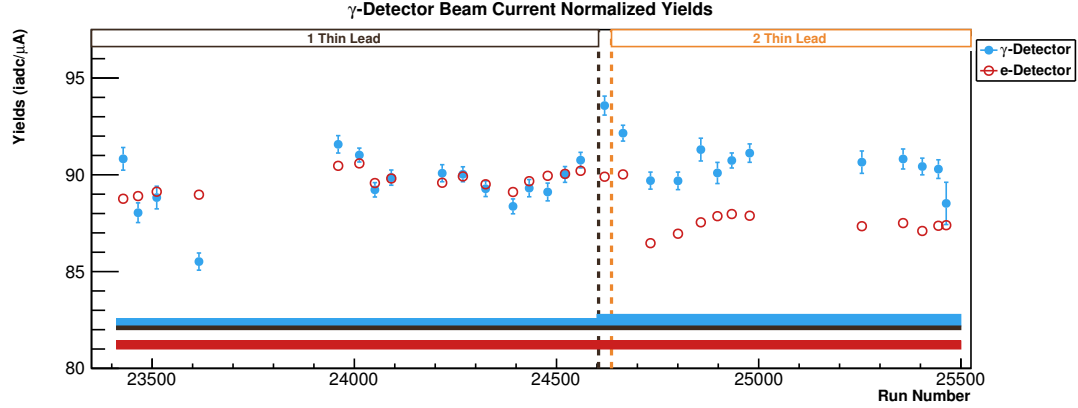


Figure 6.20: The time dependent beam polarizations as determined by the photon detector analysis. Statistical errors are shown on each point. The known systematic errors on the measured polarizations are shown as bands. The blue band corresponds to error contribution from the measured asymmetries, and the dark brown band corresponds to contributions from the analyzing power. The electron detector measured polarizations are also shown in red. The statistical errors for the electron detector are smaller than the size of the marker. The corresponding systematic error band for the electron detector is shown in red. Not shown are possible hidden errors on the photon detector results which contribute to the large discrepancy in results after run 24600.

6.4.1 Spin Precession and Depolarization Effects

The precession of a particle, in our case an electron, through a magnetic field could be written down just classically as a time dependent flip, such as

$$\frac{d\mathbf{P}}{dt} = \boldsymbol{\Omega} \times \mathbf{P}. \quad (6.33)$$

If we consider a case where there is no net electric field ($\mathbf{E} = 0$), then in the classical sense the electron spin represents a magnetic dipole where we must ignore the half-integer nature of the spin. As a result the equations of motion take the form of the

Thomas-BMT equation written as[84]

$$\boldsymbol{\Omega} = -\frac{e}{m_e \gamma} \left[\gamma \left(\frac{g_e - 2}{2} \right) \mathbf{B} - (\gamma - 1) \left(\frac{g_e - 2}{2} \right) \frac{(\mathbf{v} \cdot \mathbf{B})}{v^2} \mathbf{v} \right], \quad (6.34)$$

where e and m_e is the electrons charge and mass respectively, γ is the Lorentz factor, $(g_e - 2)/2$ is the anomalous magnetic moment of the electron as introduced in chapter 3, \mathbf{B} is the magnetic field vector and \mathbf{v} the electron's velocity vector. In the case of the Compton Chicane, the magnetic field is purely transverse to the direction of motion ($\mathbf{v} \cdot \mathbf{B} = 0$) so that eq. (6.34) simplifies to

$$\boldsymbol{\Omega}|_{\mathbf{v} \cdot \mathbf{B} = 0} = -\frac{e \mathbf{B}}{m_e} \left(\frac{g_e - 2}{2} \right). \quad (6.35)$$

The process becomes more complex when we return back to the quantum nature of the spin, and now consider not only changes to the polarization vector direction (\mathbf{P}) but also depolarization effects due to things such as radiation, due to the charge particle in the bending in the magnetic field, and spin flips. Fortunately [84] worked out the details for these cases and the derived the net change of the polarization after each piece wise magnetic field as

$$\Delta\phi = \gamma \left(\frac{g_e - 2}{2} \right) \phi, \quad (6.36)$$

where ϕ is the direction of the polarization vector \mathbf{P} in the beam direction. We can then place an upper limit on the difference in the polarization measured at the interaction point in the Compton Chicane to that incident on the $Q_{\text{weak}} \text{ LH}_2$ target downstream.

Consider now the polarization vector that makes an angle ϕ_{LH_2} with respect to the beam +z direction, then the longitudinal component of that polarization is defined by

$$P_{\text{long}}^{\text{LH}_2} = P_{\text{long}}^{\text{IP}} \cos(\phi_{\text{LH}_2}) + P_{\text{trans}}^{\text{IP}} \sin(\phi_{\text{LH}_2}), \quad (6.37)$$

where P^{IP} is the polarization measured at the interaction point. We can then get ϕ_{LH_2} when we include eq. (6.36) as

$$\phi_{\text{LH}_2} = \phi + \Delta\phi = \phi + \gamma \left(\frac{g_e - 2}{2} \right) \Delta\theta. \quad (6.38)$$

At the Q_{weak} beam energy of 1.1159 MeV the precession of the spin is $\Delta\phi \sim 2.63\phi$. Consider that the magnetic fields of the third and fourth dipole give a net zero magnetic field to 0.3 %, then we already expect $\Delta\phi \ll 1$, and as a result $\phi_{\text{LH}_2} \sim \phi$ with some error. To place an upper bound on the error, we consider any differences in the dipole currents. We already found that the current on dipole 3 varied no more than $\sim 0.5\%$ [85], but have not performed detailed studies of the difference between this and the fourth dipole current. For now, we will place the difference as high as 2 % [86]. The polarization angle ϕ is also expected to be small, considering that the average transverse polarization is only $\sim 1.05\%$ [87], while the longitudinal component is $\sim 89\%$. We can then express the error of eq. (6.37) as [86]

$$\delta P_{\text{long}}^{\text{LH}_2} < \sqrt{2}\phi\delta\phi \approx \sqrt{2}\phi \left(\frac{P_{\text{trans}}}{P_{\text{long}}} \right), \quad (6.39)$$

which places an upper bound of $\delta P_{\text{long}}^{\text{LH}_2} < 0.03\%$ [86].

6.4.2 Building the Table of Errors

By taking the various errors listed in this chapter, we can tabulate the average absolute error on the measured polarization and the results are in table 6.2.

Average Photon Detector Errors				
Source of Error	Error	$\delta(A_{ey})$	ΔP_e	Reference
Statistical		0.42 %	0.38 %	page 129
Systematics				
Scaler Deadtime	<0.05 %	($\ll 1$ %)	($\ll 1$ %)	section 5.3.2
H-C Charge Differences	1.78 μ A	0.03 %	0.03 %	section 6.1.7
H-C Position Differences	<0.1 nm	0.06 %	0.06 %	section 6.1.7
Residual Power in the FP Cavity	0.06 iadc/ μ A	0.52 %	0.47 %	page 131
H-C Pedestal Differences	<1 $\times 10^{-6}$ %	($\ll 1$ %)	($\ll 1$ %)	page 126
Beam Motion	<250 μ m	0.40 %	0.36 %	section 6.1.7
Analyzing Power Statistics	0.35 %	–	0.63 %	page 145
Detector Offsets	± 5 mm	–	0.19 %	page 145
Beam Energy	<1 MeV	–	0.03 %	page 146
Spin Precession	<0.03 %	–	($\ll 1$ %)	section 6.4.1
Unknown errors	–	–	~ 3 %	page 146
Total		0.53 %	3.15 %	

Table 6.2: Error contributions on the determination of the electron beam polarization using the photon detector. The notation ($\ll 1$ %) means the error is significantly small, and essentially zero. H-C stands for Helicity Correlated.

Chapter 7

A Blinded Q_{weak} Asymmetry

With the beam polarization finally determined, the next step is to determine the Q_{weak} parity-violating asymmetry. As of the writing of this dissertation, the asymmetry measurements remain blinded, a concept I'll explain in this chapter. The reader is reminded to keep this fact in mind as the results and discussions of these remaining chapters are not necessarily representative of the expected final Q_{weak} results. Additionally, the data set I will use in these results corresponds to only a subset of the entire Q_{weak} data set, corresponding to the dates of November 24, 2011 to May 17, 2012.

Before proceeding further, I would like to point out that a lot of the finer details, which I gloss over in this chapter, represent the work performed by the other members of the collaboration, for which I may not have had any involvement in. One can not perform a full analysis of the Q_{weak} data without the great support and dedication of the rest of the Q_{weak} collaboration, for which I am very grateful.

7.1 Determining the Measured Asymmetry

As previously mentioned, we can remove the dependence on the absolute helicity dependent cross sections by building a yield-normalized asymmetry. The first asymmetry we can build is of the net response, or yield, of the individual Cherenkov detectors, which we define as

$$A_{\text{raw}}^{\text{md}} = \frac{Y_{\text{md}}^+ - Y_{\text{md}}^-}{Y_{\text{md}}^+ + Y_{\text{md}}^-}, \quad (7.1)$$

where the Y_{md}^{\pm} is the integrated signal of a Cherenkov detector and averaged over both PMTs on the bar and then normalised to the beam current. The term “raw” is used to denote that this measurement contains no corrections outside of the pedestal correction and normalization to the electron beam current.

Recall from section 3.5.1 that perfectly sampling over the azimuthal symmetry removes any contributions to the asymmetry due to any transverse component in the beam polarization. Under the real experimental conditions the azimuthal symmetry may be broken by any misalignment in the detector or magnetic field, or by a non-centered electron beam trajectory. The term “false asymmetry” is then used to describe any process which gives rise to an asymmetry due to a broken azimuthal symmetry.

During the commissioning of the experiment, a lot of work went into minimizing these effects. Hence, by sampling over the detector azimuthal symmetry, we can minimize any residual effects due to false asymmetries[40]. We now define the raw asymmetry (A_{raw}) as the average of the eight individual Cherenkov detector asym-

metries. This asymmetry can be expressed as

$$A_{\text{raw}} = A_{\text{msr}} + A_{\text{false}}, \quad (7.2)$$

where A_{msr} is the asymmetry under perfect azimuthal symmetry and A_{false} are any residual false asymmetries. We identified three methods that give rise to false asymmetries[26]: transverse component to the electron beam polarization, effects due to any non-linearity in the detector response, and lastly effects due to the trajectory of the electron beam. We can then re-write the measured azimuthal asymmetry as

$$A_{\text{msr}} = A_{\text{raw}} - A_{\text{trans}} - A_{\text{detNL}} - A_{\text{beam}}, \quad (7.3)$$

where A_{trans} , A_{detNL} and A_{beam} are the false asymmetry due to the transverse component of the electron beam, the false asymmetry due to the beam trajectory, and the false asymmetry due to any detector non-linearity, respectively.

7.1.1 Blinding the Asymmetry

To shield the researchers from biasing the results of the analysis, whether unconsciously or not, a blinding factor was applied to the detector asymmetries of eq. (7.1). The blinded raw asymmetry is expressed as

$$A_{\text{raw}}^{\text{blinded}} = A_{\text{raw}} + A_{\text{blinding}} \quad (7.4)$$

where the asymmetry A_{blinding} is the blinding asymmetry defined as

$$A_{\text{blinding}} \equiv \text{sign}(\text{IHWP}) \text{sign}(\text{wien}) f_{\text{beam}} f_{\text{blinding}}, \quad (7.5)$$

where $\text{sign}(\text{IHWP})$ and $\text{sign}(\text{wien})$ are the signs corresponding to the IHWP and Wien angle given by eq. (6.19) and eq. (6.20), respectively, f_{beam} is the beam blinding factor, and lastly f_{blinding} is the blinding factor. The sign terms of IHWP and Wien angle are added to match the associated sign flip in the measured asymmetry due to the various IHWP and Wien angle configurations. If we had not matched this sign flip, comparison between the different IHWP and Wien measured asymmetries would reveal the blinding asymmetry.

Similarly, when the beam current is off the A_{msr} term in eq. (7.4) is zero and once again the blinding asymmetry would be revealed. For that reason the beam blinding factor f_{beam} is defined as

$$f_{\text{beam}} = \begin{cases} 1 & \text{for } I_{\text{beam}} > 0 \\ 0 & \text{for } I_{\text{beam}} = 0, \end{cases} \quad (7.6)$$

which forces the blinding asymmetry to be zero when the beam is off.

The blinding factor f_{blinding} is a non-zero uniform random number chosen such that

$$0 \text{ ppb} < |f_{\text{blinding}}| \leq 60 \text{ ppb}, \quad (7.7)$$

and is fixed for the entirety of this data subset.

We modify eq. (7.3) to write the blinded measured asymmetries as

$$A_{\text{msr}}^{\text{blinded}} = A_{\text{raw}}^{\text{blinded}} - A_{\text{trans}} - A_{\text{detNL}} - A_{\text{beam}}, \quad (7.8)$$

For the remainder of this dissertation, any mention of a raw or measured asymmetry will be a blinded asymmetry unless otherwise specified.

7.1.2 Blinded Detector Asymmetries

The Q_{weak} DAQ read out the information from a series of ROCs and wrote them into a number of 2 GB runlets, similar to the Compton DAQ described in section 5.3.6. These runlet files were stored in a high-capacity storage system maintained by the Jefferson Lab Computer Center. $Q_{\text{wAnalysis}}$ was then used to process the raw runlet files similar to the Compton data as described in section 5.3.6. However, due to the volume of data produced by the experiment, it was preferable to not store the resulting ROOT files in the high-capacity storage system. In lieu of storing all the ROOT files, only four values were stored for each measurement contained in a runlet file. The values corresponds to the mean, error, root mean squared and number of entries for each measurement. These values were stored in a MySQL database as similarly described in section 5.3.6 for the Compton data set. Special ROOT files were subsequently built and distributed to the collaboration for individual analyses[88].

I took the the slug averaged ROOT files produced on April 01, 2015. The data used in the averages included only data which passed a series of selection criteria. For example, only the data from periods in which the beam was on and stable was

considered. On occasion the beam abruptly turned off, a term commonly known as a “beam trip.” As a safety precaution to prevent unnecessary stress on the thin LH_2 aluminum windows, the beam would be brought up slowly from a beam trip. It would take up to 45 s to recover from a trip. To be certain the trip was over, an automated selection criteria would exclude the entirety of the trip with an additional four seconds to ensure it has reached stability[69]. From here forward, I will refer to any selection criteria as a “cut,” a term similar to the act of cutting a section of film from a reel.

Additional cuts were included which removed other bad periods, including removing single helicity level measurements due to an error in the electronics read out[3]. The cuts included in this data has already been described elsewhere[2, 3, 24, 46, 69, 89].

The runlet asymmetries I used were grouped into slugs and error weighted averaged together. The asymmetries were averaged over all 16 PMTs on the eight Cherenkov bars with their respective gains included. This should minimize any sensitivity to any gain mismatch between the detector PMTs. The results are shown graphically in fig. 7.1 for the entirety of the Run II data taking period corresponding to November 24, 2011 to May 17, 2012. These represent the raw, and blinded, asymmetries with no corrections applied except for the corresponding pedestal, gain and beam current normalizations described previously. The average raw asymmetry is (162.10 ± 7.79) ppb where only the statistical error contribution is included. Next, I will describe the corrections for any false asymmetries.

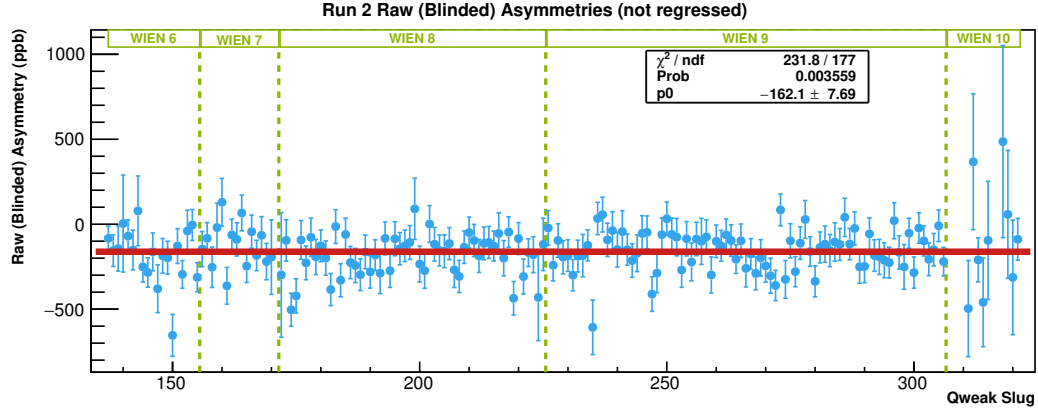


Figure 7.1: The slug averaged Run II raw asymmetries. Only No regression or linearity corrections applied. Only statistical errors shown.

7.1.3 Corrections Due to Beam Properties

It will be useful to discuss the corrections due to the beam properties, since we can directly use these results to study the contributions of the transverse component to the beam polarization. We can study the effects of beam properties by rewriting A_{beam} from eq. (7.8) as

$$A_{\text{beam}} = \sum_i \left(\frac{\partial A_{\text{raw}}}{\partial \chi_i} \right) \Delta \chi_i, \quad (7.9)$$

where χ_i is a beam parameter whose deviation from the mean is given by $\Delta \chi_i$ and the partial derivative term is the sensitivity of the raw asymmetry to this beam parameter. For this analysis, I relied only on linear regression on the natural jitter of the beam to determine the contributions due to the beam properties. Though I expect that the final analysis by the collaboration will include the results measured by the beam modulation system described in section 4.7.5.

We can use any combination of beam parameters in eq. (7.9) as long as they span the entire range of sensitivities suspected to give rise to a false asymmetry. There

were up to 13 such combinations, which we classify as regression schemes[89]. I briefly studied the effects of all thirteen schemes to determine the most useful in this analysis. With only three exceptions, they were all found to be fairly consistent with each other. The results are tabulated in table C.1. Schemes 5, 6 and 13 were excluded due to incomplete coverage for all the measured asymmetries. The large deviation from set 9 includes a luminosity monitor which is highly sensitive to other background processes making the fit highly improbable. The probabilities of the fits are also listed. We can further evaluate the quality of the regression scheme by studying the null asymmetry, which I'll explain next.

Computing the Null asymmetries

From section 4.1.2 we recall that we use a half-waveplate (IHP) to reverse the sign on the helicity every four to eight hours. This slow reversal is expected to minimize any systematic electronic effects on the Pockels cells[90]. A consequence of using an IHP is that the measured asymmetry will change sign depending on the IHP setting. Other processes may also reverse the sign of the asymmetry, such as the settings on the Wien. In general, the sign of the measured asymmetry is expressed as

$$\text{sign}(A_{\text{msr}}) = \text{sign}(\text{IHP}) \text{sign}(\text{wien}) f_{g-2}, \quad (7.10)$$

where the term f_{g-2} is an additional sign correction to account for the precession of the electron spin as it is transported through the accelerator. For any specific Wien and spin precession setting, we can construct groups of opposite IHP settings. The

asymmetry for these groups will be given as

$$A_{\text{msr}}^{\text{phys}} = A_{\text{msr}}^{\text{IN}} - A_{\text{msr}}^{\text{OUT}}, \quad (7.11)$$

where $A_{\text{msr}}^{\text{IN}}$ and $A_{\text{msr}}^{\text{OUT}}$ are the measured asymmetries for IHWP IN and OUT, respectively. The superscript “phys” is to convey that, under proper corrections for background and false asymmetries, this corresponds to the asymmetry of electron-proton scattering with only a possible sign difference. To prove that the background and false asymmetries were properly removed, we construct special “null” asymmetries. These null asymmetries are defined so that under proper removal of any false asymmetries the null asymmetries are zero. Different null asymmetries may be constructed that are sensitive to different beam parameters. We start by expressing the false asymmetries as

$$A_{\text{false}} = A_1(\text{wien}) + A_2(f_{g-2}) + A_3(\text{IHWP}), \quad (7.12)$$

where A_1 and A_2 are false asymmetries that are insensitive to the IHWP, but flips sign under opposite Wien and spin reversals, respectively, and A_3 is a false asymmetry that is insensitive to Wien and spin reversals, but flips sign under opposite IHWP settings. There are three possible methods of constructing a null asymmetry which will evaluate the effectiveness of the regression scheme.

Method 1: For this method we define a null asymmetry as [90, 91]

$$A_{\text{NULL}}^1 \equiv \frac{A^{\text{IN}} + A^{\text{OUT}}}{2}, \quad (7.13)$$

where A^{IN} and A^{OUT} are asymmetries measured under opposite IHPW setting that we wish to test. We can use the asymmetry from eq. (7.2) in place of A^{IN} and A^{IN} on the above equation and then use eq. (7.11) and eq. (7.12) to get

$$A_{\text{NULL}}^1 = A_1(\text{wien}) + A_2(f_{g-2}). \quad (7.14)$$

The result is that an asymmetry defined in this form provides direct access to the IHPW insensitive terms of the false asymmetry. For a specific Wien and spin precession setting this asymmetry may be nonzero. However, the terms $A_1(\text{wien})$ and $A_2(f_{g-2})$ expected to flip sign for opposite Wien and spin precession settings. The average over all settings in Run II will cancel this asymmetry[91].

In fig. 7.2 we see the results of this null asymmetry for two cases. The data are grouped into groups of three to five slugs which we refer to as a ‘‘Pitt’’ group, named after the person who suggested using grouping at time scales smaller than the monthly Wien setting changes[92]. In fig. 7.2a I applied no linear regression to the raw asymmetry, where in fig. 7.2b the set 10 regression scheme was used. We confirm that for specific Wien settings the null asymmetry may be nonzero but the average over the entire running period is consistent with zero for the given errors. Only statistical errors are shown, where I took the average error for the slugs in the Pitt grouping. This is a first approximation to the error and will require revising.

Method 2: We define a second null asymmetry as[90, 91]

$$A_{\text{NULL}}^2 \equiv \frac{\text{sign}(\text{wien},1) \text{sign}(f_{g-2,1}) A^{\text{IN}} - \text{sign}(\text{wien},2) \text{sign}(f_{g-2,2}) A^{\text{OUT}}}{2}. \quad (7.15)$$

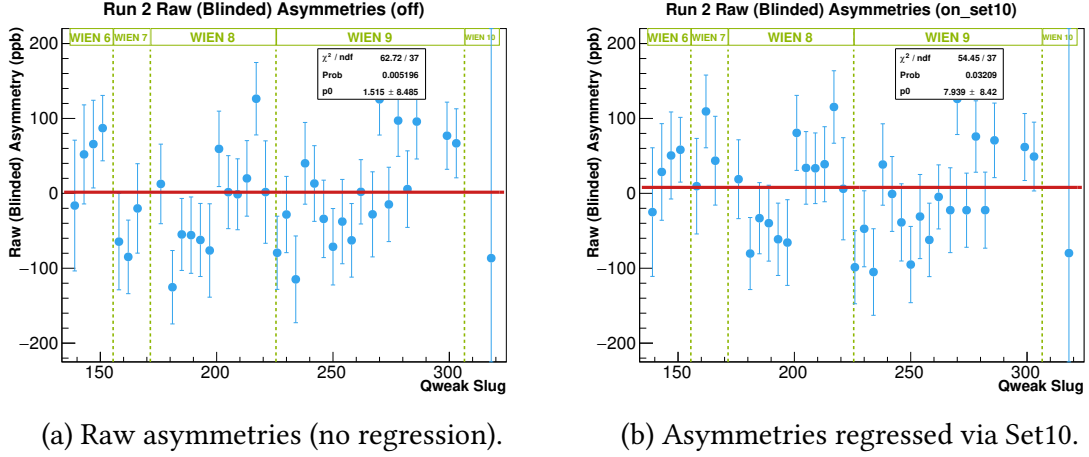


Figure 7.2: The null asymmetries A_{NULL}^1 for all the Run II data. The average over the entire period for both the un-regressed raw asymmetries (left) and the asymmetries regressed under the Set10 scheme (right) are consistent with zero for the given errors. Only statistical errors are shown.

Use the procedure outlined in the first null asymmetry rewrite the above equation as

$$A_{\text{NULL}}^2 = \frac{S_{w,1}S_{g2,1}(A_{\text{msr}}^{\text{IN}} + A_1 + A_2) - S_{w,2}S_{g2,2}(A_{\text{msr}}^{\text{OUT}} + A_1 + A_2)}{2} + A_3(\text{IN/OUT}), \quad (7.16)$$

where $S_{w,i} \equiv \text{sign}(w_{\text{ien},i})$ and $S_{g2,i} \equiv \text{sign}(g_{-2,i})$, and A_3 is the false asymmetry term that flips sign with the IHWP setting. If we were to select a single Wien and spin precession setting for both IHWP settings, then we would leave a contribution of half the A^{phys} term. Instead select Wien and spin reversal settings such that $\text{sign}(w_{\text{ien},1}) \text{sign}(f_{g-2,1}) = -\text{sign}(w_{\text{ien},2}) \text{sign}(f_{g-2,2})$. Then the fractional term in the equation above cancels and the null asymmetry reduces to

$$A_{\text{NULL}}^2 = A_3(\text{IN/OUT}). \quad (7.17)$$

I did not study this null asymmetry in any great detail of detail.

Choosing a Regression Scheme

Given that most regression schemes are consistent with each other, I will use the scheme defined by set 10 since it is the most probable at 5.14 % and the most likely $\chi^2 = 1.18$ per degree of freedom. Furthermore, the null asymmetries produced with this regression scheme are consistent with zero. Set 10 uses six beam parameters corresponding to the horizontal and vertical positions x and y on the beam, respectively, with their corresponding slopes. Additionally it uses the beam energy and the beam current measured by BCM 6¹.

From table C.1 we get the regressed asymmetry for set 10 as (-161.60 ± 7.63) ppb which means $A_{\text{beam}} = -0.5$ ppb. The error is harder to untangle due to correlations between the beam parameters. However, as of the writing of this dissertation, they are believed to be ~ 3 ppb[93].

7.1.4 Transverse Polarization and Signal Non-Linearity

For the Run I data than 1 % residual transverse polarization was found. However, the contribution of this residual transverse polarization on the asymmetry when averaged over all eight Cherenkov bars was considered to be insignificant[24]. However, this determination still contributes ± 1.6 ppb to the overall asymmetry uncertainty[94].

Effects of signal non-linearity were also studied[3] and found to have not net contribution on the asymmetry. Similarly to the transverse, the contribution to the

¹This is a different BCM than the BCM identified in section 6.1.1. The mix of numbers is due to a mislabeling on the Compton DAQ which mislabeled BCM 17 as BCM 6.

uncertainty of the asymmetry is ± 2 ppb [94].

7.2 Determining the PVES Asymmetry

Even with false asymmetries removed eq. (7.8) does not yet represent only the contributions from the electron-proton scattering of interest. Furthermore, the asymmetry has been diluted by electron's longitudinal polarizations discussed in the previous chapter. We can use eq. (3.47) to write the polarization corrected form of eq. (7.8) as

$$A_{\text{msr}}^{\text{pcorr}} = \frac{A_{\text{msr}}}{P_L}, \quad (7.18)$$

where P_L is the longitudinal polarization of the electron beam. We keep in mind that A_{msr} remains blinded, and will continue to represent the blinded asymmetry for the remainder of this dissertation.

In chapter 6 we saw the effects of background contributions on a measured asymmetry. We must also remove the contribution of any background processes on eq. (7.18). We derive the following form of a background corrected asymmetry

$$A_{\text{bkgcorr}} = \frac{A_{\text{msr}}^{\text{pcorr}} - \sum_i^4 f_i A_i}{1 - \sum_i^4 f_i}, \quad (7.19)$$

where A_i is the asymmetry of any background process and f_i is the fractional yield

contribution of the background defined as

$$f_i \equiv \frac{Y_i}{Y_{\text{msr}}}, \quad (7.20)$$

The full derivation of eq. (7.19) can be found in appendix E.

We identified four possible sources of backgrounds[26]. The first due to the use of an Al cell to hold the LH_2 target. Only the thin (~ 5 mil) entrance and exit windows contribute, which gives the fractional yield as $f_{\text{Al}} \approx 0.3\%$. However the asymmetry of Al is of the scale of 10^3 ppb, which can still significantly effect the measured electron-proton asymmetry. Other background sources include scattering off any element in the beam line, neutral particles having direct line of sight to any of the eight Cherenkov bars, or contributions due to inelastic scattering processes. Each will be discussed in turn in later sections.

For now, let us continue the discussion of eq. (7.19), which is only one step away from representing the real parity-violating electron-proton asymmetry. There are four more identified components which can affect the measured asymmetry[3]. One effect comes from energy loss of the electron as it travels through the 35 cm long LH_2 target. The second is to account for the distribution of light along the Cherenkov bars. The third effect is due to the non-uniform distribution of electron scattered with different Q^2 on the Cherenkov bars. We term these four corrections as “experimental biasing” since they are due to a bias introduced by the detector setup. We associate three corrections to these four effects given as R_{RC} , R_{det} , R_{Ω} , respectively. We combine all these corrections into[3]

$$R_{\text{total}} = R_{\text{RC}} R_{\text{det}} R_{\Omega} R_{Q^2}. \quad (7.21)$$

We apply this correction directly to eq. (7.19) and write the final form for the experimentally measured elastic electron-proton scattering asymmetry as[26]

$$A_{\text{ep}}^{\text{PV}} = R_{\text{total}} \left(\frac{\frac{A_{\text{msr}}}{P_L} - \sum_{i=1}^4 f_i A_i}{1 - \sum_{i=1}^4 f_i} \right). \quad (7.22)$$

7.2.1 Background Corrections

In order to properly account for any background process in eq. (7.22) we need to know both the yield fraction f_i and the asymmetry A_i for all background processes. In this section, I will summarize the work performed by others in the collaboration to determine these specific values. I will also show the latest results, with the caveat that they are preliminary and not necessarily the final expected values.

Beamline Backgrounds

The background asymmetries can be directly measured from a special test in which a tungsten shutter was placed in the opening of the first and fifth octant of the second collimator. This effectively blocked the scattered electrons into the first and fifth Cherenkov detector. Any signal incident on the detector was believed to be from scattering from the tungsten plug or from the beam line. The fractional yield was determined from comparing the blocked Cherenkov detector from the unblocked, as

$$f_{\text{bbkg}}^{\text{md}} = \frac{Y_{\text{md}}^{\text{blocked}}}{Y_{\text{md}}}, \quad (7.23)$$

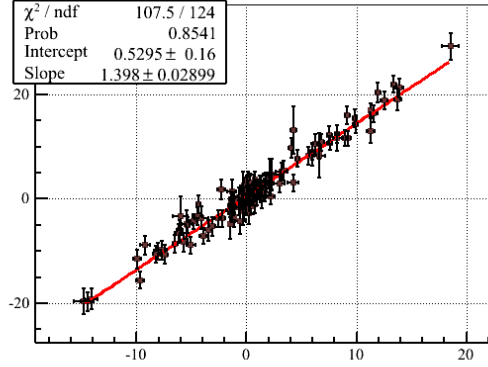


Figure 7.3: An example of the strong correlation between two background detectors[98]. The vertical axis is the asymmetry of the PMT-only detector and the horizontal is the average asymmetry in the US lumi. The units are in ppm.

where “md” refers to the main detector and was measured to be[94–96]

$$f_{\text{bbkg}}^{\text{md}} = (0.193 \pm 0.064) \%. \quad (7.24)$$

The asymmetry could also be directly measured directly from the blocked octant. However, we can use the various background detectors discussed in section 4.6 to monitor and measure this asymmetry. What the blocked octant studies proved was the direct correlation between the measured asymmetries of the upstream Lumis and the background asymmetries on the blocked octant[97].

Strong correlation between the various background detectors was also found as seen on fig. 7.3[98]. With direct evidence that the background monitors are correlated. Add the direct evidence of correlations between background monitors and the Cherenkov detectors. Then we measure any time based fluctuations in the beamline

scattering asymmetry. The correlation is determined as[99]

$$C_{\text{bkgdet}}^{\text{md}} = f_{\text{bkg}} m_{\text{bkgdet}}^{\text{md}}, \quad (7.25)$$

where $m_{\text{bkgdet}}^{\text{md}}$ is the slope. The correlations of the upstream Lumi and the the Cherenkov detectors was found to be stable throughout the entire running period[100]. The correlation for regression scheme set 10 is[100]

$$C_{\text{bkgdet}}^{\text{md}} = (5.00 \pm 1.62) \text{ ppb/ppm}. \quad (7.26)$$

The units of ppm in the numerator is due to the very large asymmetries measured in the background detectors, as seen on fig. 7.3.

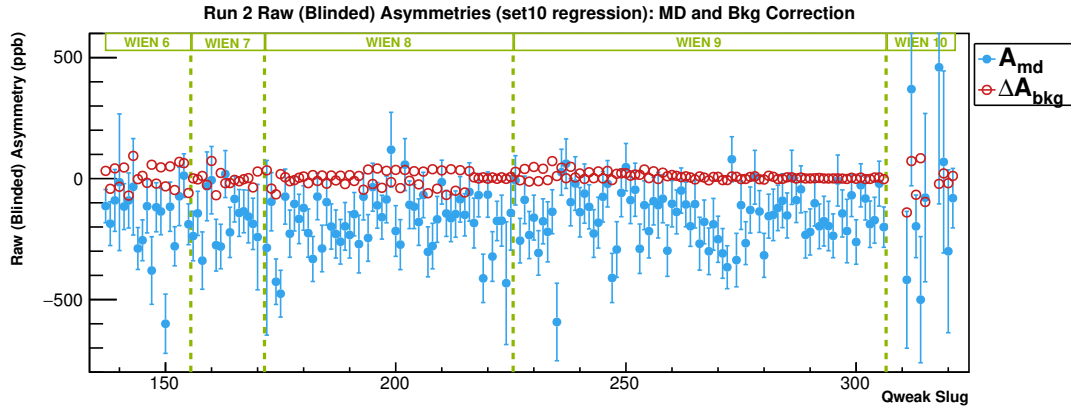


Figure 7.4: Regressed asymmetries using set 10 regression scheme with an overlay of the the background correction. The background correction corresponds to $\Delta A_{\text{bkg}} = C_{\text{bkgdet}}^{\text{md}} A_{\text{uslumi}}^i$.

In fig. 7.4 I overlay the background correction to a plot of regressed asymmetries. The correction is applied individually to each slug as[3]

$$A_{\text{bkgsub}}^i = A_{\text{msr}}^i - C_{\text{bkgdet}}^{\text{md}} A_{\text{uslumi}}^i. \quad (7.27)$$

We can study the effects of applying the corrections to the average asymmetry for the entire Run II period. The average asymmetry of the upstream Lumi for all of Run II is

$$\langle A_{\text{uslumi}} \rangle = (0.379 \pm 0.011) \text{ ppm}, \quad (7.28)$$

which gives an overall background correction of

$$\langle \Delta A_{\text{bbkg}} \rangle = (-1.985 \pm 0.616) \text{ ppb}. \quad (7.29)$$

We can use the results of eq. (7.24) to convert this to an asymmetry, which we find to be

$$A_{\text{bbkg}} = (-981 \pm 455) \text{ ppb}. \quad (7.30)$$

Compare this to the results when the correction is applied on a slug by slug level, whose figures can be found in appendix D. The average correction when applied slug by slug is

$$\langle \Delta A_{\text{bbkg}} \rangle = (-2.9 \pm 10.8) \text{ ppb}. \quad (7.31)$$

The error in this case is an over estimation since the error has to account for the correlations between all variables in the asymmetry and in the background correction. An effort is underway to understand the true error, which is expected to be much lower[101, 102].

Aluminum Windows

We directly measured the signal contribution from the thin Al windows to the Cherenkov detector signals. This was achieved by comparing the signals of the

nominally filled LH_2 target to those of an empty target. During a special period the LH_2 was removed from the target container and the signal on the Cherenkov bars was measured[2]. This had to be performed at very low currents due to the fact that the LH_2 also serves to cool the windows. At high current the Aluminum windows would have been destroyed. We keep this effect on in mind as I discuss the details of measuring f_{Al} .

Comparison of the signal on an emptied target Y_{empty} to that of the LH_2 filled target Y_{LH_2} gives us the fractional contribution of Al as[103]

$$f_{\text{AL}} = \frac{Y_{\text{empty}}}{Y_{\text{LH}_2}}. \quad (7.32)$$

The yields are determined by incident rates R on the Cherenkov detectors, where the rates are given as

$$R \equiv \frac{N}{t}, \quad (7.33)$$

where N is the number of detected electrons over a period t . We can directly measure N , as opposed to an integral like the main Q_{weak} data set, because at these low currents individual readout of incident electrons is possible. To account for the different currents used between the empty and the filled target, the rates are normalized to the beam current. This means that the yield can be written as[103]

$$Y = \frac{R}{\langle I \rangle}. \quad (7.34)$$

Due to a large non linearity in the BCM signal at these low currents, the rates were also normalized to the signal of a reference Carbon target[104]. The corresponding

measured signal fraction between an empty target at $\langle I \rangle \approx 0.1 \mu\text{A}$ and the LH_2 target at $\langle I \rangle \approx 1.0 \mu\text{A}$ are shown in fig. 7.5[104].

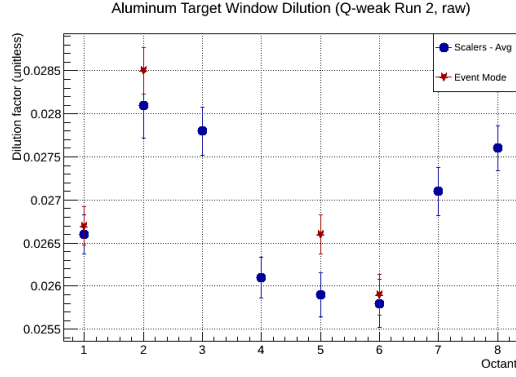


Figure 7.5: The determined fractional signal contribution of the Aluminum windows on the detector signal[104].

An octant dependent effect was measured as evident on fig. 7.5. We can reduce the overall systematic uncertainty by applying this correction on each octant individually. However, for purposes of this dissertation, the error weighted average is sufficient and given as $(2.670 \pm 0.009)\%$ where the error is only statistical. With a preliminary systematic uncertainty[94], we get

$$f_{\text{AL}} = 2.670 \pm 0.009(\text{stat}) \pm 0.011(\text{sys})\%. \quad (7.35)$$

The asymmetry of Aluminum was measured from a thick ($\sim 3.6 \text{ mm}$) pure Aluminum foil positioned at the same z -position of the downstream exit window. By using a thicker Aluminum foil allowed measurements to be made at beam currents up to $60 \mu\text{A}$. The asymmetry was measured using the same technique as eq. (7.22), where any background contributions to the measurement had to be removed. The asymmetry was also corrected for longitudinal polarization and any false asym-

metries. In fig. 7.6 the asymmetries corrected for beam polarization and beamline scattering background only are shown. Only statistical errors were shown and the average value is given as (1596 ± 69) ppb[105]. The corrections for the remaining backgrounds gives us an asymmetry of (1607 ± 70) ppb[106].

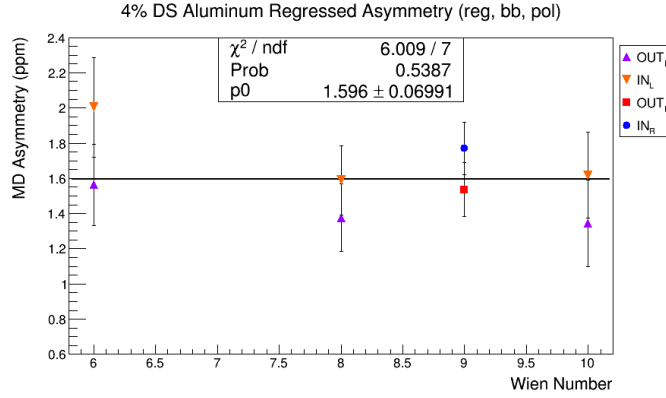


Figure 7.6: The measured asymmetries from a thick (~ 3.6 mm) pure Aluminum foil[105]. Only the statistical errors are shown. Asymmetries are regressed using regression scheme Set13 and are corrected for beamline scattering backgrounds and the beam polarization[105]. The sign of the asymmetry has been corrected for IHWP, Wien and spin precession.

This asymmetry requires a few more corrections, however. The radiative effects of the electron beam interacting with a thick Aluminum foil must be taken into account. Additionally, the thick foil is made of pure Aluminum while the target windows are an Aluminum alloy which contain small fractions of other metals. Theoretical models of the Aluminum window were input into Geant4 simulation to determine the corrections to the asymmetry. The model scales the measured asymmetries down by $\sim 6.7\%$ and contributes an additional uncertainty of ± 26 ppb[107]. Finally we get[106, 107]

$$A_{\text{Al}} = 1506 \pm 70(\text{stat}) \pm 15(\text{sys}) \pm 26(\text{model}) \text{ ppb}. \quad (7.36)$$

Inelastic Scattering Contributions

Due to the finite resolution of the spectrometer, inelastic processes also contributed to the measured yield and asymmetries. However, due to energy energy and momentum conservation, we find that the energy of the scattered electron is smaller than the elastic energy for the same scattering angle and Q^2 . The majority of these events can then be “filtered” by the magnetic field of the spectrometer. In fig. 7.7a we see a simulation of the relative rate of of the elastically scattered electrons compared to the inelastic and aluminum contributions, which have been scaled by 10^2 for visualization purposes only[108].

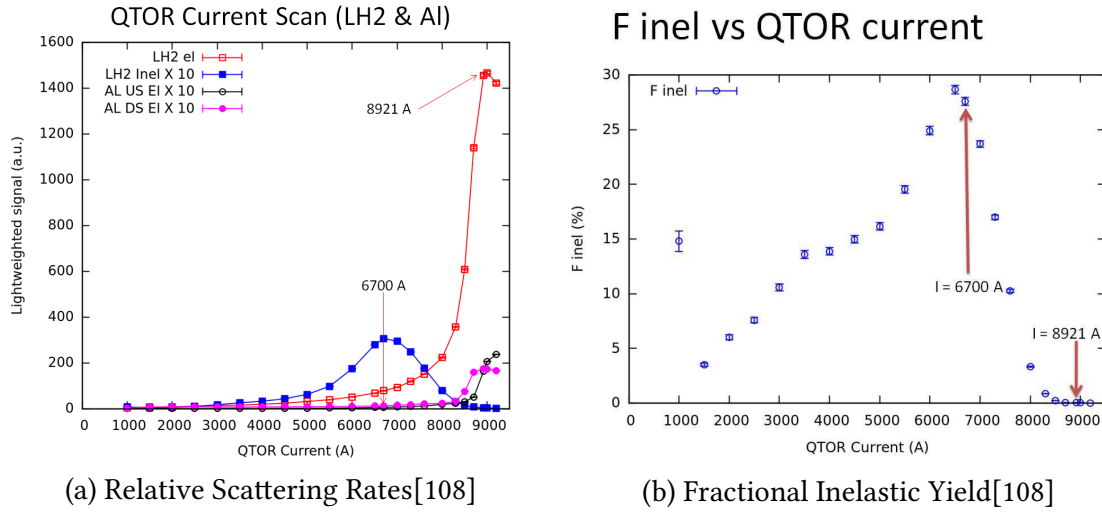


Figure 7.7: Simulations of the total scattering rates for various processes are show on the left. The horizontal scale corresponds to the current on the spectrometer which is proportional to the scattering energy of the particle. The figure on the right shows the relative fractional yield for the inelastic scattering energy distribution[108].

The inelastic processes at these kinematics are believed to be dominated by the $N \rightarrow \Delta$ transition, in which a nucleon is excited to a Δ state by a quark either flipping spin or quark flavor[39]. In particular the $p \rightarrow \Delta^+$ was determined as the primary

process[39].

There is no innate means of directly measuring the yield fraction of inelastic signal to the elastic signal on the Cherenkov bars. This is due to the fact that both elastic and inelastic scattering processes scatter from the same target, unlike the case for scattering from the Aluminum windows. However, a well understood simulations provides the expected relative rates of various processes, as we saw in fig. 7.7a. Here the horizontal axis is shown in units of the spectrometer's current. The current is related to the magnetic field which we can then relate to the scattered energy of the electron. In essence fig. 7.7a provides the relative rates of elastic, inelastic, and Aluminum contributions as a function of scattered electron energy.

By changing the current in the spectrometer, which in effect changes the scattering energy, to 6700 A we can center the inelastic peak on the Cherenkov bars[39]. The asymmetry of this peak can then be measured and the simulation will tell us the fractional yield at the nominal spectrometer current of 8921 A[39]. The fractional yield given at the nominal spectrometer setting is[3, 94, 108]

$$f_{N \rightarrow \Delta} = 0.02 \pm 0.0005(\text{stat}) \pm 0.02(\text{sys}) \%, \quad (7.37)$$

where the error is dominated by a very conservative 0.02 % [94]. The corresponding asymmetry is [94]

$$A_{N \rightarrow \Delta} = (-3020 \pm 970) \text{ ppb}, \quad (7.38)$$

where the combined statistical and systematics are shown.

Neutral Contributions

The last background contribution we consider are neutral particles which have direct line of sight to the Cherenkov detectors. These contributions are expected to be mostly from photons[69]. These photons can either be produced in the Tungsten plug or anywhere along the path of the spectrometer magnetic field. The contributions from the Tungsten plug were already studied in section 7.2.1. However, this method also blocks out contributions from photons produced in the spectrometer. These photons can either be produced via Compton scattering in the air, or scattering off the edges of the shield wall[109]. Furthermore, photons can be produced by scattering from the Lintels described in Chapter 2.

A different technique that did not rely on blocking off any octants was implemented[69]. This relied on using the tracking configuration at a beam current in the nA range. Neutral particles should produce little to no signal in the scintillating material of the Trigger Scintillator[69, 109]. However, they can still produce a signal in the Cherenkov detectors, which as the name suggest is dominated by emission of Cherenkov radiation. Charged particles, however, will produce a signal on both materials. Comparison between the signals produced in the Cherenkov bar with those produced in the Trigger Scintillator gives us the yield fraction of the neutrals. A preliminary measurement of the yield fraction is[94]

$$f_{\text{neutral}} = (0.127 \pm 0.138) \%, \quad (7.39)$$

where only statistical errors are shown.

The corresponding asymmetry is determined from simulations. Since photons

can be produced via any scattered electron in the spectrometer, the contributions to the asymmetry must include all likely initial scattering processes. The scattering rates of elastic electron-proton scattering, Møller scattering from the LH_2 target, scattering from the Al window and also the inelastic scattering processes from the target were included. The net asymmetry of the neutral backgrounds is [94]

$$A_{\text{neutral}} = (-283 \pm 57) \text{ ppb}, \quad (7.40)$$

where only statistical errors are shown.

7.2.2 Experimental Bias Corrections

The last remaining corrections are R_{RC} , R_{det} , R_{Ω} , respectively. Simulations were performed that modeled the energy loss in the target[3]. The ratio between the model with no energy loss and the various energy loss models gives us the correction, which was found to be[110]

$$R_{\text{RC}} = 1.0101 \pm 0.0007, \quad (7.41)$$

with only statistical errors have been determined as of the writing of this dissertation.

The distribution of light on the detector bars effectively biases the results. This has an added consequence that it affects the experimentally determined asymmetry. Simulations were performed where the incident optical photons on the Cherenkov bar PMTs were weighted by the light yield in the detectors along the length of the Cherenkov bars. The ratio of the “light weighing” result and the unweighted re-

sults gives us the correction as[111]

$$R_{\text{det}} = 0.992\,06 \pm 0.004\,40. \quad (7.42)$$

The Effective Q^2

Before discussing the remaining correction, we have to understand the distinction between the asymmetry given by eq. (3.36) and that which one measures in the Q_{weak} apparatus.

The asymmetry of eq. (3.36) correspond to electrons scattering off protons with well defined energy and scattering angle[112]. You then need to take into account account energy loss of an electron going through an elongated target or the biasing of the detectors into account. We already took into account those corrections above. Now we also consider that we have an acceptance of a range of angles $\Delta\theta_e$ scattering from a fixed position along the beamline. Now take into account that the target is 35 cm long and we find that there is a range of accepted angles $\Delta\theta_e^{\text{us}}$ at the upstream size of the target and a different $\Delta\theta_e^{\text{ds}}$. We recall the relation between the scattering angle, incident electron energy, scattered electron energy, and Q^2 from eq. (3.7). With the acceptances described above we conclude that the asymmetry measured corresponds to the average of the distribution of all asymmetries with a well defined Q^2 . The second conclusion is that we also cannot measure a single Q^2 but rather an average distribution of Q^2 . We define a correction R_{Ω} to relate the two as follows[3]

$$A(\langle Q^2 \rangle) = R_{\Omega} \langle A(Q^2) \rangle, \quad (7.43)$$

where R_Ω was determined from simulations as[94]

$$R_\Omega = 0.980 \pm 0.005. \quad (7.44)$$

The effective average Q^2 was[3, 94]

$$\langle Q^2 \rangle = (0.024\,55 \pm 0.000\,31) \text{ GeV}^2/c^2 \quad (7.45)$$

.

7.2.3 The Blinded Run II Parity-Violating Asymmetry

Gathering all the corrections together allows us determine the parity violating asymmetry by using eq. (7.22). To minimize any time variation effects due to false asymmetries, beam polarization and beamline scattering background, we compute and apply the corrections on a slug by slug level. For beam polarization I will be supplementing the electron beam polarizations with those determined with the electron detector in the Compton polarimeter, and the Møller polarimeter[113]. The benefit of using these polarization measurements is that the net error is only $\pm 0.67\%$ and more importantly, span the entire range of the Run II running period. Figure 7.8 shows the slug averaged measured asymmetries for all of Run II.

First, define the total scaling to the asymmetry due to background processes as

$$f_s = \frac{1}{1 - f_{\text{bbkg}} - f_{\text{Al}} - f_{\text{neutral}} - f_{N \rightarrow \Delta}}. \quad (7.46)$$

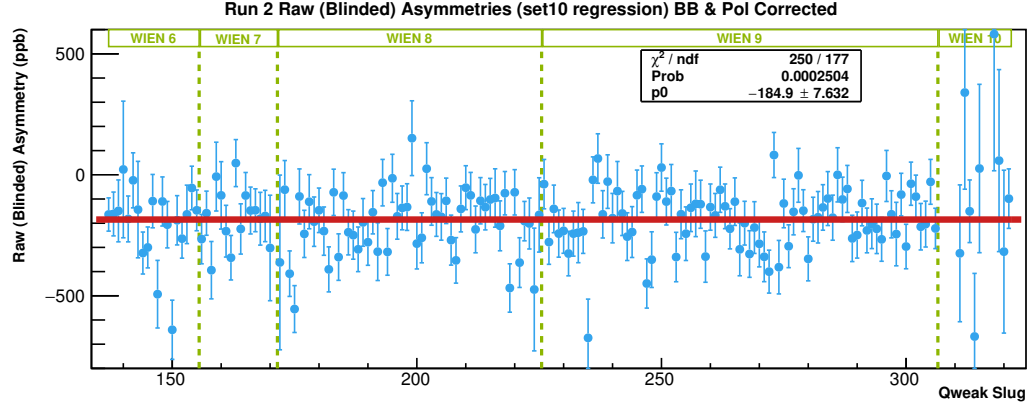


Figure 7.8: The measured regressed asymmetries averaged into slugs. Regression scheme set 10 was used. Beamline background corrections and polarization corrections have been applied. Only statistical errors shown.

By using the numbers provided previously we get

$$f_s = 1.0310. \quad (7.47)$$

Then take the average background and polarization corrected asymmetry from fig. 7.8 and scale it by f_s to get

$$f_s A_{\text{msr}}^{\text{bkg.pol}} = (-190.6 \pm 7.6) \text{ ppb}, \quad (7.48)$$

where the error has not been scaled yet and will be determined at the end. The sum of the background asymmetries is given by

$$f_s \sum_i^3 f_i A_i = 36.3182 \text{ ppb}. \quad (7.49)$$

Lastly the total correction for experimental biasing is

$$R_{\text{total}} = 0.982. \quad (7.50)$$

All combined we get the blinded parity-violating asymmetry for electron-proton scattering

$$A_{ep}^{\text{PV}} = -221.2 \pm 9.4(\text{stat}) \pm 60(\text{blinding}) \text{ ppb}. \quad (7.51)$$

The propagation of errors is taken from [3].

Chapter 8

Results and Discussions

In this final and brief chapter, we will take the parity-violating asymmetry from the last chapter and use it to determine the weak charge of the proton. Keeping in mind that the dominant error is given by the blinding asymmetry. First, however, I will outline the process.

8.1 The World PVES Data

We recall that the asymmetry can give us access to Q_w^p by treating the weak charge as the intercept when $Q^2 B(Q^2, \theta) \rightarrow 0$ in eq. (3.46). As a quick estimate, we can see if our measured asymmetry is of the right scale by assuming that our measured Q^2 is essentially zero. Then from eq. (3.46) we get a $Q_w^p(Q^2 \neq 0) \approx 0.1049$. To do better, we need to extrapolate to zero, which will require fitting the data from other Parity Violating Electron Scattering (PVES) experiments.

We gathered data from light-nuclei PVES data at low Q^2 using ^1H , ^2H , and ^4He targets[26]. Then followed the procedure described in the literature[114, 115].

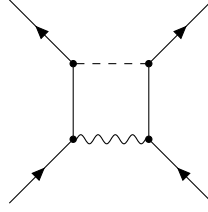


Figure 8.1: γZ -box diagram, in which an interaction exchanges two virtual particles, a photon and a Z -boson.

Parametrization of the form factors could use either Kelley[116] or Arrington and Sick[117]. The choice of form factor parametrization was studied and found to be consistent within one standard deviation[118]. The fit involved data up to $Q^2 = 0.63 \text{ GeV}^2/c^2$. At these low values we were not affected by the discrepancy in the electromagnetic form factors between the Rosenbluth separation and polarization transfer methods[119].

8.2 Determination of the Blinded Q_w^p

The fit involved five free parameters, the weak quark coupling constants C_{1u} and C_{1d} , the strange charge radius ρ_s , the magnetic moment μ_s and the iso-vector axial form factor $G_A^{Z(T=1)}$ [26]. The γZ -box diagram in fig. 8.1 required an energy dependence correction for each individual data point[26].

In fig. 8.2 we see a two dimensional representation of the five parameter fit. The vertical axis is the reduced asymmetry from eq. (3.46). The Q_{weak} data point, with the large 60 ppb blinding error, is the point closest to the vertical axis. With the blinding removed, this error should be reduced significantly. With the data included in this dissertation, the error without the blinding asymmetry is 4.3 % relative to the

measured asymmetry.

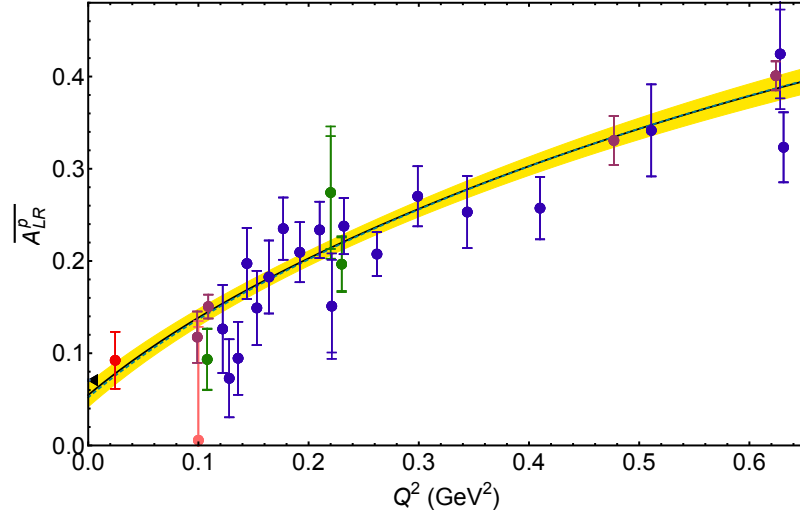


Figure 8.2: A projection of the five parameter fit to the world PVES data at low Q^2 into a 2D plot showing the reduced asymmetry as a function of Q^2 .

The blinded weak charge of the proton is

$$Q_w^p(\text{PVES,Blinded}) = (+0.0541 \pm 0.0127) \quad (8.1)$$

The current Standard Model prediction taken from the latest PDG is[6]

$$Q_w^p(\text{SM}) = +0.0708 \pm 0.0003, \quad (8.2)$$

which is $\sim 1.3\sigma$ away.

8.3 Extracting the Weak Coupling Constants

In writing the weak charge of the proton in chapter 2 we made use of the weak charges of the up and down quark C_{1u} and C_{1d} , respectively to write the proton's

weak charge as a sub of the constituent quarks. We can extend that further to larger nuclei and write the weak charge as[3]

$$Q_w^p = -2(C_{1u}(2Z + N) + C_{1d}(Z + 2N)), \quad (8.3)$$

where Z and N are the number of protons and neutrons in the nuclei, respectively. Comparing to the Atomic Parity Violating (APV) results allows us to extract values for C_{1u} and C_{1d} directly[3, 26]. In fig. 8.3 we compare the world PVES data to the results from an APV experiment on ^{133}Cs . The PVES data includes the blinded Q_{weak} result described in this dissertation.

The determined weak charges from fig. 8.3 are

$$C_{1u} = -0.179 \pm 0.006 \quad (8.4)$$

$$C_{1d} = +0.332 \pm 0.005. \quad (8.5)$$

Then writing out the weak charge of the neutron as $Q_w^n = -2(C_{1u} + 2C_{1d})$ and using the values from above we find

$$Q_w^n(\text{PVES+APV,Blinded}) = -0.9684 \pm 0.0104. \quad (8.6)$$

8.4 Closing Remarks

In this dissertation we have discussed a procedure to test the Standard Model at a relatively low energy of 1.12 GeV via a precision measurement of a well predicted Standard Model value. The end result was blinded by a large offset on the experimen-

tal asymmetry of up to ± 60 ppb. We can still make some observations on possible improvements for future experiments.

First, we recall the discrepancy between a global correction to the background due to beamline scatterings and the time based corrections on the slug level. For future experiments we will need to be able to understand and identify any correlation between the various beam monitors to a higher level. While I merely outlined the procedure in this dissertation, the real work required the constant effort of several people working since the end of the experiment.

For the polarization measurements for Run II where determined to a precision of better than 1 % absolute uncertainty. However, this was due to a combination of the Møller and electron detector of the Compton polarimeter. The photon detector results where not included for these quoted results due to the large associated errors found. These can be mitigated in the future by use of a linearity system which is available before the start of the experiment. This will help ensure that any load dependence non-linear behavior in the signal line is well understood for all time periods.

Other changes which will help in the future would be to calibrate photon detector with the electron detector. This was unavailable during the Q_{weak} running since both detectors where being commissioned at the same time. Now that both detectors are better understood, future experiments may make use of coincidence triggered events between the photon and electron detector as was done for for the HAPPEX-III experiment[23]. Using a dedicated photon beam, such as the High Intensity Gamma-Ray Source in North Carolina, can provide a better calibration.

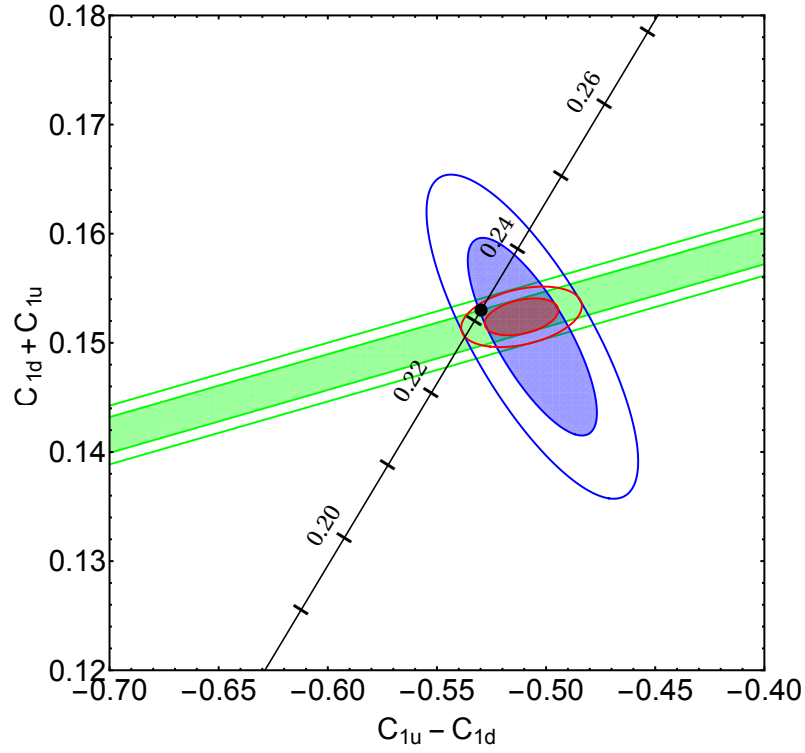


Figure 8.3: The constraints imposed the coupling constants C_{1u} and C_{1d} from the results of the world PVES and APV experiments. The vertical axis corresponds to the isoscaler ($C_{1u} + C_{1d}$) and the horizontal axis corresponds to the isovector ($C_{1u} - C_{1d}$). The green shaded area represent the constraints imposed by APV experiments with a 68 % confidence level, while the outer lines correspond to a 95 % confidence level. The purple ellipses corresponds to the constraints imposed by all the PVES experiments at 68 % and 95 % confidence levels, respectively. Finally the small red ellipse is the combination of PVES and APV data. The solid black dot is the Standard Model prediction.

Appendix A

Compton Tables

Channel	Monitor	Channel	Monitor
0x00 (0)	BPM 3P02A Y ⁻	0x10 (16)	Laser Power M6
0x01 (1)	BPM 3P02A Y ⁺	0x11 (17)	Laser Power Attenuated
0x02 (2)	BPM 3P02A X ⁻	0x12 (18)	Laser Power Transmitted
0x03 (3)	BPM 3P02A X ⁺	0x13 (19)	Scintillator 2
0x04 (4)	BPM 3P03A Y ⁻	0x14 (20)	C13
0x05 (5)	BPM 3P03A Y ⁺	0x15 (21)	Photon Rate
0x06 (6)	BPM 3P03A X ⁻	0x16 (22)	(Not Used)
0x07 (7)	BPM 3P03A X ⁺	0x17 (23)	(Not Used)
0x08 (8)	BPM 3P02B Y ⁻	0x18 (24)	Beam Mod Ramp
0x09 (9)	BPM 3P02B Y ⁺	0x19 (25)	(Not Used)
0x0a (10)	BPM 3P02B X ⁻	0x1a (26)	Clock 1 MHz
0x0b (11)	BPM 3P02B X ⁺	0x1b (27)	BCM 1
0x0c (12)	BPM 3C20 Y ⁻	0x1c (28)	BCM 2
0x0d (13)	BPM 3C20 Y ⁺	0x1d (29)	BCM 6 (BCM 17)
0x0e (14)	BPM 3C20 X ⁻	0x1e (30)	Unser
0x0f (15)	BPM 3C20 X ⁺	0x1f (31)	Clock 4 MHz

Table A.1: Table map of the scaler channels located on ROC 31, Bank 0x1f02

Calibrations from run 22617				
Monitor	Pedestal (Hz)	Calibration ($\mu\text{A}/\text{Hz}$)	Pedestal (Hz)	Calibration ($\mu\text{A}/\text{Hz}$)
BCM 1	249 960	5.616×10^{-4}	249 960	5.616×10^{-4}
BCM 2	250 069	6.098×10^{-4}	250 069	6.098×10^{-4}
BCM 6	248 869	9.580×10^{-4}	249 541	2.088×10^{-3}
Runs	22585 \rightarrow 23594		23595 \rightarrow 23876 23885 \rightarrow 25281 25324 \rightarrow 25361	

Calibrations from Møller			Calibrations from run 25362	
Monitor	Pedestal (Hz)	Calibration ($\mu\text{A}/\text{Hz}$)	Pedestal (Hz)	Calibration ($\mu\text{A}/\text{Hz}$)
BCM 1	249 618	2.302×10^{-5}	242 174	5.43×10^{-4}
BCM 2	249 814	2.385×10^{-5}	242 889	5.89×10^{-4}
BCM 6	249 504	3.016×10^{-5}	249 741	2.030×10^{-3}
Runs	23877 \rightarrow 23885 25282 \rightarrow 25323 ($I < 5 \mu\text{A}$)		25362 \rightarrow 25548	

Table A.2: Tables of the calibration factors and pedestals for the Unser and BCMs 1, 2 and 6 for runs taken from December 2011 to May 2012.

Antenna	Pedestal (Hz)	α_i (f ⁺ /f ⁻)	Rotation Angle	Beamline Position (m)
3P02AX ⁺	1202	0.982332	0°	109.212
3P02AX ⁻	1185			
3P02AY ⁺	1198	0.981035		
3P02AY ⁻	1187			
3P02BX ⁺	1196	0.969537	29°	110.602
3P02BX ⁻	1194			
3P02BY ⁺	1196	1.033020		
3P02BY ⁻	1207			
3P03AX ⁺	1193	0.909295	45°	113.292
3P03AX ⁻	1095			
3P03AY ⁺	1184	1.006700		
3P03AY ⁻	1202			

Table A.3: Listing of each respective pedestal on each antenna. The global calibration is set to 1 and instead relies on the relative gain α between the two antennas. The angle corresponds to the rotation around the beamline. Lastly, the absolute distance from the start of the Hall C beamline is listed.

Average Run	γ -Detector Polarization	e -Detector Polarization
1 Thin Lead Configuration		
23427.2	$(91.81 \pm 1.97) \%$	$(88.97 \pm 0.09) \%$
23463.0	$(89.05 \pm 2.06) \%$	$(88.83 \pm 0.11) \%$
23507.4	$(87.59 \pm 2.26) \%$	$(89.28 \pm 0.13) \%$
23615.5	$(82.47 \pm 1.62) \%$	$(88.92 \pm 0.09) \%$
23962.2	$(91.13 \pm 1.49) \%$	$(90.45 \pm 0.12) \%$
24009.4	$(90.29 \pm 0.90) \%$	$(90.64 \pm 0.07) \%$
24051.7	$(89.05 \pm 1.00) \%$	$(89.53 \pm 0.07) \%$
24087.5	$(89.67 \pm 1.12) \%$	$(89.90 \pm 0.07) \%$
24218.3	$(88.44 \pm 1.16) \%$	$(89.72 \pm 0.06) \%$
24267.1	$(89.08 \pm 1.02) \%$	$(89.93 \pm 0.05) \%$
24316.4	$(89.16 \pm 1.46) \%$	$(89.47 \pm 0.10) \%$
24395.0	$(91.77 \pm 1.28) \%$	$(88.90 \pm 0.06) \%$
24432.7	$(89.22 \pm 1.55) \%$	$(89.70 \pm 0.08) \%$
24478.7	$(88.92 \pm 1.33) \%$	$(89.94 \pm 0.07) \%$
No Thin Lead Configuration		
24519.4	$(89.91 \pm 1.28) \%$	$(90.00 \pm 0.06) \%$

Table A.4: Table of photon detector compared to electron detector for the 1 thin lead and no thin lead configuration. Only includes the statistical errors, where the photon detector includes the statistical error of the analyzing power.

Average Run	γ -Detector Polarization	e -Detector Polarization
2 Thin Lead Configuration		
24561.8	$(92.30 \pm 1.19) \%$	$(90.19 \pm 0.07) \%$
24619.0	$(91.80 \pm 1.47) \%$	$(89.88 \pm 0.08) \%$
24661.4	$(93.49 \pm 1.29) \%$	$(89.98 \pm 0.06) \%$
24736.0	$(88.69 \pm 1.26) \%$	$(86.50 \pm 0.07) \%$
24795.9	$(89.86 \pm 1.27) \%$	$(87.17 \pm 0.08) \%$
24855.0	$(93.24 \pm 2.04) \%$	$(87.48 \pm 0.11) \%$
24899.3	$(89.30 \pm 1.68) \%$	$(87.90 \pm 0.09) \%$
24929.7	$(89.67 \pm 1.17) \%$	$(87.94 \pm 0.07) \%$
24979.7	$(89.60 \pm 1.27) \%$	$(87.88 \pm 0.07) \%$
25255.4	$(90.92 \pm 2.94) \%$	$(87.47 \pm 0.23) \%$
25352.3	$(93.16 \pm 2.11) \%$	$(87.62 \pm 0.11) \%$
25412.7	$(87.26 \pm 1.41) \%$	$(87.06 \pm 0.07) \%$
25445.2	$(90.39 \pm 1.45) \%$	$(87.45 \pm 0.07) \%$
25463.7	$(88.91 \pm 4.46) \%$	$(87.42 \pm 0.23) \%$
2 Thin Lead Configuration at $E_b = 879$ MeV		
25071.8	$(77.40 \pm 0.74) \%$	$(77.63 \pm 0.03) \%$
25136.4	$(75.57 \pm 0.79) \%$	$(77.31 \pm 0.03) \%$
25192.5	$(75.57 \pm 0.83) \%$	$(77.16 \pm 0.03) \%$

Table A.5: Table of photon detector compared to electron detector for 2 thin lead configuration at the nominal beam energy (top) of 1160 MeV and the special 879 MeV running period. Only includes the statistical errors, where the photon detector includes the statistical error of the analyzing power.

Appendix B

Compton Analysis Figures

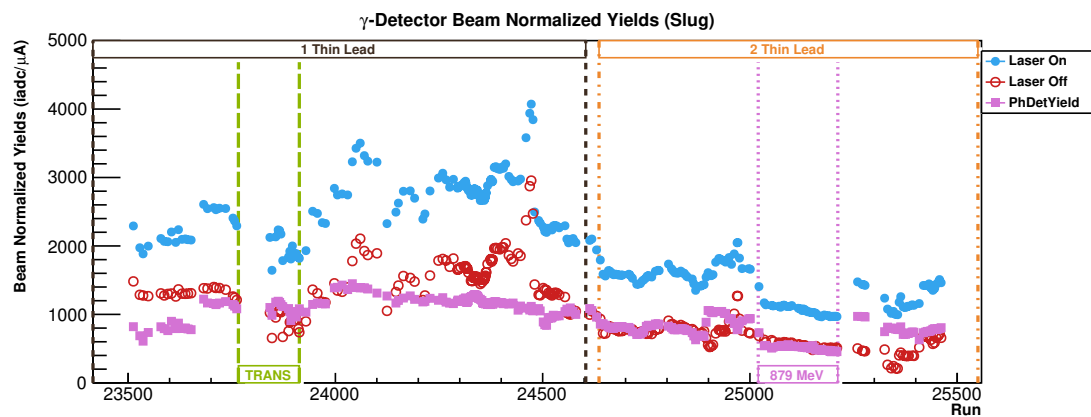


Figure B.1: The slug averaged pedestal corrected yields normalized to beam current of all the Photon Detector data from January to May 2012.

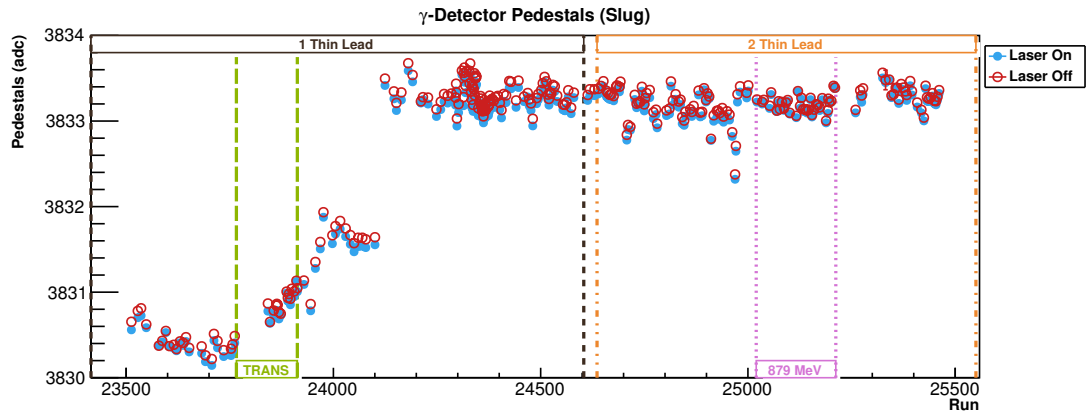
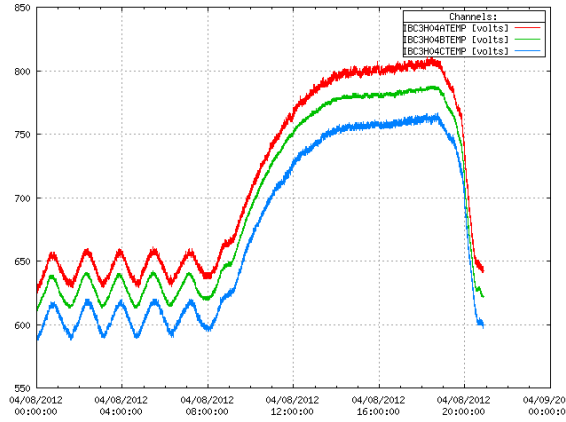
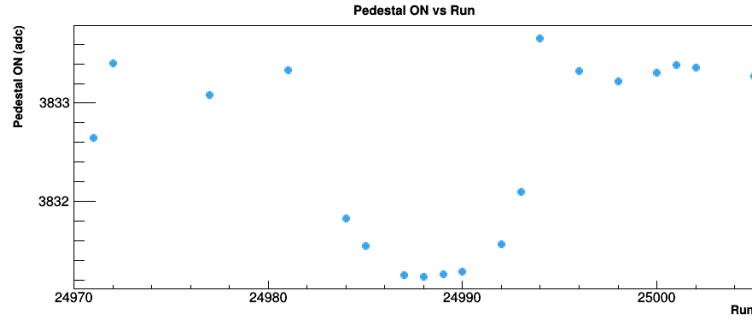


Figure B.2: The slug averaged determined pedestals for all the Photon Detector data from January to May 2012.



(a) Temperature of the BCM modules situated in the same electronics room as the Compton DAQ[120]. The temperature of the BCMs seemed to match the temperate of the room during a period when the AC failed.



(b) Pedestal ON during the temperature excursion.

Figure B.3: An illustration of the pedestal sensitivity to temperature. During a special period where the electronics's room AC malfunctioned for several hours, the pedestal slowly started to increase (pedestal is measured from the top down). The match in time with the measured room temperature (top) with the measured pedestal (bottom) track incredibly well.


 Jefferson Lab Alignment Group Data Transmittal			
TO: D. Gaskell		DATE: 08 Nov 2011	
FROM: J. Dahlberg	Checked:	# : C1416	
<u>DETAILS:</u>		Data: Step2B\BSY\QW9C\111101a, 111101b	
<p>Below are the results from the Nov 1st survey carried out on the Compton laser table and photon detector. A +X is to the beam left from ideal, a +Y is up from ideal. The Z distances (a + value being downstream), is based on the ideal table center. Values are in millimeters. Note that the ideal Y coordinate for the main beam harp listed below is 570 millimeters above the photon line of the laser table.</p>			
LASER TABLE AREA	Z	X	Y
US BPM Upstream end	-765	0.4	2.3
US BPM Downstream end	-620	0.2	2.8
US Oval pipe		0.1	
US FC	-521	-0.1	3.1
US CV mirror	-412	-0.4	3.3
Main beam harp upstream end	-84	0.3	0.7
Main beam harp downstream end	16	0.9	0.6
DS CV mirror	412	1.1	3.3
DS FC	516	0.9	3.5
DS Oval pipe		0.7	
DS BPM upstream end	613	0.5	3.0
DS BPM downstream end	746	0.2	3.2
PHOTON DETECTOR	Z	X	Y
Top of support table			-112.3
Detector average CL	3564	-1.1	4.7
Detector top left	3565	29.8	34.6
Detector top right	3564	-29.8	36.0
Detector bottom left	3563	27.7	-26.4
Detector bottom right	3563	-32.1	-25.4
<p>Front face of detector: Yaw angle is clockwise 0.309 deg. looking from above. Pitch angle is clockwise 1.116 deg. looking from the beam right. Roll angle is counter clockwise 2.096 deg. looking from upstream.</p>			

Figure B.4: Survey of Photon Detector positions as found on November 08, 2011[121].


 Jefferson Lab Alignment Group Data Transmittal			
TO: D. Gaskell		DATE: 25 May 2012	
FROM: S. Hardisty		Checked: JD	# : C1459
<u>DETAILS:</u>		Data: Step2B\BSY\QW9C\120529A	
<p>Below are the results from the May 25th survey carried out on the Compton laser table and photon detector. A +X is to the beam left from ideal, a +Y is up from ideal. The Z distances (a + value being downstream), is based on the ideal table center. Values are in millimeters.</p>			
LASER TABLE AREA	Z	X	Y
US BPM Upstream end	-777	0.4	1.9
US BPM Downstream end	-612	0.2	2.2
US FC	-511	0.4	2.3
DS FC	509	1.6	2.2
DS BPM upstream end	609	0.9	2.3
DS BPM downstream end	771	1.1	2.2
PHOTON DETECTOR	Z	X	Y
Detector average CL	3537	-5.7	4.1
Detector top left	3539	24.4	34.1
Detector top right	3537	-34.9	35.9
Detector bottom left	3537	24.7	-27.5
Detector bottom right	3535	-36.9	-26.1

Figure B.5: Survey of Photon Detector positions as found on May 25, 2012[122].

Appendix C

Qweak Tables

Scheme	Linear Fit Average (ppb)	Probability (%)	χ^2/DoF
on	-161.00 ± 7.63	3.63	212.2/177.0
5+1	-161.40 ± 7.63	3.71	212.0/177.0
Set 3	-161.40 ± 7.63	4.16	210.9/177.0
Set 4	-161.40 ± 7.63	4.93	209.2/177.0
Set 7	-161.00 ± 7.63	4.67	209.7/177.0
Set 8	-161.50 ± 7.63	4.02	211.2/177.0
Set 9	-180.80 ± 7.61	$\sim 10^{-37}$	542.5/177.0
Set 10	-161.60 ± 7.63	5.13	208.8/177.0
Set 11	-161.70 ± 7.63	4.20	210.8/177.0
Set 12	-162.10 ± 7.63	4.42	210.3/177.0

Table C.1: The results of the raw blinded asymmetry due to various regression schemes. The schemes are defined in [89]. Sets 5, 6 and 13 were excluded due to incomplete coverage of the entire asymmetry data set. Set 9 is an outlier due to the inclusion of a luminosity monitor which is highly sensitive to other background processes. The remaining schemes were all fairly consistent. “DoF” stands for Degrees of Freedom.

	Slugs	Q_{weak} Runs	Compton Runs	Dates	Wien-Flip
Wien 6	137 - 155	13843 - 14256	22616 - 22889	Nov 24, 2011 - Dec 08, 2011	Right
Wien 7	156 - 171	14260 - 14683	22893 - 23094	Dec 08, 2011 - Dec 22, 2011	Left
Wien 8	172 - 225	15163 - 15986	23151 - 23765	Jan 14, 2012 - Feb 12, 2012	Left
Wien 9	226 - 306	16172 - 17505	23933 - 25007	Feb 20, 2012 - Apr 09, 2012	Right
Wien 10	307 - 321	18415 - 18898	25250 - 25526	May 03, 2012 - May 17, 2012	Right

Table C.2: Table of Wien periods and the Q_{weak} runs. The approximate Compton polarimeter runs are also shown.

Appendix D

Miscellaneous Q_{weak} Figures

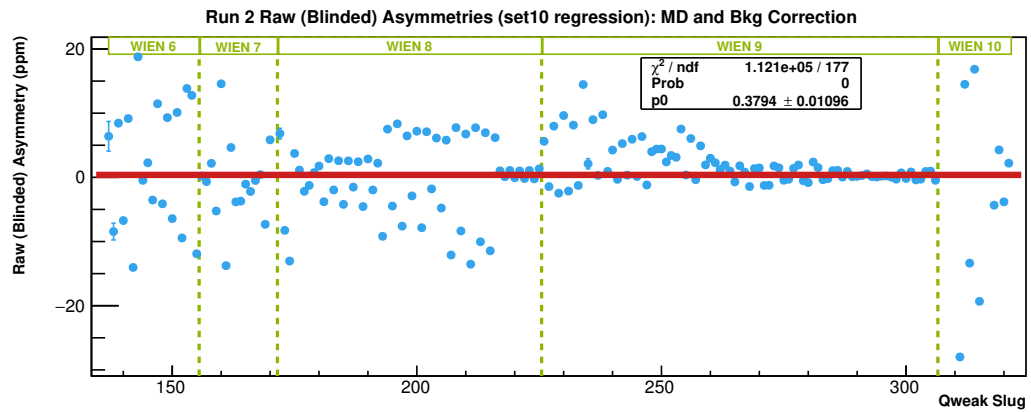


Figure D.1: The measured upstream Lumi asymmetries. Note, these are given in ppm

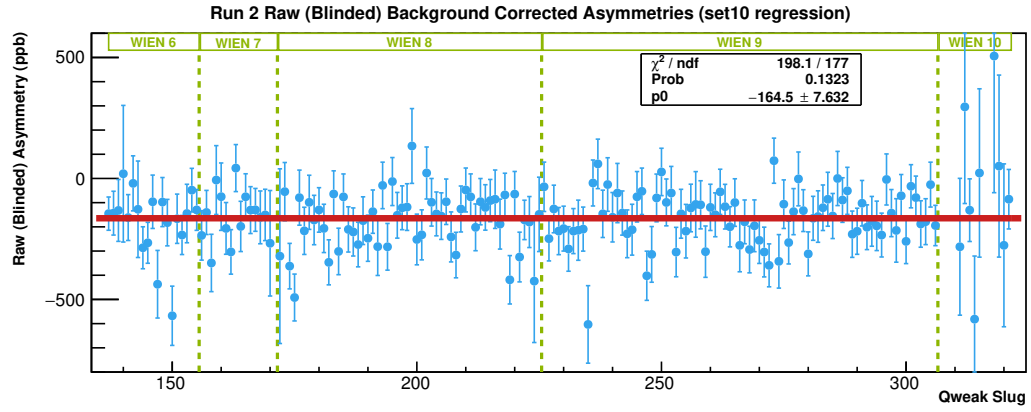


Figure D.2: Background correction due to beamline scattering applied on a slug by slug basis.

Appendix E

Derivation of Background Corrected Electron-Proton Asymmetry

We want to derive a method to subtract any background signal contributions to an asymmetry. We start with the usual definition of the asymmetry as

$$A_{\text{bkgsub}} = \frac{Y^+ - Y^-}{Y^+ + Y^-}, \text{ (E.1)}$$

where we define Y^+ and Y^- explicitly into the real electron-proton scattering asymmetry and the four known background contributions in Q_{weak}

$$A_{\text{bkgsb}} = \frac{(Y_{\text{msr}}^+ - Y_{\text{msr}}^-) - \sum_i^4 (Y_i^+ - Y_i^-)}{(Y_{\text{msr}}^+ + Y_{\text{msr}}^-) - \sum_i^4 (Y_i^+ + Y_i^-)},$$

(E.2)

$$= \frac{\Delta Y_{\text{msr}} - \sum_i^4 \Delta Y_i}{Y_{\text{msr}} - \sum_i^4 Y_i},$$

(E.3)

$$= \frac{\Delta Y_{\text{msr}} - \sum_i^4 \Delta Y_i}{Y_{\text{msr}} \left(1 - \sum_i^4 \left(\frac{Y_i}{Y_{\text{msr}}} \right) \right)},$$

(E.4)

$$= \frac{\frac{\Delta Y_{\text{msr}}}{Y_{\text{msr}}} - \sum_i^4 \Delta Y_i}{1 - \sum_i^4 \left(\frac{Y_i}{Y_{\text{msr}}} \right)},$$

(E.5)

where we brought the Y_{msr} term to the numerator and by using $A \equiv \frac{\Delta Y}{Y}$, we rewrite it as

$$A_{\text{bkgsb}} = \frac{A_{\text{msr}} - \sum_i^4 \left(\frac{\Delta Y_i}{Y_{\text{msr}}} \right)}{1 - \sum_i^4 \left(\frac{Y_i}{Y_{\text{msr}}} \right)}. \quad (\text{E.6})$$

We can use eq. (7.20) to express the above equation in terms of f_i as

$$A_{\text{bkgsb}} = \frac{A_{\text{msr}} - \sum_i^4 \left(\frac{\Delta Y_i}{Y_{\text{msr}}} \right)}{1 - \sum_i^4 f_i}. \quad (\text{E.7})$$

We substitute $\Delta Y_i = Y_i A_i$ and to express eq. (E.7) as

$$A_{\text{bkgsb}} = \frac{A_{\text{msr}} - \sum_i^4 \left(\frac{Y_i A_i}{Y_{\text{msr}}} \right)}{1 - \sum_i^4 f_i}, \quad (\text{E.8})$$

and by using eq. (7.20) once more we can write the final form as

$$A_{\text{bkgsb}} = \frac{A_{\text{msr}} - \sum_i^4 f_i A_i}{1 - \sum_i^4 f_i}.$$

(E.9)

Bibliography

- [1] https://en.wikipedia.org/?title=Standard_Model#/media/File:Standard_Model_of_Elementary_Particles.svg.
- [2] K. E. Myers, “The first determination of the proton’s weak charge through parity-violating asymmetry measurements in elastic $e + p$ and $e + Al$ scattering”, PhD thesis (The George Washington University, 2012).
- [3] A. Subedi, “Determination of the weak charge of the proton through parity violating asymmetry measurements in the elastic $e+p$ scattering”, PhD thesis (Mississippi State University, 2014).
- [4] C. Burgess, and G. Moore, *The standard model: a primer* (Cambridge, 2007).
- [5] B. C. Rislow, “Low energy tests of the standard model”, PhD thesis (The College of William and Mary, 2013).
- [6] K. Olive, et al. (Particle Data Group), “Review of particle physics”, Chinese Physics C **38**, 090001 (2014).
- [7] T. D. Lee, and C. N. Yang, “Question of parity conservation in weak interactions”, Phys. Rev. **104**, 254–258 (1956).

- [8] C. S. Wu, E. Ambler, R. W. Hayward, D. D. Hoppes, and R. P. Hudson, “Experimental test of parity conservation in beta decay”, *Phys. Rev.* **105**, 1413–1415 (1957).
- [9] F. Hasert, et al., “Search for elastic muon-neutrino electron scattering”, *Phys. Lett. B* **46**, 121–124 (1973).
- [10] F. Hasert, et al., “Observation of neutrino-like interactions without muon or electron in the gargamelle neutrino experiment”, *Phys. Lett. B* **46**, 138–140 (1973).
- [11] G. Arnison, et al., “Experimental observation of lepton pairs of invariant mass around 95 gev/c² at the CERN SPS collider”, *Phys. Lett. B* **126**, 398–410 (1983).
- [12] G. Arnison, et al., “Experimental observation of isolated large transverse energy electrons with associated missing energy at s=540 gev”, *Phys. Lett. B* **122**, 103–116 (1983).
- [13] M. Banner, et al., “Observation of single isolated electrons of high transverse momentum in events with missing transverse energy at the CERN pp collider”, *Phys. Lett. B* **122**, 476–485 (1983).
- [14] G. Arnison, et al., “Further evidence for charged intermediate vector bosons at the SPS collider”, *Phys. Lett. B* **129**, 273–282 (1983).
- [15] G. Aad, et al., “Observation of a new particle in the search for the standard model higgs boson with the ATLAS detector at the LHC”, *Phys. Lett. B* **716**, 1–29 (2012).
- [16] S. Chatrchyan, et al., “Observation of a new boson at a mass of 125 GeV with the CMS experiment at the LHC”, *Phys. Lett. B* **716**, 30–61 (2012).

- [17] R. Davis, D. S. Harmer, and K. C. Hoffman, “Search for neutrinos from the sun”, *Phys. Rev. Lett.* **20**, 1205–1209 (1968).
- [18] V. Gribov, and B. Pontecorvo, “Neutrino astronomy and lepton charge”, *Phys. Lett. B* **28**, 493–496 (1969).
- [19] M. Musolf, et al., “Intermediate-energy semileptonic probes of the hadronic neutral current”, *Physics Reports* **239**, 1–178 (1994).
- [20] A. J. R. Puckett, “Recoil polarization measurements of the proton electromagnetic form factor ratio to high momentum transfer”, PhD thesis (Massachusetts Institute of Technology, 2010).
- [21] D. H. Beck, and B. R. Holstein, “Nucleon structure and parity-violating electron scattering.”, *International Journal of Modern Physics E: Nuclear Physics* **10**, 1 (2001).
- [22] J. Erler, A. Kurylov, and M. J. Ramsey-Musolf, “Weak charge of the proton and new physics”, *Phys. Rev. D* **68**, 016006 (2003).
- [23] M. L. Friend, “A precision measurement of the proton strange-quark form factors at $Q^2 = 0.624 \text{ GeV}^2$ ”, PhD thesis (Carnegie Mellon University, 2012).
- [24] D. B. P. Waidyawansa, “A 3% measurement of the beam normal single spin asymmetry in forward angle elastic electron-proton scattering using the Qweak setup”, PhD thesis (Ohio University, 2013).
- [25] C. Reece, “Overview of CEBAF operations and SRF-related activities at Jefferson Lab”, in 9th workshop on rf superconductivity (1999).
- [26] D. Androic, et al. (Qweak Collaboration), “First determination of the weak charge of the proton”, *Phys. Rev. Lett.* **111**, 141803 (2013).

- [27] D. T. Pierce, F. Meier, and P. Zurcher, “Negative electron affinity GaAs: a new source of spin-polarized electrons”, *Appl. Phys. Lett.* **26**, 670 (1975).
- [28] R. J. Celotta, and D. Pierce, “Sources of polarized electrons”, *Advances in Atomic and Molecular Physics* **16**, 101 (1980).
- [29] T. Maruyama, et al., “Observation of strain-enhanced electron-spin polarization in photoemission from InGaAs”, *Physical Review Letters* **66**, 2376 (1991).
- [30] T. Maruyama, et al., “Systematic study of polarized electron emission from strained GaAs/GaAsP superlattice photocathodes”, *Applied Physics Letters* **85**, 2640 (2004).
- [31] F. H. Pollak, “Modulation spectroscopy under uniaxial stress”, *Surface Science* **37**, 863 (1973).
- [32] T. Allison, et al., “The Qweak experimental apparatus”, *Nuclear Instruments and Methods in Physics Research Section A: Accelerators, Spectrometers, Detectors and Associated Equipment* **781**, 105–133 (2015).
- [33] C. Sinclair, et al., “Development of a high average current polarized electron source with long cathode operational lifetime”, *Physical Review Special Topics - Accelerators and Beams* **10**, 023501 (2007).
- [34] M. Gericke, *Yes, the target is boiling ... but ... (see yield frequency spectrum)*, (Password required for access, please contact author for access.), <https://qweak.jlab.org/eelog/Analysis+Simulation/94>.
- [35] P. Wang, “A measurement of the proton’s weak charge using an integration čerenkov detector system”, PhD thesis (University of Manitoba, 2011).

- [36] J. Pan, “Towards a precision measurement of parity-violating e-p elastic scattering at low momentum transfer”, PhD thesis (University of Manitoba, 2012).
- [37] J. P. Leckey IV, “The first direct measurement of the weak charge of the proton”, PhD thesis (College of William & Mary, 2012).
- [38] F. Salio, “Principles of operation of multiwire proportional and drift chambers”, in, Academic Training Lectures, CERN (1977).
- [39] J. D. Leacock II, “Measuring the weak charge of the proton and the hadronic parity violation of the $N \rightarrow \Delta$ transition”, PhD thesis (Virginia Polytechnic Institute and State University, 2012).
- [40] D. Androic, et al. (Qweak Collaboration), “First determination of the weak charge of the proton”, Physical Review Letters **111**, 141803 (2013).
- [41] M. Loppacher, “Møller polarimetry for CEBAF Hall C”, MA thesis (University of Basel, 1996).
- [42] K. B. Unser, “Design and preliminary tests of a beam intensity monitor for LEP”, in The proceedings of IEEE 1989 particle accelerator conference (1989), p. 71.
- [43] C. S. Armstrong, “Electroproduction of the $S_{11}(1535)$ resonance at high momentum transfer”, PhD thesis (The College of William & Mary, 1998).
- [44] R. Kazimi, et al., “Precision intercomparison of beam current monitors at CEBAF”, in Proceedings of the 1995 particle accelerator conference (1995).
- [45] T. Powers, L. Doolittle, R. Ursic, and J. Wagner, “Design, commissioning and operational results of wide dynamic range BPM switched electrode electronics”, in Aip conference proceedings (1997).

- [46] J. R. Hoskins, “Determination of the proton’s weak charge via parity violating electron scattering”, PhD thesis (The College of William & Mary, 2015).
- [47] R. D. Carlini, et al., *The Qweak experiment: a search for new physics at the TeV scale via a measurement of the proton’s weak charge*, 2007.
- [48] J. J. Murray, and P. R. Klein, *A compton scattered laser beam for the 82” bubble chamber*, SLAC-TN-67-19.
- [49] C. K. Sinclair, J. J. Murray, P. R. Klein, and M. Rabin, “A polarized photon beam for the SLAC 82-inch hydrogen bubble chamber”, Nuclear Science, IEEE Transactions on **16**, 1065–1068 (1969).
- [50] C. Y. Prescott, *Spin dependent compton scattering for use in analyzing electron beam polarizations*, SLAC-TN-73-1.
- [51] M. E. Peskin, and D. V. Schroeder, *An introduction to quantum field theory* (Westview Press, 1995).
- [52] D. Jones, “Precision compton polarimetry for Hall C at Jefferson Lab”, in XVth international workshop on polarized sources, targets, and polarimetry (2013).
- [53] R. J. Loewen, “A compact light source: design and technical feasibility study of a laser-electron storage ring x-ray source”, PhD thesis (Stanford University, 2003).
- [54] M. Dalton, and D. Jones, (Password required for access, please contact author for access.), <https://qweak.jlab.org/elog/Laser/111>.
- [55] R. V. Pound, “Electronic frequency stabilization of microwave oscillators”, Review of Scientific Instruments **17**, 490–505 (1946).

- [56] R. Drever, et al., “Laser phase and frequency stabilization using an optical resonator”, English, *Applied Physics B* **31**, 97–105 (1983).
- [57] M. Dalton, *Digilock error into NIST lock*, (Password required for access, please contact author for access.), <https://qweak.jlab.org/elog/Laser/40>.
- [58] M. Dalton, *Locked laser polarization scan*, (Password required for access, please contact author for access.), <https://qweak.jlab.org/elog/Laser/147>.
- [59] M. Dalton, *Further evidence for the relationship between max DOCP and the reflected power*, (Password required for access, please contact author for access.), <https://qweak.jlab.org/elog/Laser/149>.
- [60] N. Vansteenkiste, P. Vignolo, and A. Aspect, “Optical reversibility theorems for polarization: application to remote control of polarization”, *J. Opt. Soc. Am. A* **10**, 2240–2245 (1993).
- [61] M. Dalton, *OCP RRPD correlation*, (Password required for access, please contact author for access.), <https://qweak.jlab.org/elog/Laser/202>.
- [62] D. Gaskell, *Residual background from not using flipper tiny*, (Password required for access, please contact author for access.), <https://qweak.jlab.org/elog/Laser/194>.
- [63] A. Narayan, “Determination of electron beam polarization using electron detector in compton polarimeter with less than 1% statistical and systematic uncertainty”, PhD thesis (Mississippi State University, 2015).

- [64] D. Dutta, *Final run 2 results*, (Password required for access, please contact author for access.), <https://qweak.jlab.org/elog/Electron+Detector/670>.
- [65] *Photomultiplier tubes and assemblies*, Hamamatsu (Sept. 2012).
- [66] R. Mao, L. Zhang, and R.-Y. Zhu, “Optical and scintillation properties of inorganic scintillators in high energy physics”, in Nuclear science symposium conference record, 2007. NSS ’07. IEEE, Vol. 3 (Oct. 2007), pp. 2285–2291.
- [67] A. Mkrtchyan, *Temperature comparison 24C vs 14C*, (Password required for access, please contact author for access.), <https://qweak.jlab.org/elog/Photon+Detector/145>.
- [68] W. A. W. III, J. Chen, G. Heyes, E. Jastrzembski, and D. Quarrie, “Coda: a scalable, distributed data acquisition system”, in Proceedings of the real time conference, 1993 (1993), p. 296. G. Heyes, et al., “The CEBAF on-line data acquisition system”, in Proceedings of the chep conference, 1994 (1994), p. 382. D. Abbott, et al., “Coda performance in the real world”, in Real time conference, 1999. Santa Fe 1999. 11th IEEE NPSS (1999), pp. 119–122.
- [69] R. S. Beminiwattha, “A measurement of the weak charge of the proton through parity violating electron scattering using the Qweak apparatus: a 21% result”, PhD thesis (Ohio University, 2013).
- [70] G. W. M. IV, “Parity violation in forward angle elastic electron-proton scattering”, PhD thesis (Princeton University, 2001).
- [71] *Specification of HAPPEX II ADC timing board, revision 1*, HAPPEX Collaboration (2008).

- [72] W. Deconinck, and P. King, *Set up HAPTB for similar integration window as Qweak*, (Password required for access, please contact author for access.), https://hallcweb.jlab.org/hclog/1104_archive/110428014414.html.
- [73] E. Jastrzemski, et al., “The Jefferson Lab trigger supervisor system”, in Real time conference, 1999. Santa Fe 1999. 11th IEEE NPSS (1999), pp. 538–542.
- [74] M. Friend, G. Franklin, and B. Quinn, “An LED pulser for measuring photomultiplier linearity”, *Nuclear Instrumentation and Methods in Physics Research A* **676**, 66 (2012).
- [75] R. Brun, and F. Rademakers, “ROOT — an object oriented data analysis framework”, in Aihenp’96 workshop, luusanne, sep. 1996 (1996). “ROOT — an object oriented data analysis framework”, *Nuclear Instruments and Methods in Physics Research Section A: Accelerators, Spectrometers, Detectors and Associated Equipment* **389**, 81–86 (1997). See also, <http://root.cern.ch>.
- [76] MySQL AB, *MySQL*, <http://www.mysql.com/>, 1995-2015.
- [77] G. Bardin, et al., *Conceptual design report of a compton polarimeter for CEBAF Hall A*, tech. rep. (1996).
- [78] S. Agostinelli, et al., “Geant4—a simulation toolkit”, *Nuclear Instruments and Methods in Physics Research Section A: Accelerators, Spectrometers, Detectors and Associated Equipment* **506**, 250–303 (2003).
- [79] J. Allison, et al., “Geant4 developments and applications”, *Nuclear Science, IEEE Transactions on* **53**, 270–278 (2006).
- [80] *Physics reference manual*, version geant4 10.1, Geant4 (Dec. 2014).

- [81] R. Mao, L. Zhang, and R.-Y. Zhu, “Optical and scintillation properties of inorganic scintillators in high energy physics”, Nuclear Science, IEEE Transactions on **55**, 2425–2431 (2008).
- [82] S. Baccaro, et al., “Ordinary and extraordinary complex refractive index of the lead tungstate (PbWO₄) crystal”, Nuclear Instruments and Methods in Physics Research Section A: Accelerators, Spectrometers, Detectors and Associated Equipment **385**, 209–214 (1997).
- [83] A. Rohatgi, *WebPlotDigizer*, <http://arohatgi.info/WebPlotDigitizer/app/>, 2010-2015.
- [84] B. W. Montague, “Polarized beams in high energy storage rings”, English, Physics Reports **113**, 1–96 (1984).
- [85] M. Dalton, *3rd compton dipole trim coil*, (Password required for access, please contact author for access.), <https://qweak.jlab.org/elog/Chicane/8>.
- [86] D. Dutta, *Systematic uncertainty due to spin precession*, (Password required for access, please contact author for access.), <https://qweak.jlab.org/elog/Electron+Detector/664>.
- [87] B. Waidyawansa, *Qweak transverse polarization monitor*, (Password required for access, please contact author for access.), https://hallcweb.jlab.org/qweak/transverse_monitor/.
- [88] W. Duvall, *ROOT tree of database now available*, (Password required for access, please contact author for access.), <https://qweak.jlab.org/elog/Analysis+&+Simulation/667>.

- [89] Nuruzzaman, “Beam normal single spin asymmetry in forward angle inelastic electron-proton scattering using the q-weak apparatus”, PhD thesis (Hampton University, 2014).
- [90] M. Pitt, “Comments on null asymmetry”, Qweak Physics Meeting, 2015.
- [91] M. Kargiantoulakis, *Definitions of null combinations*, (Password required for access, please contact author for access.), <https://qweak.jlab.org/elog/Management/18>.
- [92] D. Jones, *Definition of "Pitt"*, (Password required for access, please contact author for access.), <https://qweak.jlab.org/elog/Management/15>.
- [93] K. Paschke, and M. Pitt, Private Communication.
- [94] https://qweak.jlab.org/wiki/index.php/Run2_Analysis_Summary.
- [95] D. Mack, *Wien0 beamline background dilution central value and uncertainty*, (Password required for access, please contact author for access.), <https://qweak.jlab.org/elog/Analysis+&+Simulation/784>.
- [96] W. Duvall, *[W-shutter] fractional yields in blocked MD's in 'good' halo conditions*, (Password required for access, please contact author for access.), <https://qweak.jlab.org/elog/Analysis+&+Simulation/779>.
- [97] W. Duvall, “W-shutter results from pass5b”, Qweak Collaboration Meeting, Aug. 2012.
- [98] M. Kargiantoulakis, *Background correlations in run1b, test of consistency with run2 behaviour*, (Password required for access, please contact author for access.), <https://qweak.jlab.org/elog/Analysis+&+Simulation/1349>.

- [99] M. Pitt, “Beamline backgrounds summary”, Qweak Physics Meeting, May 2015.
- [100] M. Kargiantoulakis, *BB correction factors and PHYS/NULL asymmetries [run2]*, (Password required for access, please contact author for access.), <https://qweak.jlab.org/elog/Analysis+&+Simulation/1364>.
- [101] M. Kargiantoulakis, *Beamline backgrounds correction statistical uncertainty through randomization of the correction factor*, (Password required for access, please contact author for access.), <https://qweak.jlab.org/elog/Analysis+&+Simulation/1519>.
- [102] M. Kargiantoulakis, *Beamline backgrounds correction statistical uncertainty through randomization of the correction factor*, (Password required for access, please contact author for access.), <https://qweak.jlab.org/elog/Analysis+&+Simulation/1513>.
- [103] J. Magee, “Aluminum dilution status report”, Qweak Collaboration Meeting, Mar. 2015.
- [104] J. Magee, *Run 2 aluminum dilution numbers*, (Password required for access, please contact author for access.), <https://qweak.jlab.org/elog/Analysis+&+Simulation/1480>.
- [105] K. Mesick, *Asymmetry for 4% DS Aluminum*, (Password required for access, please contact author for access.), <https://qweak.jlab.org/elog/Analysis+&+Simulation/1516>.

- [106] K. Mesick, *Systematic corrections and uncertainties for 4% DS Aluminum*, (Password required for access, please contact author for access.), <https://qweak.jlab.org/elog/Analysis+&+Simulation/1518>.
- [107] K. Mesick, Private Communication.
- [108] A. Subedi, *QWGEANT 3 simulations of rates & inelastic dilution factor*, (Password required for access, please contact author for access.), <https://qweak.jlab.org/elog/Analysis+&+Simulation/451>.
- [109] R. Beminiwattha, *Main detector neutral background contribution*, (Password required for access, please contact author for access.), https://qweak.jlab.org/DocDB/0015/001549/002/qweak_soft_background.pdf.
- [110] A. Subedi, *GEANT3 based run 2 R_{RC} simulation results*, (Password required for access, please contact author for access.), <https://qweak.jlab.org/elog/Analysis+&+Simulation/1449>.
- [111] D. Armstrong, *Q^2 uncertainties - master list*, (Password required for access, please contact author for access.), <http://dilbert.physics.wm.edu/Physics/125>.
- [112] D. Armstrong, *Q^2 uncertainty and extracting Q_{weak}* , (Password required for access, please contact author for access.), <https://qweak.jlab.org/elog/Tracking/207>.
- [113] D. Gaskell, *Run 2 final polarizations - updated proposal*, (Password required for access, please contact author for access.), <https://qweak.jlab.org/elog/DAQ+&+Analysis/334>.

- [114] R. D. Young, J. Roche, R. D. Carlini, and A. W. Thomas, “Extracting nucleon strange and anapole form factors from world data”, *Phys. Rev. Lett.* **97**, 102002 (2006).
- [115] R. D. Young, R. D. Carlini, A. W. Thomas, and J. Roche, “Testing the standard model by precision measurement of the weak charges of quarks”, *Phys. Rev. Lett.* **99**, 122003 (2007).
- [116] J. J. Kelly, “Simple parametrization of nucleon form factors”, *Phys. Rev. C* **70**, 068202 (2004).
- [117] J. Arrington, and I. Sick, “Precise determination of low- q nucleon electromagnetic form factors and their impact on parity-violating e - p elastic scattering”, *Phys. Rev. C* **76**, 035201 (2007).
- [118] S. MacEwan, [Q_{weak} extraction] sensitivity to EM form factors, (Password required for access, please contact author for access.), <https://qweak.jlab.org/elog/Analysis+Simulation/1334>.
- [119] C. Perdrisat, V. Punjabi, and M. Vanderhaeghen, “Nucleon electromagnetic form factors”, *Progress in Particle and Nuclear Physics* **59**, 694–764 (2007).
- [120] P. King, *Electronics room AC is working again*, (Password required for access, please contact author for access.), https://hallcweb.jlab.org/hclog/1204_archive/120408205751.html.
- [121] D. Gaskell, *Laser table as-found*, (Password required for access, please contact author for access.), <https://qweak.jlab.org/elog/Laser/195>.

- [122] D. Gaskell, *Preliminary photon detector survey*, (Password required for access, please contact author for access.), <https://qweak.jlab.org/elog/Photon+Detector/150>.